Durham E-Theses

Time-Resolved Phase-Sensitive Second Harmonic Generation Spectroscopy of the Hydrated Electron at the Water/Air Interface

NOWAKOWSKI, PAWEL,JACEK

How to cite:

Use policy

Time-Resolved Phase-Sensitive Second Harmonic Generation Spectroscopy of the Hydrated Electron at the Water/Air Interface

Paweł Jacek Nowakowski

Submitted for the Qualification of Doctor of Philosophy

Department of Chemistry

University of Durham

2016

Abstract

Time-Resolved Phase-Sensitive Second Harmonic Generation Spectroscopy of the Hydrated Electron at the Water/Air Interface

by

Paweł Nowakowski

The hydrated electron attracts attention since its discovery over fifty years ago. Being one of the products of the ionization of water, hydrated electrons, which are free electrons in water, play significant roles in biological damage, atmospheric chemistry, nuclear chemistry, etc.. However, despite its importance and the large number of studies on the hydrated electron many aspects of it are still not resolved. One of these concern its existence and behaviour at the water surface, which is of great interest since many of the processes it is involved in take place at interfaces.

In this work, a technique is developed, that is based on the second harmonic generation (SHG) and enables the study dynamics of the hydrated electron at the water/air interface. By introducing a local oscillator, which interferes with obtained SHG from the water surface, a signal directly proportional to the sample concentration is obtained, in contrast to the quadratic dependence from conventional SHG. Moreover, the technique allows phase information to be obtained, which enables the determination of the real and imaginary parts of the 2nd order non-linear susceptibility. In addition to this, the technique uses a lock-in measurement, removing large constant offset from the interference. The technique yields high quality data on adsorbates with low surface concentration and has been extended to the time domain which provides insight into the dynamics of hydrated electrons at the water/air interface. In this experiment, the electron was generated using the charge-transfer-to-solvent transition of iodide and probed primarily over the first few picoseconds. This probes the initial solvation of the electron at the interface. Our results suggest that the dynamics are similar to the dynamics observed in the bulk, although the added phase-sensitivity provides new information about early solvation dynamics.

Acknowledgements

First of all, I would like to thank my supervisor Dr Jan R. R. Verlet. Thank you for the opportunity to work on this project, for the guidance and many fruitful discussions (and these not so much as well) during this time. Thank you for the patience with my economical with words and emotions communication and probably many language mistakes when words were finally used. Working with you was a real pleasure, I could not imagine having better supervisor. I would also like to thank my second supervisor Prof. Colin D. Bain for introducing me to this project and giving the opportunity to be a part of it.

Thanks are also due to all of the current and former members of the Verlet Group, David, Chris, Laurence, Josh, James, Catey, Alex and all the master and summer students that passed through the lab. Thank you for help in various technical and language issues I had, and off course for all the procrastination during this time. Special thanks to Dr David A. Woods, who worked with me on this project. Without your knowledge and spinning optics this project would be really hard to do (not that it was not anyway).

I would probably become crazy if I would live only with my work, that is why I have to thank all of my friends I met in various of different places. Thank you for keeping me sane by all the conversations and support. And off course by sharing trips, parties, music, art, movies, basketball and all the things we did together. For that to each of you sincere thanks.

And finally, I would like to thank my family: my parents and my sister. None of this would be possible without you. You always support me in whatever I do and push me to do even more and better. You are my best fans, my strongest critics and my best motivation. And even that mom is not able to see me becoming a doctor I know she would be as proud as you are. Kocham was.

Copyright Notice

Mojej mamie

Contents

1   Hydrated electron

At the beginning of the 20th century, Charles A. Kraus published a series of articles in which he described an investigation concerning the electrical conduction in metals. These experiments in which alkali metals where dissolved in non-metallic solvents showed that the conduction process is ionic, with the negative ion consisting of an electron surrounded by a group of solvent molecules.[1-4] With this, a new species, the solvated electron, was introduced and assigned as the source of the characteristic blue colour of these solutions.[5] In 1953, it was suggested by Platzman that the same free electron is a product of radiolysis of water.[6] However, because the lifetime of the solvated electron in water is much shorter than in the solvents used by Kraus, it was not seen experimentally for another ten years. In 1962, in a pulse radiolysis experiments, Hart *et al.* as well as Keene recorded an absorption spectrum (Figure 1.1), which could be assigned to the hydrated electron.[7-9]

Since the discovery of the hydrated electron, it has been studied extensively until this day, attracting much attention as one of the main species in radiation chemistry and the most basic radical. Produced in the radiolysis of water, hydrated electrons can have a destructive influence on biological systems, and this makes it a central entity in radiobiology and medicine.
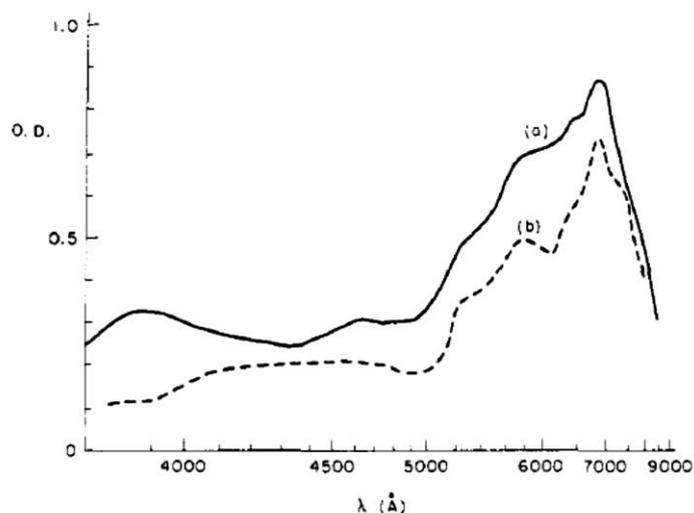
Figure 1.1. Absorption band of the hydrated electron in (a) 0.05 M solution of Na_2CO_3 and (b) pure water obtained by Hart *et al*. Reprinted with permission from ref. [7]. Copyright (2015) American Chemical Society.

Recent observations show that low energy electrons can cause single and double strand breaks in DNA.[10-12] Before becoming fully solvated, the hydrated electron can react with nucleotides dXMPs (deoxyribonucleotide where X can be T, thymine; A, adenine; C, cytosine; G, guanine) forming an excited intermediate anion state dXMP*$^-$, which can then relax to the stable anion dXMP$^-$ or dissociate. The latter can either lead to single strand breaks or modify a DNA base releasing radical fragments that can break other strands (Figure 1.2).
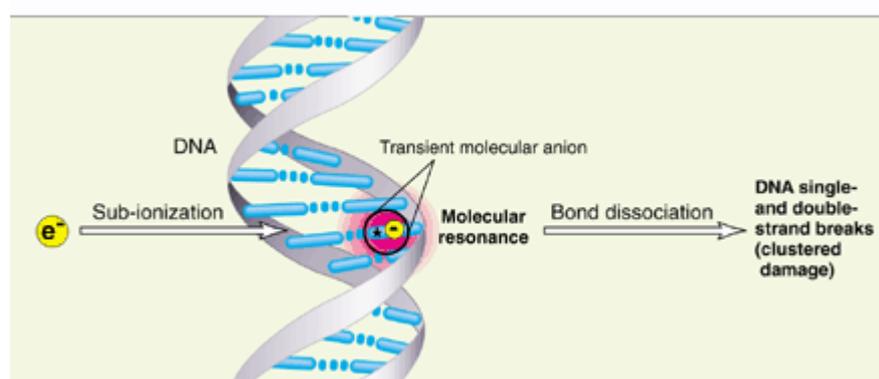

Figure 1.2. Prehydrated electron (e_{pre}^-) created in the vicinity of the DNA can lead to a dissociative electron transfer (DET) to DNA base causing a bond break, leading to DNA damage. From ref. [13]. Reprinted with permission from AAAS.

Furthermore, the precursor of the hydrated electron, so-called prehydrated electron, has been shown to be responsible for dissociative attachment to

halopyrimidines (XdUs, with X=Cl, Br and I), which are potential radiosensitizing agents.[14, 15] This reaction, leading to the formation of an anion and a highly reactive radical, is considered as a key step in the mechanism causing the replacement of thymidine in DNA by BrdU or IdU by these prodrugs in the radiotherapy of cancer.

It was also observed that the hydrated electron and its precursor takes part in the mechanism of chemotherapeutic anticancer drug cisplatin (cis-Pt(NH$_3$)$_2$Cl$_2$). [16-18] Dissociative electron transfer caused by the prehydrated electron gives rise to the cis-Pt(NH$_3$)$_2$ radical, which binds to guanine bases in DNA leading to intrastrand cross-links. Such action blocks DNA replication, which can prevent cancer growth and as a result cell death. Additionally, the hydrated electron can attach to the cisplatin radical at the binding site, causing dissociation by breaking one or two bonds with guanine bases and leading to base damage.

Apart from importance of hydrated electrons in biological systems that have been exposed to radiation, studies suggest that electrons created on the surface of ice clouds in the stratosphere take part in dissociation of chlorofluorocarbons resulting in ozone depletion (Figure 1.3).
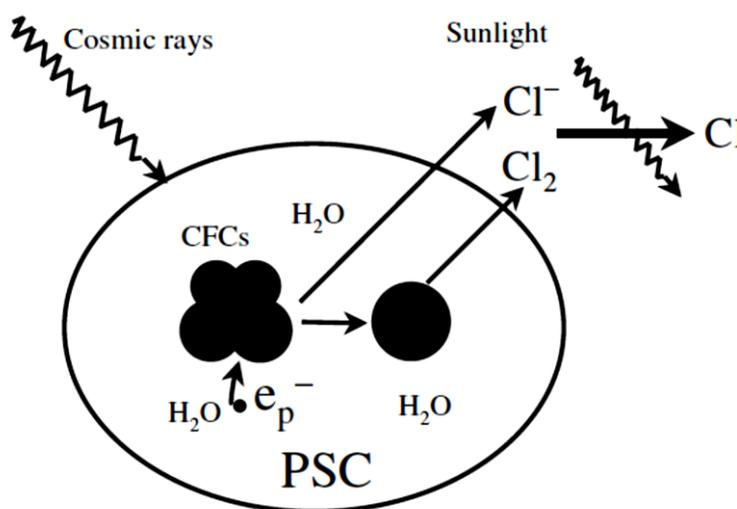
Figure 1.3. Proposed mechanism leading to depletion of ozone involving creation of hydrated electron on the surface of ice particles of polar stratospheric cloud (PSC) and its reaction with chlorofluorocarbons. Reprinted figure with permission from ref. [19] Copyright (2015) by the American Physical Society.

Hydrated electrons are produced on the surface of ice particles in polar stratospheric clouds, by high energy particles created by cosmic rays. Initially, while not fully hydrated, an electron can transfer to a chlorine containing molecule (CFCl$_3$, CF$_2$Cl$_2$ [19-

21]) adsorbed at the surface of ice, causing its dissociation. Obtained this way, Cl⁻ ions can undergo photodetachment, or produce Cl_2, which subsequently experience photodissociation. The end product are Cl atoms and these react with O_3, in part leading to the formation of the ozone hole.

As shown above, studying the hydrated electron and its precursor e_{pre}^-, which has a quantum yield much greater than the other main radicals produced in water radiolysis (OH, H) [22, 23], is important in order to understand mechanisms initiated by radiation in biology, atmospheric- and astro-chemistry, and to improve methods of radiotherapy used in cancer treatment and the protection of humans exposed to radiation.

1.1 Formation of hydrated electrons

The hydrated electron is formed when high energy radiation encounters aqueous media. The energy of the radiation is adsorbed by the solvent, leading water molecules undergoing either excitation or ionization. The latter reaction is a source of free electrons and can be represented as

$$H_2O + h\nu \rightarrow H_2O^+ + e^- \tag{1.1}$$

The ionization is immediately followed by reaction with neighbouring water molecules

$$H_2O^+ + H_2O \rightarrow H_3O^+ + OH \tag{1.2}$$

and at the same time the electron released in the ionization (eq. (1.1)) diffuses and thermalizes in the medium, forming hydrated electrons, e_{hyd}^-. As result, ionization of water leads to the formation of three primary species: e_{hyd}^-, H_3O^+ and OH.[24]

Direct ionization (eq. (1.1)) occurs for radiation of energy above the vertical ionization threshold of liquid water, which is at least 8.5 eV.[25] However, observations show that the hydrated electron can be detected also at lower energies. Both, one- and two-photon experiments indicate that hydrated electrons can be generated by exposing liquid water to energy above 6.5 eV.[26-28] This suggests that the creation of the hydrated electron at lower energies, below vertical ionization threshold, involves nuclear rearrangement or

secondary reactions. Two models for the production of excess electrons with low energy radiation in water exist: dissociation or a mechanism involving a proton transfer.[25, 29] However, since both result in the same products, they are not easily distinguishable.

The dissociation model proceeds as

$$hv + H_2O \rightarrow H_2O^* \rightarrow OH + H \tag{1.3}$$

$$H(\text{hot}) + H_2O \rightarrow H_3O^+ + e_{\text{hyd}}^- \tag{1.4}$$
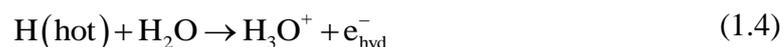
The photodissociation of water molecule leads to the generation of an OH radical and an H atom, which leaves with most of the excess energy. Immediately afterwards, the "hot" H atom reacts with a neighbouring water molecule creating H_3O^+ and the hydrated electron.

The second model explaining the production of excess electrons below the vertical ionization threshold assumes involvement of the proton transfer reaction as follows

$$hv + H_2O \rightarrow H_2O^* \tag{1.5}$$

$$H_2O^* + H_2O \rightarrow H_3O^+ + OH + e_{\text{hyd}}^- \tag{1.6}$$
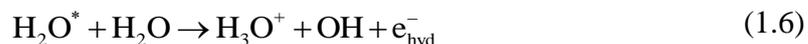
In this scheme, a water molecule gets excited and can then transfer a proton to the solvent leading to production of H_3O^+ and electronically excited OH^-, which can transfer an electron to a solvent trap giving e_{hyd}^-.

Once formed, the hydrated electron can undergo diffusional geminate recombination with other photoproducts of this reaction (H_3O^+ and OH), on a time scale of few to few hundred picoseconds. The yield of this recombination is dependent on the ejection length of the electron during its creation; because it is diffusional process, the further the electron is located from its geminate partners the smaller the probability to recombine with them. Experiments performed with different photon energies show a dependence of the excitation energy on the survival probability/ejection length of the hydrated electron (Figure 1.4).[29-35]
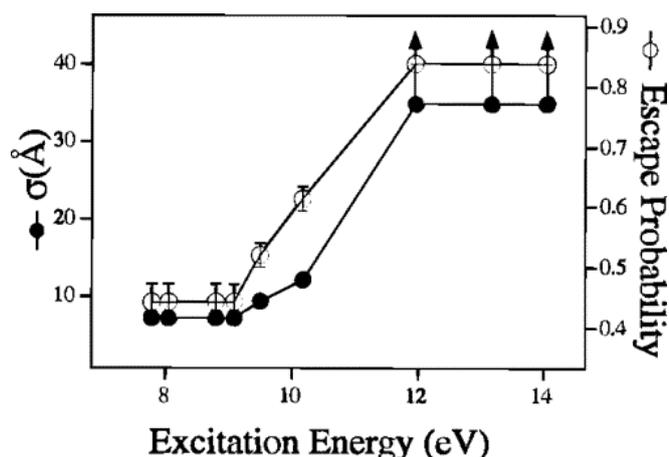
Figure 1.4. Escape probability (open circles) and the width of initial electron distribution (filled circles) due to the excitation energy. Reprinted with permission from ref. [29] Copyright (2015) American Chemical Society.

The constant and small escape probability for excitation energies below ~9 eV was ascribed as hydrated electron production in the indirect way, by dissociation or proton transfer. Beginning of the increase of the escape probability at around 9.5 eV, which is close to where the vertical ionization threshold was estimated, indicates the opening of the direct ionization channel. In the energy region, where the escape probability increases, ionization competes with the indirect ways to create the electron. While at higher energies, where escape probability is constant with increase of excitation energy, the process proceeds entirely through direct ionization.[29]

In addition to ionization of water, the hydrated electron can be produced by charge-transfer excitations of electron donors such as I^- or $Fe(CN)_6^{4-}$ in an aqueous solution. Unlike the ionization of water, generating an excess electron in this case is possible by one photon excitation using commercially available lasers (e.g. 3rd harmonic of Ti:sapphire laser) and makes this method very experimentally appealing. The absorption bands responsible for these charge-transfer processes are broad and structureless and in the ultraviolet region. However, these absorption bands lie below the detachment energy of donor in solution and are not observed in isolated ions. Moreover, they are strongly sensitive to the character of the solvent. These bands are called charge-transfer-to-solvent (CTTS). For iodide, excitation to these CTTS bands leads to the ejection of the electron from I^-, which subsequently becomes solvated, resulting in e_{hyd}^- and the neutral halogen atom.[36] For I^- in water, the lowest lying CTTS state peaks at 225 nm (5.5 eV) and can lead to ejection of the electron by excitation with photons of energy as low as ~4.9 eV (~255 nm).[37] The second CTTS

band of iodide peaks at 195 nm (6.4 eV).[38] The separation between the two lowest bands approximately matches the spin-orbit splitting of the neutral iodine atom.[39] Thus, the two lowest CTTS peaks are attributed to the ejection of the electron leaving the halogen atom in the ground state $I(^2P_{3/2})$ and the spin-orbit excited state $I(^2P_{1/2})$ of the neutral, respectively.

For excitation of an aqueous halide above its vertical ionization threshold (for iodide in water recorded as ~7.1 eV [40]) two different channels exist for the creation of hydrated electrons.[41] The minor channel corresponds to the direct detachment, where the excited ion relaxes to a well-separate solvated electron and halogen atom without passing through any intermediate state. The electron ejection in this case occurs immediately and nonadiabatically from excited ion with the electron in an the excited p-like orbital directly to the ground state hydrated electron at the long distances, exceeding 8 Å. However, the dominant channel remains through the CTTS states. In this mechanism, nonadiabatic transitions occur between the CTTS bands, which relax to the lowest CTTS state on a few 100 fs timescale. The electron is then adiabatically detached from the lowest CTTS state into the ground state of the hydrated electron. Excitation directly to the lowest CTTS state follows this route, adiabatically detaching electron with almost instantaneous effect.[42] The lowest CTTS state is predominantly of s character (30% s valence, 50% s and 17% p diffuse, 2% d), and occupies a free space mainly in the first solvation shell.[43] The first hydration shell of the iodide ion consists of around 9 water molecules, with I^-–O bonds of ~3.6 Å.[44] The wavefunction of the CTTS electron has a strongly asymmetric shape, with a radial node between diffusive outer lobe, centred at ~3 Å, and an inner lobe in a close proximity to the iodine (Figure 1.5). The most concentrated electron density region is channelled into the void created by the solvent.[43] Thus, the solvent plays a big role in the shape of the orbital and the detachment process itself, as observed by comparing the electron detachment process and relaxation from Na^- in THF and I^- in THF and water.[45] Fluctuations of the solvent molecules in the first solvation shell, which arise due to thermal disorder in liquid water, can lead to creation of a small void. Following excitation of the ion, water molecules start to reorient, directing hydrogen atoms towards the centre of the void and enlarging it at the same time. This rearrangement of the first solvent shell takes ~60 fs. This can be seen in fluorescence up-conversion experiments, that show a shift in

emission energy of >1 eV from the UV to visible region.[46] The voids can then serve as traps for the detached electrons, which attract the photodetached electrons because of their positive electrostatic potential.[47, 48] The electron is then detached from the ion and stabilized in the ground state, which takes ~200 fs. This is observable by the appearance of the absorption signal of the solvated electron.[37] However, fluorescence up-conversion measurements show that this timescale, due to the divergence in configurations of the relaxed CTTS state, can extend to ~400 fs as evidence by a decreasing emission energy.[46] The detached electron is then stabilised in such a cavity. The creation of the cavity before the detachment indicates that the fluctuations of the solvent stimulate the detachment and determine the place of the localization of the electron.[42, 43] The electron ejected from the lowest CTTS state is located in the close proximity to the iodine radical forming a solvated contact pair I^0:e^-.[42, 49]
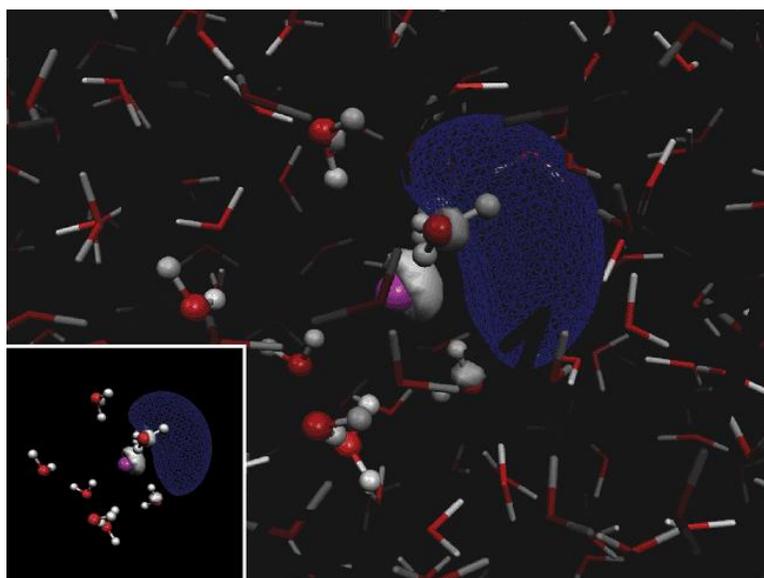
Figure 1.5. Snapshot of the molecular dynamics simulation of the iodide in a box of 864 water molecules. Water molecules of the first solvation shell, shown as ball and sticks, are included in the ab initio calculations. Rest of the water molecules represented with sticks are replaced with partial charges at the oxygen and hydrogen atoms in calculations. Picture shows the HOMO orbital of the triplet CTTS state of the iodide in water, which is argued that due to small singlet-triplet splitting is a good model for experimental CTTS state. The inset shows the picture only with the water molecules of the first solvation shell. It can be noticed that the orbital (blue mesh and white solid lobes are the opposite signs of the wave function amplitude) is directed towards the empty space in the solvation shell. Reprinted with permission from ref. [43]. Copyright (2015) American Chemical Society.

The I^0:e^- contact pair is a metastable state, with a small fraction of the electron density delocalized on the iodine atom. The lifetime of the pair is determined by the

competition between dissociation to create separate solvated species and nonadiabatic back electron transfer to the iodine. Therefore, the final yield for the separated hydrated electron created through the CTTS state depends mostly on the return electron transfer rate (which relies on the energy gap between the unoccupied ground state of the ion and the energy of the hydrated electron[42]), and the diffusion coefficients of the I^0 and e^- in the solution. The long-time survival of the solvated electron increases in the series $I^- < Br^- < Cl^-$, which may be caused by the different sizes of the anions (for iodide is harder to diffuse than for smaller chloride) and different back electron transfer rates.[36] The electron is fluctuating around ~6 Å distance from iodine atom core, being kept there by the orientational polarization of the water molecules potential well (Figure 1.6).[50, 51] In case of the CTTS detachment from chloride, the electron and resulting radical are stabilized in a contact pair separated by a layer of water molecules.[50] Because of the big size of the iodine, both components of the contact pair are located in the same cavity with no water molecules between them.
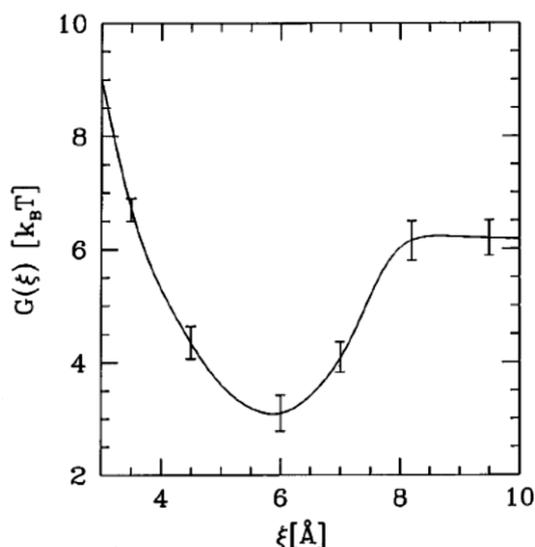
Figure 1.6. Free energy curve for the lowest CTTS state of the chloride along the separation distance between electron and chlorine atom obtained from the molecular dynamic calculations.[50] Minimum of the well corresponds to the contact pair. It can be noticed that in order to escape from the pair energy of ~3 k_BT is needed, similar energy was calculated for electron to escape pair formed with iodine.[52] Reprinted with permission from ref. [50]. Copyright (2015) AIP Publishing LLC.

Similar as in case of photodetachmet from pure water, the mechanism of detachment from I^- is associated with the survival probability and ejection length of the solvated electron.[37, 53] The survival probability as a function of excitation is presented on Figure 1.7. The ejection of the electron from iodide is preceded by

the excitation from the ground state of p character to the higher CTTS state of s character. The increase of the excitation energy across the band would be expected to increase the electron's kinetic energy, and therefore the ejection length as well. However, as can be seen in Figure 1.7, increasing of the excitation energy across the lowest CTTS band does not influence the ejection length. Due to the solvent asymmetry, the three valence p orbitals of I^- become non-degenerate.[43] The CTTS band can be partitioned into three sub-bands, corresponding to excitation from one of the valence p orbital of the ground state to the CTTS state. Thus, changing the excitation energy changes which occupied p orbital is excited, but in all cases, the electron ends up in the same s orbital of the CTTS state so that the ejection length does not change.[53, 54] Excitation to the second CTTS state is accompanied by an increase of the electron survival probability. This peak in the absorption band is attributed to the excited spin-orbit state of iodine atom. Thus the additional energy is associated with the formation of the spin-orbit excited state and no ejection length change occurs. The difference in escape yield could result from a smaller back electron transfer rate to $I(^2P_{1/2})$. However, experiments show no evidence for the formation of $I(^2P_{1/2})$ after the excitation of the second CTTS band, but indicate an appearance of the ground state $I(^2P_{3/2})$.[55] The second CTTS state of iodide lies below the adiabatic threshold to the $I(^2P_{1/2})$ continuum, however, it lies above the threshold of the $I(^2P_{3/2})$ continuum. Therefore, the proposed route is a process assigned as autodetachment, where excited $I(^2P_{1/2})$ converts into the $I(^2P_{3/2})$ and, with the proper solvent configuration, the detached electron is then able to reach the conduction band. Further increase of the excitation energy makes it easier to reach continuum, which results in an increase of the escape yield. When the energy matches the vertical detachment energy, the electrons are ejected through the conduction band. This is represented as the escape yield matching unity and an ejection length exceeding 40 Å.
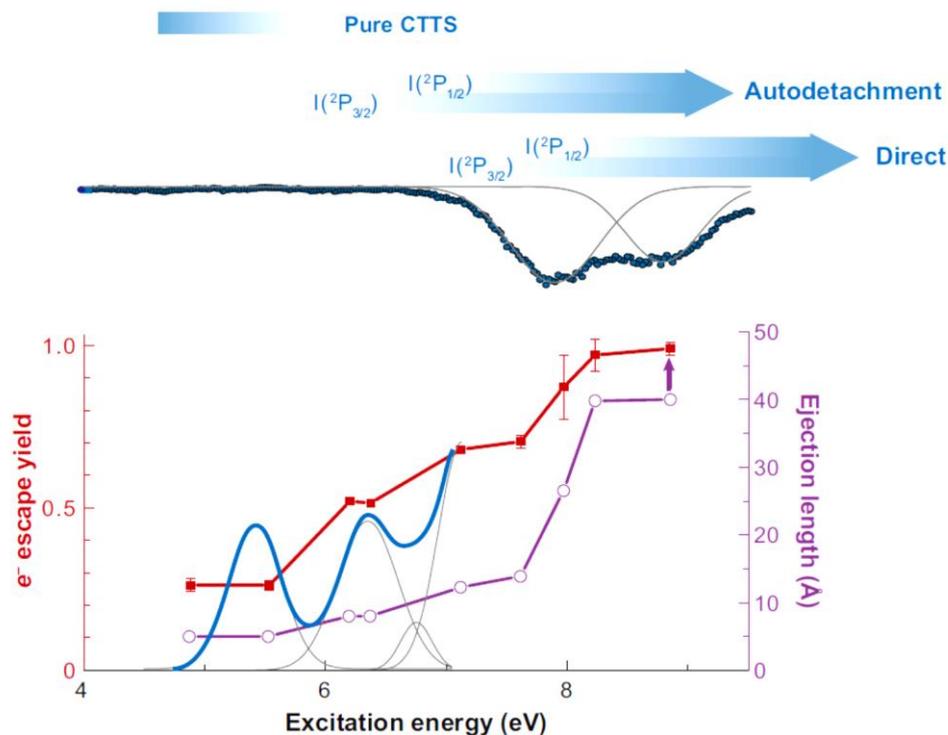
Figure 1.7. The electron escape yield and ejection length due to different excitation energy of the iodide in water solution. For comparison the absorption spectrum is showed on the graph and photoelectron spectrum above the graph. The photoelectron spectrum has two peaks, at 7.7 and 8.8 eV, which correspond to vertical detachment energy; excitation at this energies result in ejection of the electron into the vacuum and creation of the $I(^2P_{3/2})$ and $I(^2P_{1/2})$ iodine atom respectively. At the top different detachment mechanisms are indicated, over which energy range they are initiated and in which continuum they occur ($I(^2P_{3/2})$ or $I(^2P_{1/2})$).[37]

Near the water/air interface, the electron ejection dynamics may be expected to be different. Specifically, large polarizable halide anions are present at the interface and bromide and iodide may actually exhibit higher concentration at the interface than in the bulk (Figure 1.8).[56-58] When iodide, which has a strong polarizability, is near the water surface, the dipole of the iodide can increase due to the anisotropic solvation. Dipole-dipole interactions can compensate for the loss of ion-dipole interactions. Therefore, for an electron created by CTTS from iodide near the surface, there is a large likelihood that the electron is solvated at the surface or in close vicinity of it.
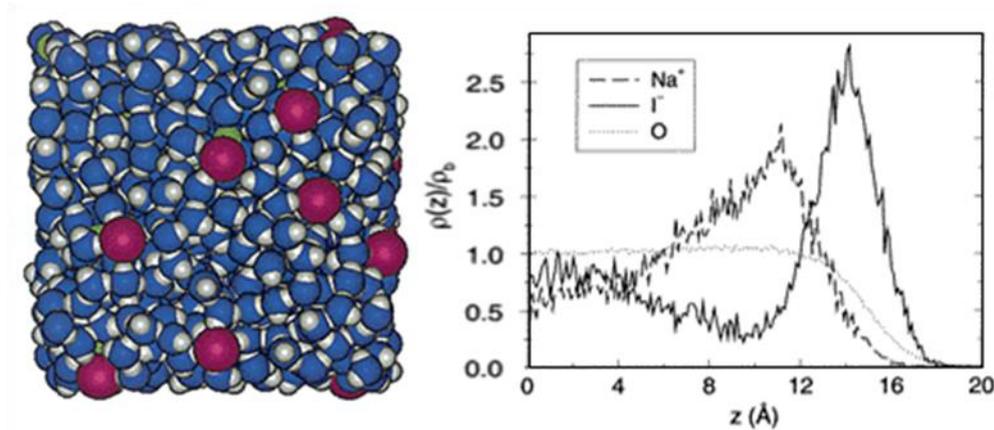
Figure 1.8. Enhanced iodide concentration on the surface of water: (left) snapshot viewed from the air side from molecular dynamics (MD) simulation of the solution/air interface of 1.2 M sodium iodide solution (iodide anion- magenta, sodium cation- green, water oxygen- blue, water hydrogen- grey); (right) number density of water oxygen atom and ions from MD simulation of 1.2 M sodium iodide solution due to the centre of the simulation slab in the direction normal to the interface, normalized by the bulk water density. Adapted with permission from ref. [57]. Copyright (2015) American Chemical Society.

Because of the disrupted solvation one might expect that the absorption spectrum of iodide at the water/air interface is redshifted. Using second harmonic generation spectroscopy, the lowest CTTS band was observed to peak around 250 nm, as shown in Figure 1.9.[59]
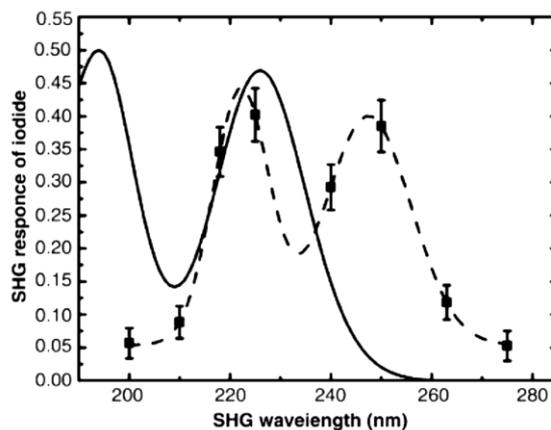
Figure 1.9. Absorption spectrum of iodide in aqueous solution (solid line), with second harmonic generation (SHG) response of iodide located on the water/air interface (squares are experimental data and dashed line is a fit to two Gaussian resonances). Reprinted from ref. [59], Copyright (2015), with permission from Elsevier.

However, mixed quantum mechanics/molecular mechanics molecular dynamics simulations show that the HOMO orbital of the CTTS state does not change significantly for iodide at the interface. It is predominantly directed towards the water phase, as shown in Figure 1.10, while the shape and character is similar as it was

described before for bulk iodide and is therefore not spectrally shifted as observed in the experiment.[43]
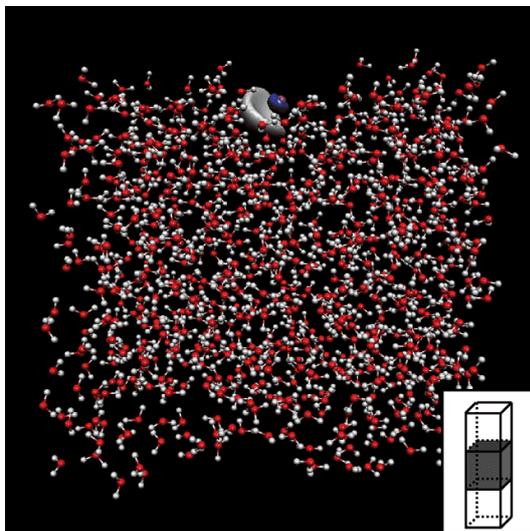
Figure 1.10. Snapshot from the molecular dynamics calculations of the iodide anion at the water/air interface. Iodide, depicted as purple, is located at the surface of the slab of water consisting of 864 water molecules, represented by ball and sticks. All water molecules were replaced in the ab initio calculations by partial charges in the place of the hydrogen and oxygen atoms. Picture shows the HOMO orbital of the triplet CTTS state of the iodide in water, which is argued that due to small singlet-triplet splitting is a good model for experimental CTTS state. It can be noticed that the orbital (white and blue lobes are the opposite signs of the wave function amplitude) is directed towards the bulk. Reprinted with permission from ref. [43]. Copyright (2015) American Chemical Society.

1.2   Properties

1.2.1   Electron structure

One of the most basic and at the same time important properties of the hydrated electron is its structure. Because there is no direct method to experimentally determine the structure of the hydrated electron on a molecular level, most of the information is based on simulations. Most of these calculations used one electron molecular dynamics simulations, where only the excess electron is treated quantum mechanically, while the surrounding water molecules are treated classically and the interaction between them is described by a pseudopotential. The results of these simulations are then evaluated by comparison with experimental observables. In recent years, debate about the electron structure concentrated on two models, the cavity and non-cavity model (Figure 1.11).
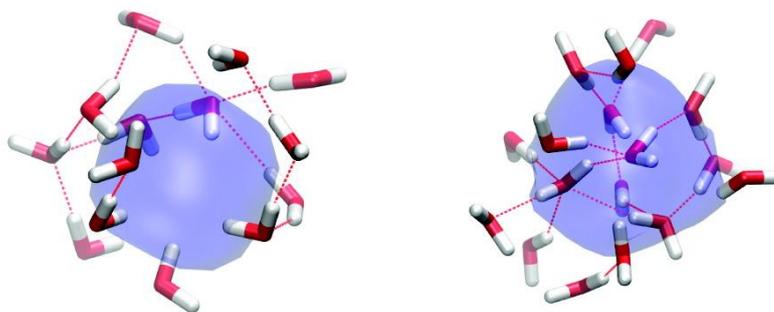
Figure 1.11. Image representation of the ground state excess electron in the cavity (left) and non-cavity (right) models. The purple sphere depicts 70% of the electrons probability distribution ($|\Psi|^2$), the sticks represent water molecules and dotted lines hydrogen bonds. It can be easily notice that in the cavity model water molecules create a structure around the electron, while in the non-cavity model water penetrates the electrons wave function. Adapted from ref. [60]. Copyright (2015) American Chemical Society.

For many years, the accepted model for the hydrated electron was the cavity model. According to this picture, a roughly spherical electron is localized in a void in the water structure, with the surrounding water molecules oriented with their hydrogen atoms pointing towards the electron density. Such a cavity consists of 4 to 6 water molecules in the first shell, depending on the used theoretical model. The electron radius of gyration varies between 2.1 and 2.4 Å, and distance between the centre of mass of the electron and the nearest hydrogen of the water molecules is ~ 2 Å. The vertical detachment energy, which is the energy needed in order to remove the excess electron without changing the nuclear configuration of the solvent, according to simulations with electron localized in the cavity is 3.2 or 3.7 eV.[61] Overall, calculated values based on this picture match fairly well with the experimental observables. The radius of gyration, taken from an electron spin resonance (ESR) echo experiment on an aqueous glass at 77 K, as well as extracted from the line shape of the experimental absorption spectrum of the hydrated electron in ambient temperature, suggest a value of 2.45 Å.[62, 63] The vertical detachment energy observed directly in the liquid jet photoelectron spectroscopy experiments varies from 3.3 to 3.6 eV.[64-66]

Despite the good correlation of the cavity model with experiment, this picture has been recently questioned, and a new so called non-cavity model was proposed.[67] It was suggested that the pseudopotentials used in previous calculations ignored some of the important details of the molecular core region. Using a new pseudopotential, the non-cavity model was suggested, in which the hydrated electron is not localized in the

void but is rather delocalized over many water molecules. Although water molecules do not form the cavity, there still exists a specific orientation where the electron is located with hydrogen atoms pointing towards the electron's centre of mass. Moreover, the water molecules are dragged together, resulting in the electron occupying a region of enhanced water density. In this model, the excess electron has a bigger size reaching a radius of gyration of ~2.69 Å.[60] The estimated vertical detachment energy is ~5 - 6 eV and is significantly larger then experimental value.[61] The non-cavity model remains controversial and was almost immediately criticized. It was shown that the applied pseudopotential was not appropriate and can result in a false picture of the electrons structure.[60, 68, 69]

Nevertheless, the non-cavity model cannot be completely ruled out. At present, it seems that both of the cavity and non-cavity models may be partly correct. Uhlig *et al.* performed an ab initio molecular dynamics calculations, where not only the excess electron is treated quantum mechanically, but also the valence electrons of the surrounding water.[70] The simulations indicate water molecules forming a structure around the electron containing on average 4 water molecules with hydrogen atoms pointing towards the centre. However, only 41% of the electrons spin density resides in the cavity. It turns out that the structure of the electron is more complex with a significant part of the electron extending beyond the cavity. It was shown that there are two more contributions to the electrons spin density besides the cavity part. 24% of the electron is directly overlapping with water molecules of both first and second solvation shell, while the remaining 35%, similar as in the non-cavity model, contribute to the diffused electron beyond the first solvation shell not overlapping with water molecules (Figure 1.12). The estimated radius of gyration from this simulation is 2.6 Å and the vertical detachment energy has a mean value of 3 eV. The model is supported by the ab initio calculations performed by Kumar *et al.* on the hydrated electron in water cluster anions, where values close to experimental are obtained when some diffuse character is included.[71]
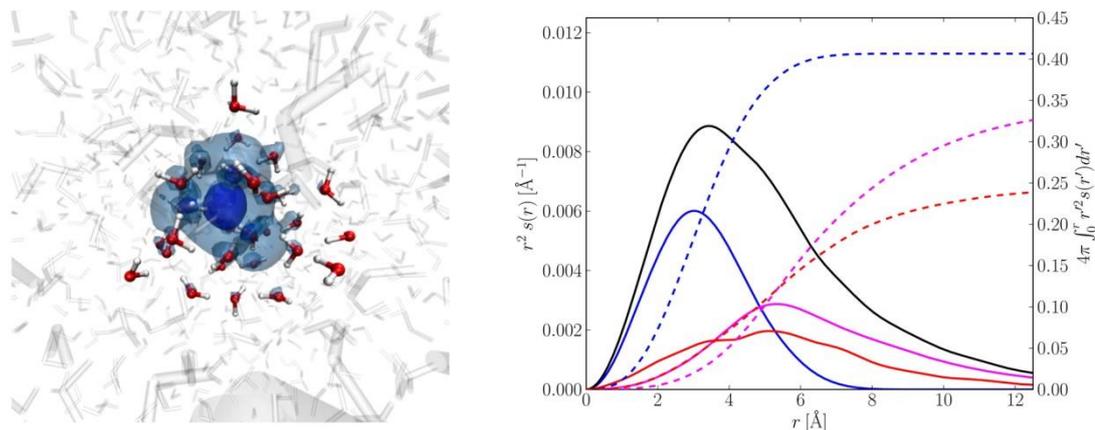
Figure 1.12. Left: snapshot from the performed simulation. The blue sphere represents the electron spin density distribution, the colour and transparent ball and stick models represents water molecules treated quantum mechanically and molecular mechanically, respectively. Right: The excess electron spin density distribution (black) with indicated contributing parts from inner cavity (blue), overlapping with water molecules (red) and diffuse part (magenta). Full lines correspond to spin density and dashed lines to integrals. Adapted with permission from ref. [70]. Copyright (2015) American Chemical Society.

1.2.2   Absorption Spectrum
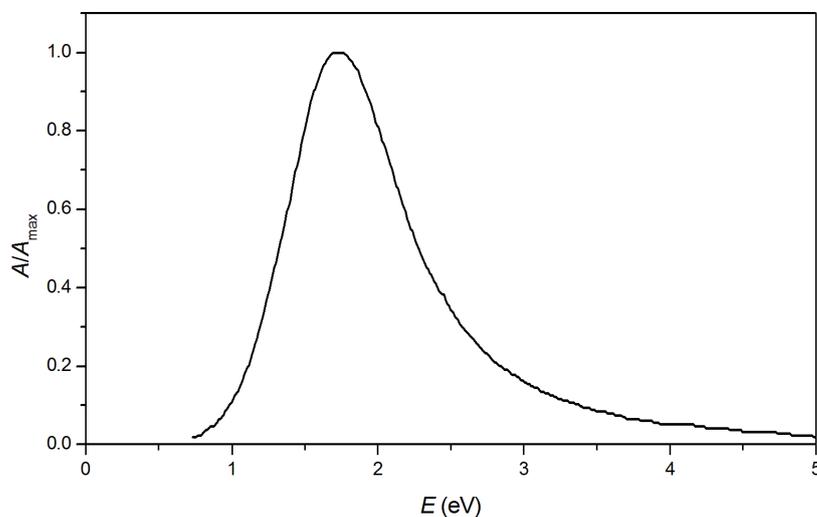
Figure 1.13. Optical absorption spectra of solvated electron in H_2O at 298 K. Adapted with permission from ref. [72]. Copyright (2015) American Chemical Society.

The hydrated electron, as mentioned before, was first observed by Hart *et al.* in a pulse radiolysis experiment.[7] The absorption spectrum they recorded was assigned to hydrated electron due to similarity with the spectra of solvated electron in ammonia and methylamine. Additionally, the microsecond lifetime and the fact that the signal is

reduced by introducing electron scavengers to the solution, all suggested that the observed absorption spectrum was that for the hydrated electron. This absorption spectrum has become its most characteristic feature (Figure 1.13). It has an asymmetric shape, which extends through the entire visible spectrum to the near IR and peaks at 720 nm (1.7 eV). The band can be fitted with a Gaussian shape function on the lower energy side of the band and with a Lorentzian shape function on the higher energy extending into a long tail to the high energies.[73] This optical spectrum corresponds to the electronic transitions of the hydrated electron. The spectrum is dominated by the transitions from the *s*-like ground state to three excited *p*-like states, which provides a Gaussian shape of the spectrum. The three *p*-like orbitals are approximately perpendicular to each other in orientation and are localized. They are nondegenerate, with energy splitting between the excited states being influenced by the fluctuations of the symmetry, while the energy gap between ground and excited states depends on the radius of the cavity.[74] The Gaussian part of the optical spectrum (both red side of the spectrum, its width and the position of the maximum) can be fairly well reproduced by simulations, but there is still no model that accurately predicts the Lorentzian tail on the blue side. It has been suggested that the high energy tail obtained in the experiments comes from the excitation of the bound state to the continuum.[74] However, recent time dependent density functional theory (TD-DFT) calculations, based on the snapshots from the one electron molecular dynamics simulation, suggest that higher-lying bound states lie between the three *p* states and continuum and that these can be excited leading to the Lorentzian tail (Figure 1.14).[75] These higher bound states are diffuse, extending over several water molecules and are bound only by the net polarization of these molecules. This model combined with the mixed quantum/classical calculations results in the complex model of the electron structure described before (having a cavity and diffuse contribution).[76] Although the calculated spectrum does not match the experimental data perfectly, it provides a good physical picture of where its shape comes from.
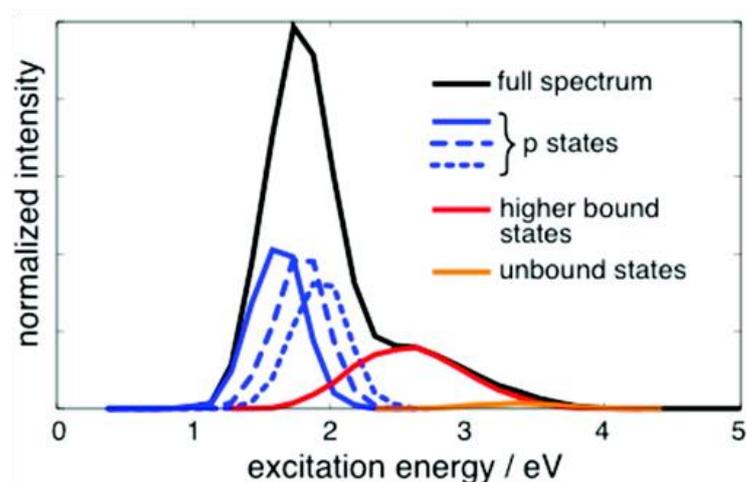
Figure 1.14. Obtained in the TD-DFT simulation absorption spectrum of the hydrated electron in liquid water and its decomposition to different types of excited states. Adapted with permission from ref. [75]. Copyright (2015) American Chemical Society.

1.2.3 Vertical detachment energy

Another characteristic feature of the hydrated electron, besides absorption spectrum, that can be measured experimentally is its vertical detachment energy (VDE). Values of the VDE of the solvated electron can be obtained from the photoelectron spectroscopy measurements on water cluster anions as a function of cluster size extrapolation to infinite size. It was observed that the VDE varies linearly with $n^{-1/3}$, where n indicates number of water molecules in a cluster, and an extrapolation yielded a value of VDE = 3.3 eV.[77] However, it was also observed that, depending on the temperatures of the clusters, different isomers of the hydrated electron could be formed.[78] The new isomers gave smaller values of VDE and, although these still depend linearly on $n^{-1/3}$, extrapolation yielded smaller values. The lower VDE isomer was assigned to a different localization of the excess electron in the cluster, as predicted by molecular dynamics simulations.[79] Isomers resulting in lower VDE were attributed to containing a surface electron and an internal electron for those with higher VDE. However, different theoretical and experimental investigations suggest different assignment of electron position to the specific cluster isomers, suggesting that it may additionally depend on the cluster size.[79-81] The bulk VDE have been recently measured directly, using liquid microjets coupled to photoelectron spectroscopy, and has yielded values for the VDE ranging between 3.3 and 3.6 eV.[64-66]

1.3   Surface hydrated electron measurements

One of the most important "things" about the hydrated electron that is still unclear concerns its solvation at interfaces. For example, does it solvate at the surface of liquid water and how is the solvation different from the bulk; how are its properties or reactivity affected; and what is the role of surface electrons in chemistry? There is a great interest about these questions because, when considering the role of the hydrated electron in biological or atmospheric events, most of its reactivity occurs at aqueous interfaces.

Gas phase experiments have played a significant role in the understanding of excess electrons in water. Water cluster anions were first observed in the 80s.[82] The advantage of exploring a system with smaller number of degrees of freedom is that it provides a higher level of detail that can be attained from experiment and theory, thus leading to a better understanding of the system. Even if the behaviour of clusters differs from that in bulk, it can provide an idea of what can be expected. As mentioned before, the surface localization of the electron was predicted by molecular dynamics simulations.[79] These early studies concluded that small water clusters $n < 32$ have a surface localized excess electron with a VDE smaller than that for an interior located electron. For larger cluster sizes, the interior position was shown to become the dominant isomer due to role of long range interactions playing a significant role in the electron localization. In accordance with that, Verlet *et al.* assigned their observed classes of isomers with different VDE values as originating from different localization of the hydrated electron.[78] The isomer with higher VDE (isomer I) was assigned to the interior solvated electron, while isomer with smaller VDE (isomer II) to the surface located one. Isomer II formed preferentially in cold clusters. Further investigation by Verlet *et al*. on water clusters containing an iodide showed that CTTS excitation led to the initial formation of isomer II then converts into isomer I on a 1 ps timescale.[83] This is in accord with the established view that iodide sits on the water surface of the cluster. These dynamics matched with the simulations predicting a similar sequence of events.[84, 85] Surface location of the excess electron in water cluster anions also supports later simulations by Turi *et al.*.[80] However they stated that the isomer previously assigned as containing internally solvated electron (isomer I) in fact has the

electron at the surface as well and the internally solvated one should appear for much larger clusters in range of 100 to 200 molecules.

Vibrational spectroscopy experiments showed a binding motif involving a double acceptor water molecule suggesting surface location in small clusters ($n = 4 - 6$).[86] On the other hand, mixed quantum/classical molecular dynamics by Madarasz *et al.* on large water cluster anions (n = 200, 500, 1000 and 8000) indicate that the surface electron is more evident in smaller clusters, while in bigger clusters it solvates to interior localization in a short time.[87] Ab initio molecular dynamics calculations on medium sized water clusters (n = 32) at varying temperatures concluded that the cold isomers (isomer II) are metastable structures trapped in glassy clusters.[88] Under ambient conditions, however, such structures should not exist and the electron relaxes to an internally located structure on a picosecond time scale.

Overall, determining the location of the hydrated electron in the water cluster anion has been challenging and is still not entirely resolved. It seems that the excess electron located on the surface can be found in the water clusters, although it may require specific conditions. Smaller clusters prefer surface localization of the electron as well as cold clusters, which can be related rather to ice than liquid water. Moreover, a surface electron seems to exhibit a lower vertical detachment energy than if located internally.

More clearly than in water cluster anions, the surface localisation of the excess electron can be observed in ice. As briefly discussed at the very start, such electrons may have a great importance in atmospheric chemistry. A number of experimental and theoretical studies have been carried out in recent years in order to investigate this case.

To experimentally probe such solvation sites, ice deposited on the metal surface provides an ideal system. By selecting appropriate conditions, amorphous or crystalline ice can be obtained. The prepared sample can then be investigated by time and angle resolved two photon photoelectron spectroscopy (2PPE). The overall picture of the experiment is presented in Figure 1.15. Excited by a pump photon, an electron from the metal is excited to image-charge states that overlap with its conduction band of the adsorbed ice. The electron then localizes and solvates and can be probed by a second pulse that removes electron, and its kinetic energy analysed by a time of flight spectrometer.[89]
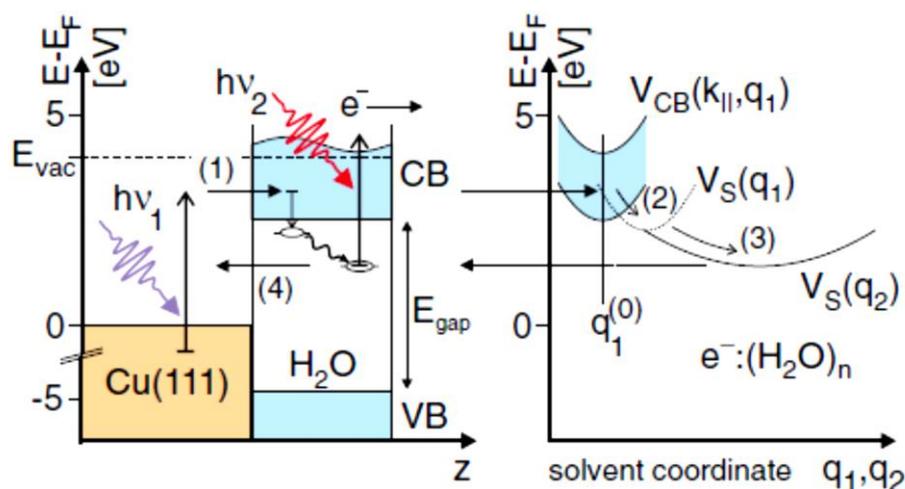
Figure 1.15. Scheme explaining events occurring during the 2PPE experiment on the ice doped on Cu. Delocalized electrons photoexcited by the pump pulse $h\nu_1$ from the metal transfer to the ice conduction band CB(1). Delocalized electrons in the ice CB can then localize in the specific sites in ice (2) and subsequently stabilize/solvate (3). At the same time during steps 1-3 electron can be transferred back to the metal (4). Initiated events are monitored with a probe pulse $h\nu_2$, which photoionizes the sample, and the kinetic energy of the electron is then detected by a time of flight spectrometer at various delay times. Reprinted with permission from ref. [90]. Copyright (2015) by the American Physical Society.

The results of these experiments show that for the amorphous ice the measured solvation dynamics do not change as more ice layers are added, or with the co-adsorption of Xe. In such cases, no influence on the binding energy of the solvated electron was observed.[90, 91] This points to bulk localization of the excess electron in amorphous ice. However, adsorption of Xe on crystalline ice was observed to quench the electron signal. Furthermore, the dynamics observed in an experiment with crystalline ice indicate much longer lifetime of the excess electron than in case of the amorphous ice.[92, 93] These results suggest a surface localization of the excess electron on crystalline ice.

The 2PPE results are supported by recent density functional theory and mixed quantum/classical molecular dynamics studies on crystalline and amorphous ice, that show an affinity of the location of the excess electron to the surface and the bulk, respectively.[94-96] In the case of amorphous ice, electron locates itself in the position of low density of solvent molecules that arise from defects in the hydrogen bonding structure. Agreeably with this, when introduced in the crystalline ice, the electron locates on the surface due to lack of such pre-existing pockets. The different lifetimes for an electron in amorphous and crystalline ice can also be explained. An electron localized on the surface has a bigger dielectric barrier to overcome in order to decay

back to the metal, while bulk electron is located closer to the metal and can thus decay faster.

However, much like the water cluster anion experiments, deposited ice experiments conducted at ~40 K do not represent ambient water. With the liquid microjet technique, photoelectron spectroscopy measurement on the liquid water can be performed and has been used to explore the solvation of electrons at the surface of water. The basic picture of experiment is presented on Figure 1.16. A beam of water of a micrometre diameter is generated by pressing through a nozzle using high pressure pump. The hydrated electron is produced by a pump pulse a few millimetres from the nozzle tip, where the water jet exhibits laminar flow. Subsequently the electron is probed by photoemission induced by ultraviolet pulse.
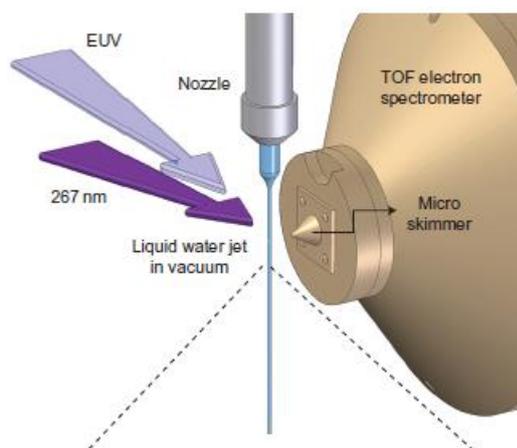
Figure 1.16. Graphic representation of the liquid microjet experiment. A beam of water is generated by pressing a liquid solution through a micrometre diameter nozzle using a high pressure pump. The hydrated electron is produced by a pump light beam in distance around 1-2 mm from the nozzle. Subsequently, electron is probed by its photoemission induced by an ultraviolet beam. Kinetic energy as a function of time can be then detected through the time of flight spectrometer, into which emitted photoelectrons access through the skimmer. Reprinted by permission from Macmillan Publishers Ltd: Nature Chemistry ref. [66], copyright (2015).

Siefermann *et al.* recorded the photoelectron spectra of electrons generated in water and observed two distinct peaks pointing to different VDE values. One agreed with that for a bulk electron, but they also observed a lower VDE value of 1.6 eV.[66] This value matches the value obtained by extrapolation of the VDE from large water clusters with the isomer II (surface bound) conformation. Because of the use of an EUV probe pulse, for which the inelastic mean free path is small, the experiment is expected to be sensitive only to few molecular layers from the surface. These arguments made

them suggest that the observed species are surface localized hydrated electrons. Additionally, it was found that the observed species has a long lifetime exceeding 100 ps.

However, the low value of the VDE was questioned by several groups, since no other liquid jet experiment was able to observe this feature. Buchner *et al.* used the CTTS transition from iodide to create excess electrons.[97] In order to distinguish the surface contribution, they used tetrabutyl ammonium iodide (TBAI), for which I^- has a strong affinity to the surface. To probe the bulk, they used NaI solution. Thus, changes observed in the experiment due to addition of the NaI to the TBAI solution should be much more pronounced if the signal comes from a bulk electron. Results obtained by them show no evidence of the 1.6 eV VDE and the signal assigned by their experiment to the surface species decays rapidly (sub picosecond time scale). Similarly, experiments by Yamamoto *et al.* using TBAI, NaI and DABCO, all having enhanced concentration at the surface, show no long lived surface excess electron.[98] What they found was that the hydrated electron created near the surface resides in the bulk and exhibit a similar VDE of that measured before for the bulk hydrated electron. These experiments different to those from Siefermann *et al.* in that they use a probe of much lower energy, which penetrates the sample much deeper. Overall, liquid jet experiments do not conclusively answer the question of hydrated electrons surface localization. However, the experiments that did not find a long-lived surface electron show that, if not at the surface itself, the solvated electron might be found in the proximity of it.

Clusters and liquid microjets experiments suggest that the VDE can be correlated with the location of the excess electron. However, mixed quantum/molecular mechanics molecular dynamics calculations of the water clusters show that VDE depend instead on the size of the electron rather than its location (Figure 1.17).[99, 100] Although a small relationship of the VDE and location can be observed, a much stronger relationship is observed between VDE and the electrons radius of gyration. The smaller the electron is, the more strongly bound it is in the cluster. Therefore, the photoelectron spectroscopy measurements can be used to evaluate the size of the electron rather than its localization.
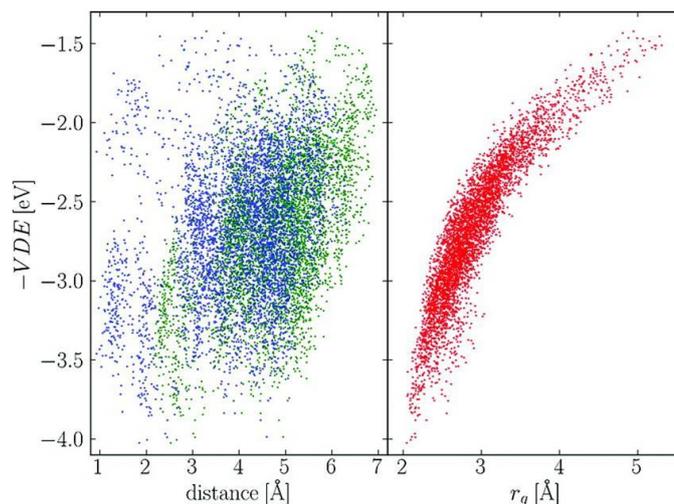
Figure 1.17. Dependence of the VDE on the distance of the excess electron from the centre of the water cluster (green- data using the average distance of the electron from the cluster centre of mass; blue- using the distance between the centre of the electron and the cluster centre of mass) and its radius of gyration. Reprinted with permission from ref. [99]. Copyright (2015) American Chemical Society.

Uhlig *et al*. recently performed mixed quantum mechanics/molecular mechanics molecular dynamics simulations of the excess electron at the liquid water surface and showed that, although the hydrated electron is embedded in the simulated water layer, a part of electrons charge density spreads into the vapour phase (Figure 1.18).[101] The surface hydrated electron can be distinguished from the bulk by the additional part extending into the vapour phase. The study shows that the structure of the electron at the surface is very similar to its bulk equivalent. The biggest part of the electrons spin density is contained in a cavity, while the overlapped with water and diffused parts takes around half of the density. Only around 10% of the spin density extends into the vapour phase. The centre of the electron is between 1 and 2.5 Å from the surface and it has a full first solvation shell composed of ~4 water molecules similarly to bulk. The deficiency in solvation appears in the second solvation shell and beyond. Additionally, in accordance to previous simulations, no correlation between distance from the surface and VDE was observed for VDE was determined to be 3.3 eV and the radius of gyration of the electron 2.7 Å. Thus similar to those of the bulk hydrated electron.
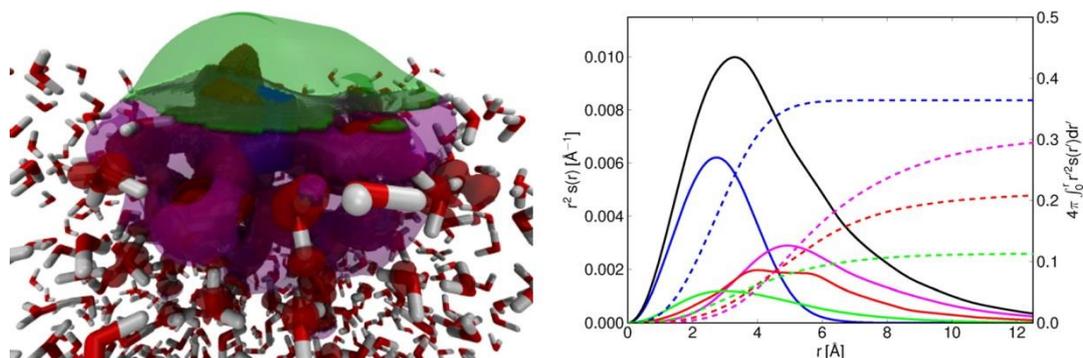
Figure 1.18. Left: Snapshot from the performed QM/MM MD simulations. Green sphere represents electrons spin density sticking out to the vapour phase. Right: The excess electrons spin density distribution (black), with indicated contributing parts from inner cavity 37% (blue), overlapping with water molecules 21% (red), diffuse part 31% (magenta) and part in the vapour phase 11% (green). Reprinted with permission from ref. [101]. Copyright (2015) American Chemical Society.

An important issue in studying surface hydrated electron seems to be what it is meant by it. In the water cluster anions and crystalline ice, the surface is well-defined and a surface electron is an excess electron which sits on top of the system bound only by one or two water molecules. However, as shown in the liquid microjet experiments and the simulations on liquid water system, this probably does not occur in the ambient water. Instead, Uhlig *et al*. calls surface hydrated electron an excess electron which is essentially a bulk solvated electron, with a full first solvation shell and a small part of the density protruding beyond the water phase.[101] Therefore, for ambient water a more appropriate nomenclature is interfacial rather than surface hydrated electrons.

Although there have been several studies probing electrons at aqueous interfaces, none have been on ambient water interfaces. Although liquid microjets experiments provide a good way of studying electron in liquid water, it is questionable for its surface. The experiment is performed in the vacuum, where liquid matter will rapidly evaporate creating a dense cover of vapour. Even when this effect is minimized by use of the micro-sized liquid jet, such a system might not be the best representation of ambient water. Furthermore, as described before, obtained VDE values from the photoelectron spectroscopy measurements do not indicate the position of the hydrated electron in the system but its size.

The study under ambient conditions is possible using a second harmonic generation (SHG) technique, which is specifically surface sensitive. SHG was used before by our group in order to study interfacial hydrated electron.[102] The experiment showed that the signal obtained for the excess electrons generated by CTTS from iodide

near surface is not altered by deposition of the decanol on the sample, which forms a layer on the water surface not penetrating into it. Deposition of the Hexaethylene glycol monododecyl ether ($C_{12}E_6$) on the other hand, which extends into the water, shows the reduction of the signal. Such an influence on the signal coming from the absorption by the hydrated electron is in agreement with picture of the solvated electron presented by Uhlig *et al.*, where it does not resides at the water surface but it is located just underneath it, mostly buried in the water phase. Despite the advantages of this technique, it is not perfect in order to study the hydrated electron in more detail in a form as used before by our group. The main issue arising here is that, because of the nature of the SHG measurement, the detected signal is quadratic with concentration of the species being probed and cannot be directly compared with other measurements performed on the hydrated electron. The aim of this thesis is to overcome this problem, introducing at the same time a few advantageous features.

2   Second harmonic generation

The first chapter explained the importance of the studies concentrated on the hydrated electron and how challenging they can be. Particular emphasis was placed on the interfacial location of the electron, which is the subject of the investigation described in this work. It was also mentioned that the hydrated electron at the surface of ambient water can be studied by second harmonic generation (SHG). This chapter explains how SHG can provide surface information.

Second harmonic generation is a nonlinear optical effect, in which photons of the same frequency are combined through the interaction with a nonlinear medium, resulting in photons of double the initial frequency. This process was first discovered in 1961 by Franken *et al.* shortly after the development of the first ruby laser.[103] In their experiment, a 694 nm laser beam was focused inside a crystalline quartz sample resulting in an output containing, besides the fundamental beam, a small signal at half the wavelength of the initial beam (Figure 2.1). This discovery is considered the beginning of the new field called nonlinear optics.
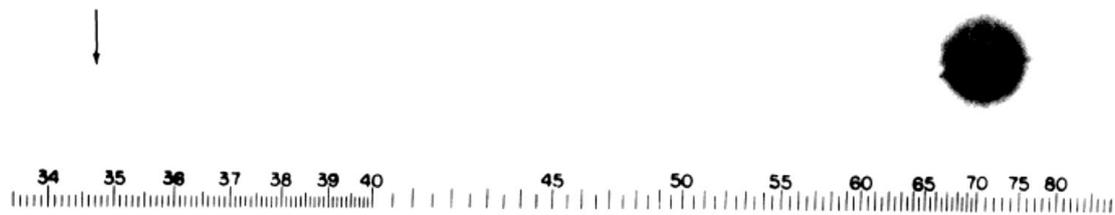
Figure 2.1. Reproduction of the spectrographic plate from the experiment by Franken *et al.* with an arrow indicating the appearance place of the produced second harmonic at 347 nm (the image of the SHG was erased from the published picture as a result of mistaken for a speck of dust [104]). Visible on picture is also image of the fundamental beam. The wavelength scale is in units of 100 Å. Reprinted with permission from ref. [103]. Copyright (2015) by the American Physical Society.

Second harmonic generation is a special case of a sum frequency generation (SFG), experimentally confirmed soon after the first SHG experiment.[105] In addition to SFG, where output photons have an energy which is the sum of the energy of the photons from the fundamental beams, light in the nonlinear material give rise to the analogous difference frequency generation. All these wave mixing processes extended the capabilities of laser systems by broadening the usable light spectrum. In addition to this application, SFG and SHG are used now as imaging and spectroscopic techniques.

The source of SHG is the interaction of light with matter resulting in the nonlinear response. An electric field $\vec{E}$ passing through a material will cause a displacement of charges within it. The dipole moment induced in this way, which per unit volume is called polarization $\vec{P}$, and is proportional to the applied electric field. For the conventional linear relation, the polarization vector can be expressed as

$$\vec{P} = \epsilon_0 \chi^{(1)} \vec{E} \tag{2.1}$$

where ϵ_0 is the permittivity of free space. The polarization and the electric field are related by the linear susceptibility $\chi^{(1)}$, which is a measure of the ability of matter to be polarized by the applied field. For an oscillating electric field, as in the case of an optical wave, the induced dipole will oscillate and become a source of radiation itself. However, the relationship described by equation (2.1) is only true when the electric field is weak. In reality, the polarization is more complicated, and can be split into a linear response and a series of additional nonlinear responses as shown in equation (2.2). For simplicity, we only consider the case where the nonlinear response P is

parallel to the electric field E, and therefore the vector nature of $\vec{P}$ and $\vec{E}$ can be neglected.

$$P = \epsilon_0 (\chi^{(1)} E + \chi^{(2)} E^2 + \ldots) = P^{(1)} + P^{(2)} + \ldots \tag{2.2}$$

where $\chi^{(2)}$ is a second order nonlinear susceptibility. The higher terms of equation (2.2) are responsible for nonlinear response of the material. Typical values of the linear susceptibility $\chi^{(1)}$ are in order of 1 mV^{-1}, while the second order susceptibilities $\chi^{(2)}$ are in order of 10^{-12} mV^{-1}. For this reason, it was only possible to observe nonlinear effects after the invention of lasers, which provided high enough electric field strengths. The second term of the equation (2.2) is responsible for the second order nonlinear processes, such as SHG, which are quadratic with the applied electric field. For a monochromatic optical wave of frequency, ω, and wave amplitude, E_0, the second order polarization is

$$
\begin{aligned}
P^{(2)} &= \epsilon_0 \chi^{(2)} E_0^2 \cos^2(\omega t) \\
&= \epsilon_0 \chi^{(2)} E_0^2 \left(\frac{1}{2} + \frac{1}{2} \cos(2\omega t) \right) \\
&= \frac{\epsilon_0 \chi^{(2)} E_0^2}{2} + \frac{\epsilon_0 \chi^{(2)} E_0^2 \cos(2\omega t)}{2}
\end{aligned}
\tag{2.3}
$$

The first term obtained in equation (2.3) is responsible for the optical rectification effect, in which a static electric polarization is generated in the medium. The second term is a source of radiation with double the frequency.

Due to symmetry restrictions governing $\chi^{(2)}$, not every medium will result in observable nonlinear response. In materials which possess a centre of inversion, the $\chi^{(2)}$ tensor is zero. This is a significant feature since 11 of the 32 crystal symmetry groups, as well as isotropic liquids that are considered in this work, are centrosymmetric. The inversion symmetry operation will change the sign of both the applied electric field and the polarization. The second order polarization of the form as in equation (2.2) is then:

$$-P^{(2)} = \epsilon_0 \chi^{(2)} \left(-E\right)^2$$

$$= \epsilon_0 \chi^{(2)} E^2$$

(2.4)

Combining this with the expression $P^{(2)} = \epsilon_0 \chi^{(2)} E^2$, it can be noticed that $\chi^{(2)} = -\chi^{(2)}$ which can only be fulfilled if $\chi^{(2)}$ is zero. Therefore, for media with inversion symmetry, even-order nonlinear processes are forbidden.

Second harmonic and sum frequency generation are described in detail in standard textbooks, on which the description presented here was mostly based.[106-109] Additionally, their use to study adsorbates at interfaces was extensively presented in number of excellent reviews.[110-114]

Anharmonic oscillator model

The response of the material can be explained by an anharmonic oscillator model. In this model, the medium consists of N oscillators per unit volume with characteristic resonant frequencies. Such oscillators can represent an electron bound to a nucleus in an asymmetric environment. In the case of a small driving field, it can be assumed that the displacement of the electron is small so that it can be described well by a harmonic oscillator. The equation of motion of the electron position due to the electromagnetic wave for a noncentrosymmetric medium is

$$\frac{d^2 x}{dt^2} + 2\gamma \frac{dx}{dt} - \frac{F_{\text{restoring}}}{m} = -\frac{eE(t)}{m}$$

(2.5)

where $-e$ is the charge of the electron, m is mass of the electron, γ is a damping rate, and $x = 0$ corresponds to the equilibrium position of the electron. The first term on the left hand side is the acceleration, the second is a damping force and the last one is a restoring force for displacements from the equilibrium. The restoring force considering linear response (harmonic oscillator) takes the form

$$F_{\text{restoring}} = -m\omega_0^2 x$$

(2.6)

where ω_0 is the natural resonant frequency of the material. However, when the driving field becomes strong, the displacement becomes large and it does not vary linearly with

driving field anymore. To account for this, a correction expressing the nonlinearity is introduced, which is the source of the nonlinear response of the system. The restoring force for a noncentrosymmetric medium can be described by

$$F_{\text{restoring}} = -m\omega_0^2 x - max^2 \tag{2.7}$$

where a is a parameter characterizing the strength of the nonlinearity. The second term in equation (2.7) expresses the nonlinear correction to the restoring force. The restoring force of such form corresponds to a potential energy function (Figure 2.2)

$$U(x) = -\int F_{\text{restoring}} dx = \frac{1}{2} m\omega_0^2 x^2 + \frac{1}{3} max^3 \tag{2.8}$$

The first term in the equation (2.8) corresponds to the harmonic potential, while the second term is an anharmonic correction term for the noncentrosymmetric medium.
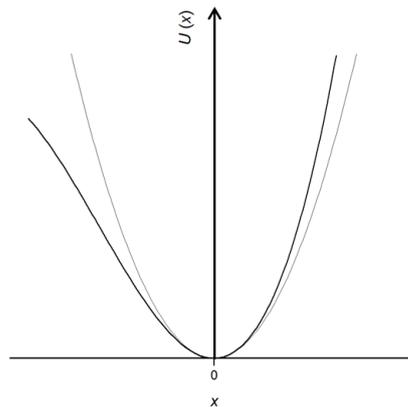
Figure 2.2. Potential energy functions for a noncentrosymmetric medium (thin line shows the parabolic potential well, which corresponds to the harmonic oscillator).

The driving field of the electromagnetic field $E(t)$ in equation (2.5) is assumed to be a monochromatic optical wave of form:

$$E(t) = E_0 \cos\omega t = \frac{1}{2} E_0 (e^{i\omega t} + e^{-i\omega t}) \tag{2.9}$$

The response of the medium in form of the second harmonic at frequency 2ω, allows the time-dependent electron displacement to be written as

$$x(t) = \frac{1}{2}(X_1 e^{-i\omega t} + X_2 e^{-2i\omega t} + \text{c.c.}) \tag{2.10}$$

where c.c. stands for complex conjugate. By inserting the above driving field (equation (2.9)) and electron displacement (equation (2.10)) into the equation of motion of the electron in the field (equation (2.5)), we obtain

$$\left(\omega_0^2 - \omega^2 - i\gamma\omega\right)\frac{(X_1 e^{-i\omega t} + \text{c.c.})}{2} + \left(\omega_0^2 - 4\omega^2 - 2i\gamma\omega\right)\frac{(X_2 e^{-2i\omega t} + \text{c.c.})}{2}$$

$$+ \frac{a}{4}\left(X_1^2 e^{-2i\omega t} + 2X_1 X_2 e^{-i\omega t} + X_2^2 e^{-4i\omega t} + \text{c.c.}\right) \tag{2.11}$$

$$= \frac{-eE_0}{2m}(e^{-i\omega t} + \text{c.c.})$$

Assuming that the nonlinear response is small compared to the linear one, so that the ω term in the anharmonic part can be neglected, and considering terms only at frequencies ω and 2ω, X_1 can be extracted:

$$X_1 = \frac{-eE_0}{m}\frac{1}{(\omega_0^2 - \omega^2 - i\gamma\omega)} \tag{2.12}$$

This is exactly what would be obtained from the harmonic oscillator. The polarization caused by the displacement at frequency ω is given by

$$P(\omega,t) = -Nex(\omega,t) = -\frac{Ne}{2}(X_1 e^{-i\omega t} + \text{c.c.}) \tag{2.13}$$

where N is the number density of particles. By comparing this expression with the one given earlier for polarization in equation (2.1), and inserting the amplitude of the displacement in form of equation (2.12), the expression for the linear susceptibility can be obtained

$$\chi^{(1)}(\omega) = \frac{Ne^2}{m\epsilon_0}\frac{1}{(\omega_0^2 - \omega^2 - i\gamma\omega)} \tag{2.14}$$

The displacement due to the nonlinear response can also be obtained from equation (2.11). If the coefficients of $e^{-2i\omega t}$ from equation (2.11) are extracted, one obtains:

$$\left(\omega_0^2 - 4\omega^2 - 2i\gamma\omega\right)\frac{X_2}{2} + \frac{aX_1^2}{4} = 0 \tag{2.15}$$

By the using equation (2.12) and (2.14), the nonlinear displacement is obtained

$$X_2 = -\frac{aX_1^2}{2\left(\omega_0^2 - 4\omega^2 - 2i\gamma\omega\right)}$$

$$= -\frac{ae^2 E_0^2}{2m^2 \left(\omega_0^2 - \omega^2 - i\gamma\omega\right)^2 \left(\omega_0^2 - 4\omega^2 - 2i\gamma\omega\right)} \tag{2.16}$$

$$= -\frac{ma\epsilon_0^3 \chi(\omega)^2 \chi(2\omega)}{2N^3 e^4} E_0^2$$

Analogously with equation (2.13), the polarization at frequency 2ω is

$$P(2\omega,t) = -Nex(2\omega,t) = -\frac{Ne}{2}(X_2 e^{-2i\omega t} + \text{c.c.}) \tag{2.17}$$

The second order polarization from equation (2.2) generated by a driving field at frequency ω (equation (2.9)) is

$$P(2\omega,t) = \epsilon_0 \chi^{(2)} E(t)^2 = \epsilon_0 \chi^{(2)} \left(\frac{E_0}{2}\right)^2 (e^{-2i\omega t} + \text{c.c.}) \tag{2.18}$$

In a similar manner as for linear susceptibility, by combining equations (2.16), (2.17) and (2.18), the expression for the second order nonlinear susceptibility is obtained:

$$\chi^{(2)} = \frac{ma\epsilon_0^2 \chi(\omega)^2 \chi(2\omega)}{N^2 e^3}$$

$$= \frac{ma\epsilon_0^2}{N^2 e^3} \frac{1}{\left(\omega_0^2 - \omega^2 - i\gamma\omega\right)^2 (\omega_0^2 - 4\omega^2 - 2i\gamma\omega)} \tag{2.19}$$

Equation (2.19) shows that, when the frequency of the applied optical wave ω or its second harmonic 2ω matches (is resonant with) the natural frequency of the material ω_0, the value of the second order susceptibility $\chi^{(2)}$ is greatly enhanced. Furthermore, $\chi^{(2)}$ is a complex number, and thus it is possible to distinguish the real and imaginary parts of it.[115] For example, a resonant species gives mostly an imaginary response, while a non-resonant medium gives real response. Therefore, the two can be distinguished if the real and imaginary parts can be distinguished.

2.1 Surface second harmonic generation

Even-order nonlinear processes are forbidden in media with a centre of inversion. However, while this is true for the bulk centrosymmetric medium, at the interface between two such media, the centrosymmetry is broken. Therefore, the response in the form of SHG from a medium with inversion symmetry arises specifically from the surface (in an electric dipole approximation, which will be discussed briefly later). This fact means that second order processes like SHG or SFG are ideal tools for studying surfaces. In the following section, the symmetry arguments showing the surface origins of SHG between two centrosymmetric media are presented.

The first experiment measuring SHG in the reflection geometry from a medium with inversion symmetry was performed in 1965 by Brown *et al*.[116] They later discovered that the SHG signal they collected from the thin layer of silver was strongly affected by surface contamination.[117] A similar result was obtained in 1973 by Chen *et al*., where the SHG signal in reflection from Ge was drastically increased by adsorption of submonolayers of Na.[118] These results indicated that the SHG signal from the surface might have monolayer sensitivity.[117, 119] Despite these early studies, SHG was not appreciated much as a technique for studying interfaces for some time. Then, inspired by the development of surface enhanced Raman scattering in 1974, the aforementioned abilities of SHG to scan surface properties started to be extensively expanded in 1980s.[120] In 1982 Heinz *et al*. showed that surface SHG is capable of providing information on the spectra and orientation of adsorbates at the interfaces of centrosymmetric media.[121, 122] This was followed by the measurement of kinetics of adsorption either on solid or liquid surfaces.[123, 124] It was shown that SHG can be used to probe basically any surface that is accessible by light, be it situated in ultra-high vacuum or under ambient conditions, and even from buried interfaces.[125] SHG has become a powerful technique in studying interfaces with new applications being constantly developed.

Symmetry

The second order nonlinear susceptibility is a third rank tensor and thus has 27 elements. However, because of the nature of the $\chi^{(2)}$ and the symmetry of the media, the number of the independent elements can be significantly reduced. For example, for a centrosymmetric medium this number becomes zero.

The second order polarization for SFG, including the tensor form of the susceptibility, can be written as

$$P_i^{(2)}(\omega_3) = \epsilon_0 \chi_{ijk}^{(2)}(\omega_3; \omega_1, \omega_2) E_j(\omega_1) E_k(\omega_2) \tag{2.20}$$

where ω_3 is the resulting frequency ($\omega_3 = \omega_1 + \omega_2$) and ω_1 and ω_2 are the incident frequencies. In the expression (2.20), the indices j, k, 1 and 2 do not appear on the left side of the equation and are so-called dummy indices. Thus, the pairs (j, ω_1) and (k, ω_2) can be exchanged with each other. It does not matter which of the incident fields, E_j or E_k, is indicated as the first one. This property is called intrinsic permutation symmetry. For SHG the incident beams are equal ($\omega_1 = \omega_2$). This means that the 27 elements of the $\chi_{ijk}^{(2)}$ tensor are reduced to 18 independent elements.

The number of tensor elements can be further reduced by considering Kleinman's symmetry. In the case that the frequencies of the light are far from any resonance frequency of the material, the nonlinear susceptibility is independent of frequency. As a consequence, all the indices of the $\chi_{ijk}^{(2)}$ can be freely interchanged without changing the corresponding frequencies. Because of this, there are now only 10 independent terms of the nonlinear susceptibility $\chi^{(2)}$. However, Kleinman's symmetry does not apply to the majority of the performed SHG or SFG experiments, including the investigation presented in this thesis, since the incident radiation (or its second harmonic) has a frequency close to a resonance of the studied species.

The final number of non-zero elements of the susceptibility tensor will depend on the medium considered. Neumann's principle states that, if the crystal is unchanged due to a symmetry operation, its physical properties (in this case the second order susceptibility tensor elements) must also be unchanged by the same symmetry operation.[126] Thus, the number of $\chi^{(2)}$ tensor elements can be reduced if the material

has a spatially symmetric organisation so that, after rotation about an axis, reflection across a plane or inverted through a point, an identical arrangement is obtained. The interface between two isotropic media (like the water/air interface) has ∞m spatial symmetry. This means that, if the surface lies in the xy plane and z is normal to the surface, the arrangement of the interface stays unchanged with any rotation around z axis and a reflection across any plane containing the z-axis. This structure has the same property as for 4mm or 6mm symmetries and thus the nonvanishing elements for the interface can be found in tables under these symmetries. Due to the Neumann's principle, the second order susceptibility at the interface between two centrosymmetric media after considering the reflection operations has only 7 non-zero elements:

$$\chi_{xxz}^{(2)}, \chi_{xzx}^{(2)}, \chi_{yyz}^{(2)}, \chi_{yzy}^{(2)}, \chi_{zxx}^{(2)}, \chi_{zyy}^{(2)}, \chi_{zzz}^{(2)} \tag{2.21}$$

However, the rotation around z axis and the fact that the order of the input fields does not matter results in only 3 independent elements that are non-zero:

$$\chi_{xxz}^{(2)} = \chi_{yyz}^{(2)} = \chi_{xzx}^{(2)} = \chi_{yzy}^{(2)}$$
$$\chi_{zxx}^{(2)} = \chi_{zyy}^{(2)} \tag{2.22}$$
$$\chi_{zzz}^{(2)}$$

Fresnel equations for SHG at interfaces

The second-order nonlinear response of the medium due to the symmetry breakage at the surface has contributions originating essentially from one to a few molecular layers of the medium. The interface can be thought of as a three layer system, where the middle layer represents the surface, contributing to the nonlinear response located between two isotropic bulk media. Since the surface layer is much thinner than the wavelength of the driving field, it can be assumed that it has a thickness approaching zero. The interfacial layer with a dielectric constant ϵ', is positioned at $z = 0^+$, embedded between medium 1 with ϵ_1 and medium 2 with ϵ_2, and has the same refractive index as medium 2 (Figure 2.3). The second harmonic at 2ω is generated from the interfacial layer in both reflection and transmission, however, for the purposes of this work only the reflected direction is considered.
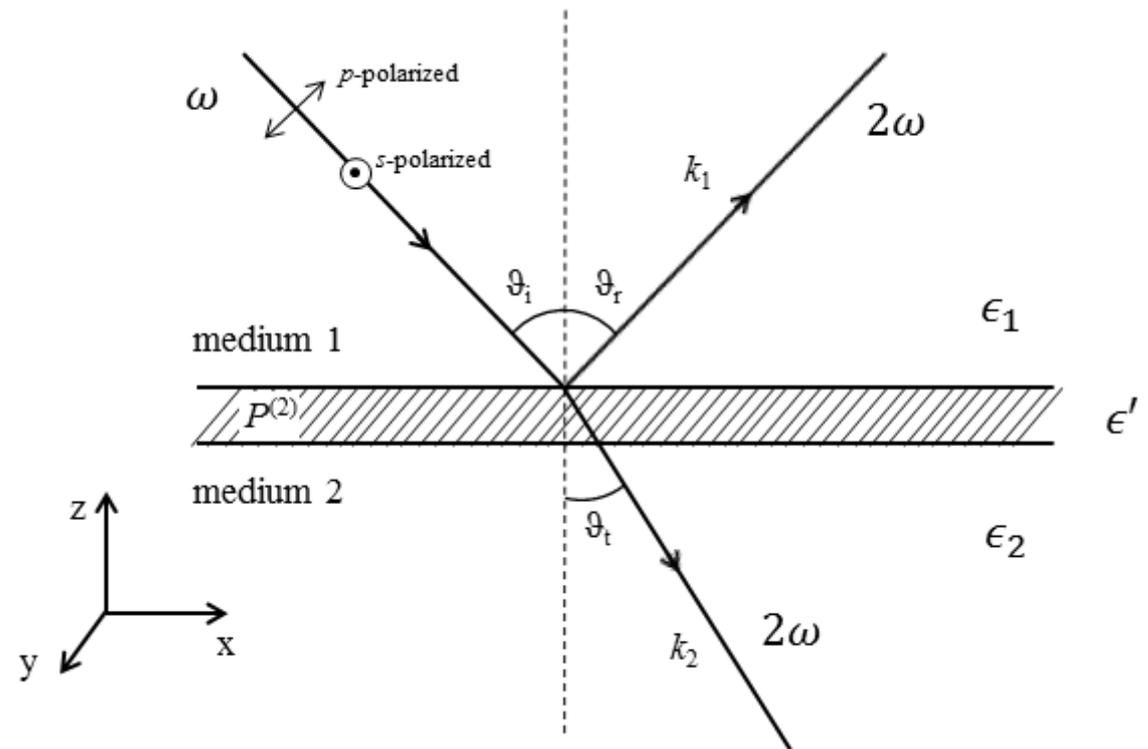
Figure 2.3. Scheme of the second harmonic generation from the interface between two isotropic media.

The theory behind the generation of harmonics from the boundary of two media was first introduced by Bloembergen *et al.*.[127] They showed that the direction of the generated harmonics, similarly to the case of the linear response, can be obtained following Snell's law. Therefore, in the case of SHG the generated beam in reflection at 2ω follows the reflected fundamental beam at ω, when the medium of propagation is a dispersionless material. The intensity and polarisation conditions can be described by the Fresnel equations.

The radiated electric field generated by the nonlinear response of the surface layer can be obtained from the solution to the wave equation, which can be derived from Maxwell's equations [106]:

$$\nabla \times \left(\nabla \times \vec{E} \right) + \frac{\epsilon}{c^2} \frac{\partial^2}{\partial t^2} \vec{E} = -\frac{4\pi}{c^2} \frac{\partial^2}{\partial t^2} \vec{P}^{(2)} \tag{2.23}$$

with

$$\nabla \cdot \epsilon \vec{E} = -4\pi \nabla \cdot \vec{P}^{(2)}$$

Fields generated from such interfaces have to obey boundary conditions, which require continuity of the electric and magnetic field components along the plane of the surface and the displacement current component along the normal to the surface [128, 129]:

$$\int_{0^-}^{0^+} \vec{E}_{\parallel}(x, y) dz = \int_{0^-}^{0^+} \vec{B}_{\parallel}(x, y) dz = 0 \tag{2.24}$$

$$\int_{0^+}^{0^-} \vec{E}_z(x, y) dz = -\frac{4\pi}{\epsilon'} P_z(x, y) \tag{2.25}$$

The relations between the fields on the opposite sides of the interface layer are then:

$$\Delta B_x = -i4\pi \frac{\omega}{c} P_y$$

$$\Delta B_y = +i4\pi \frac{\omega}{c} P_x$$

$$\Delta B_z = 0$$

$$\Delta E_x = -\frac{4\pi}{\epsilon'} \frac{\partial P_z}{\partial x} \tag{2.26}$$

$$\Delta E_y = -\frac{4\pi}{\epsilon'} \frac{\partial P_z}{\partial y}$$

$$\Delta D_z = -4\pi \left(\frac{\partial P_x}{\partial x} + \frac{\partial P_y}{\partial y} \right)$$

With these boundary conditions (2.26), the p- (parallel to the plane of incidence) and s-polarized (perpendicular to the plane of incidence) components of the second harmonic electric field can be derived from the solution to the wave equation (2.23). The s-polarized wave is created only by the *y* component of the nonlinear polarization, while p-polarized SHG arises from both the *x* and *z* components (Figure 2.3). This gives the s- and p-electric fields of the second harmonic in medium 1 as [129]:

$$E_s(2\omega) = i4\pi k_1 \frac{\left(\dfrac{1}{\epsilon_1}\right)k_1 P_y^{(2)}}{k_{1z} + k_{2z}}$$

(2.27)

$$E_p(2\omega) = i4\pi k_1 \frac{k_{2z} P_x^{(2)} + \left(\dfrac{\epsilon_2}{\epsilon'}\right)k_x P_z^{(2)}}{\epsilon_2 k_{1z} + \epsilon_1 k_{2z}}$$

where k_{ij} is a wave vector in medium 1 and medium 2 for $i = 1$ and 2, respectively, with $j = x$ or z indicating the component of the wave vector in the laboratory coordinate system. For example $k_{2z} = k_2 \cos\vartheta_t$, where ϑ_t is an angle of the transmitted wave in medium 2 to the normal, which can be obtained from Snell's law (Figure 2.3).

The components of the second order polarization seen in equations (2.27) can be selected by choosing the combination of the polarization of the incident and detected second harmonic beams. According to the nonvanishing susceptibility tensor elements shown in equation (2.22), the only allowed polarization combinations are:

PS: $$P_z^{(2)}(2\omega) = \epsilon_0 \chi_{zxx}^{(2)} E'_y(\omega) E'_y(\omega)$$

Smix: $$P_y^{(2)}(2\omega) = \epsilon_0 \chi_{xxz}^{(2)} E'_y(\omega) E'_z(\omega)$$

(2.28)

PP: $$P_z^{(2)}(2\omega) = \epsilon_0 \left(\chi_{zzz}^{(2)} E'_z(\omega) E'_z(\omega) + \chi_{zxx}^{(2)} E'_x(\omega) E'_x(\omega) \right)$$

$$P_x^{(2)}(2\omega) = \epsilon_0 \chi_{xxz}^{(2)} E'_x(\omega) E'_z(\omega)$$

where $E'(\omega)$ represents the local electric field within the interfacial layer. The calculation of $E'(\omega)$ from the incident electric field in medium 1, $E(\omega)$, is discussed later in this section. The convention of indicating the polarization combinations as shown above will be used throughout this work. That is, output polarisation is stated before input polarisations. This is similar to the case of SFG, where polarizations are most commonly written for each beam in order of highest to lowest frequency. Thus, usually the first letter indicates the polarization of the SFG beam, the second represent the polarization of the visible input beam, while the last represents the polarisation of the input IR beam. Because in SHG there is only one input beam, only two letters are used. The term 'mix' in the Smix polarization combination stands for a polarization set

up between p- and s-polarization, which results in the combination of these polarizations, equivalent to the SSP and SPS polarization combinations in SFG experiments.

The nonlinear polarization components in equation (2.28) are characterized by the components of the local electric field in the interface layer $E'_i(\omega)$ and not by the electric field of the incident beam. As the electric field travels from medium 1 into the interfacial layer, its amplitude changes. The relation between the electric field in the interfacial layer and that of the incident beam can be described by the transmission Fresnel coefficients [130]:

$$t_s = \frac{2\sin\vartheta_t\cos\vartheta_i}{\sin(\vartheta_i + \vartheta_t)}$$

$$t_p = \frac{2\sin\vartheta_t\cos\vartheta_i}{\sin(\vartheta_i + \vartheta_t)\cos(\vartheta_i - \vartheta_t)}$$

(2.29)

The boundary conditions state the continuity of the electric field along the surface and electric displacement normal to the surface. The relation between the electric field in medium 2 and the interface can be written as:

$$E_{2x}(\omega) = E'_x(\omega)$$

$$E_{2y}(\omega) = E'_y(\omega)$$

$$E_{2z}(\omega) = -\frac{\epsilon'}{\epsilon_2}E'_z(\omega)$$

(2.30)

Using the transmission coefficients equations (2.29) and relations in equations (2.30), the components of the electric field in the interface layer can be expressed as:

$$E'_x(\omega) = t_p E_p \cos\vartheta_t$$

$$E'_y(\omega) = t_s E_s$$

$$E'_z(\omega) = -\frac{\epsilon_2}{\epsilon'}t_p E_p \sin\vartheta_t$$

(2.31)

The expressions for the electric field components in equations (2.31) can be combined with the nonlinear polarization components in equation (2.28) and equations (2.27) to give the relation between the electric field of the SHG and incident beam. This can be then used to calculate the intensity of the SHG detected in reflection from the interface

layer due to the intensity of the incident beam. For a plane wave in a medium with dielectric constant ϵ, the intensity is

$$I = \frac{c\epsilon_i^{1/2}}{2\pi} |E|^2 \qquad (2.32)$$

After some manipulation, the following expression can be obtained (the description of the derivation for the below equation is presented in [131]):

$$I(2\omega) = \frac{32\pi^3\omega^2 \sec^2\vartheta_r}{c^3\epsilon_1^{1/2}(2\omega)\epsilon_1(\omega)} \left| L(2\omega) \cdot \chi^{(2)} : L(\omega)L(\omega) \right|^2 I_i^2(\omega) \qquad (2.33)$$

where ϑ_r is the angle of the second harmonic reflected from the surface to the normal, I_i is the intensity of the input beam and $L(\omega)$ is a Fresnel factor for the field (factors of the field from equation (2.31), $L(\omega) = E'_j(\omega)/E_k$ with $j = x, y, z$ and k indicating polarization s or p).

The information concerning the molecules at the surface are contained in the second order susceptibility $\chi^{(2)}$, which is a macroscopic value that can be related to the molecular structure by

$$\chi^{(2)} = N < \beta > \qquad (2.34)$$

where N is the number of molecules at the interface and β is the so-called hyperpolarizability, with brackets $<>$ denoting the averaging over all orientations.

Relation (2.34) indicates that, by experimentally measuring the intensity of the SHG signal, the concentration of the surface molecules can be measured. Moreover, if frequency dependent measurements are performed, then information on electronic and vibrational energy levels of interfacial molecules can be obtained. By the appropriate selection of the polarization combinations, specific tensor elements of the nonlinear susceptibility $\chi^{(2)}$ can be measured, which can be related to the orientation of molecules at the interface. Additionally, when phase information (i.e. $\chi^{(2)}$ is known, rather than $|\chi^{(2)}|^2$) is obtained, the absolute orientation of the molecule can be determined. Any of these measurements recorded as a function of time additionally yields in information on dynamics of molecules at the interface.[111]

The information described above can be obtained for species adsorbed at the interface. Signal from such an adsorbate can be greatly enhanced, as was shown earlier in equation (2.19), if the fundamental beam or its second harmonic is resonant with an electronic or vibrational transition of the adsorbate. In that case, the detected signal is dominated by the response from the adsorbate. Additionally, when the phase of the generated second harmonic electric field is measured, it is possible to separate the real and imaginary parts of $\chi^{(2)}$, and thus the nonresonant background from the resonant part arising from adsorbed species.

Contributions to the surface second harmonic generation

The phenomena presented throughout this work are described using the electric dipole approximation, where only the electric dipole response is considered. In reality, the response of the material can also arise from magnetic and higher electric multipoles, which can have different properties from the electric dipole. The general form of the effective second order polarization in a multipole expansion is [132]:

$$P_{\text{eff}}^{(2)}(2\omega) = P^{(2)}(2\omega) - \nabla Q^{(2)}(2\omega) + \frac{c}{i2\omega}\nabla \times M^{(2)}(2\omega) + \ldots \qquad (2.35)$$

where second and third terms gives the response due to electric quadrupole and magnetic dipole field, respectively. In the bulk of a centrosymmetric media, the electric dipole contribution to the $P_{\text{eff}}^{(2)}$ and the contribution from $M^{(2)}$ vanish for SHG.[133] However, the SHG signal can still contain electric quadrupole contributions from the bulk. Therefore, besides the surface response, where the electric dipole contribution dominates, the SHG signal in reflection contains an electric quadrupole contribution originating from the bulk. Although the probability of the quadrupole transition is much lower than for the dipole transition, there are many more molecules in the bulk than at the interface, which contribute to the quadrupole response. Because of this, the quadrupole response from the bulk can contribute to the SHG signal as much as the dipole response from the interface.[134-136] For s-polarized SHG however, due to the lack of electric field gradient in the "s-axis" it is not possible to generate electric quadrupole polarisations from the medium the beams are reflected from and, hence, the bulk contribution to the signal can be rule out for this case.[137, 138] Additionally, in some cases the contributions beyond the electric dipole can be neglected compared with

the electric dipole response and the electric dipole approximation can be applied. This is true, for example, in cases where adsorbates are studied at the surface, the response of which is resonantly enhanced (see equation (2.19)).[137, 139-141]

2.2   Interference second harmonic generation

It was shown before in equation (2.34) that information about interfacial molecules can be obtained in SHG measurements through $\chi^{(2)}$. However, equation (2.33) shows that, what is measured in the standard SHG measurement is the square of the second order susceptibility. As a consequence, the measured signal depends quadratically on the concentration. Additionally, when a specific adsorbate on the surface is being studied through resonant enhancement, two terms contribute to the effective second order susceptibility:

$$\chi_{\text{eff}}^{(2)} = \chi_{\text{R}}^{(2)} + \chi_{\text{NR}}^{(2)} \tag{2.36}$$

where $\chi_{\text{R}}^{(2)}$ contains resonant contributions and $\chi_{\text{NR}}^{(2)}$ all other non-resonant contributions arising from the nascent interface. The signal measured in a SHG experiment is then:

$$S_{\text{SHG}} \propto |\chi_{\text{R}}^{(2)} + \chi_{\text{NR}}^{(2)}|^2 = \left[\left| \chi_{\text{R}}^{(2)} \right|^2 + \left| \chi_{\text{NR}}^{(2)} \right|^2 + 2 \left| \chi_{\text{R}}^{(2)} \right| \left| \chi_{\text{NR}}^{(2)} \right| \cos \varphi \right] \tag{2.37}$$

The interference term between $\chi_{\text{R}}^{(2)}$ and $\chi_{\text{NR}}^{(2)}$ means that, when measuring resonance-enhanced S_{SHG} of an adsorbate (which is contained in $\chi_{\text{R}}^{(2)}$), the signal can depend on the surface concentration N (see equation (2.34)) to any power between 1 and 2. For example, $S_{\text{SHG}} \propto N^2$ in the limit when $\chi_{\text{R}}^{(2)} \gg \chi_{\text{NR}}^{(2)}$, while $S_{\text{SHG}} \propto N$ in the limit when $\chi_{\text{R}}^{(2)} \ll \chi_{\text{NR}}^{(2)}$. Thus, a direct comparison of measured parameters to those from the bulk using traditional methods such as absorption spectroscopy, where the measured signal is a linear representation of the concentration, becomes impossible. It also means that, a weak $\chi^{(2)}$ signal becomes even weaker after being squared. Also information about the sign of $\chi^{(2)}$, which indicates the up versus down orientation of the adsorbate at the interface, are lost in a standard SHG measurement. Furthermore, a simple SHG experiment is not able to provide phase information which, as mentioned before, can be

used in order to obtain real and imaginary parts of the $\chi^{(2)}$, and thus separate interfering resonant signal of the adsorbate from nonresonant background.

These downsides of conventional SHG measurements can be resolved by introducing an additional reference field, called the local oscillator (LO), which interferes with the SHG signal from the sample. Experiments using this idea are described in the literature as interference SHG, phase-sensitive SHG, or heterodyne detected SHG (as opposed to "homodyne detected" for the conventional SHG measurement). The signal detected in such a manner is then:

$$S_{\text{SHG}} \propto \left|\chi_{\text{S}}^{(2)} + \chi_{\text{LO}}^{(2)}\right|^2 = \left|\chi_{\text{S}}^{(2)}\right|^2 + \left|\chi_{\text{LO}}^{(2)}\right|^2 + 2\chi_{\text{S}}^{(2)}\chi_{\text{LO}}^{(2)}\cos(\varphi) \qquad (2.38)$$

where φ is the phase difference between the signal and the local oscillator fields, and the subscript S signifies the surface contribution, defined by equation (2.37). As can be seen in equation (2.38), the signal, besides quadratic components from each source, also contains an interference term, which is linear with the detected signal. Moreover, the interference term contains a $\cos(\varphi)$ term, providing phase information. In addition to the linearization of the signal, introducing a strong constant local oscillator field can improve a signal to noise ratio in the case of samples generating very weak SHG (SFG) signal.[142]

The first measurement of the SHG with a reference beam was performed as early as 1965 by Chang *et al.* in order to obtain phase information, which allowed the estimation of the complex value of the second order susceptibility for a few nonlinear crystals.[143] Interference SHG was further exploited in the 1980s, where adsorbates at interfaces were studied, making it possible to distinguish the contributions to the SHG signal from the adsorbate and the solvent background.[124, 144, 145] Subsequently, SFG experiments also adopted phase-sensitive measurements and attracted considerable attention within sum-frequency vibrational spectroscopy (SFVS), in which an infrared beam experiment yields vibrational spectra of the molecules at interfaces and orientation of specific functional groups in these molecules.[146-150] The limitation of early phase-sensitive measurements was that, in order to obtain a vibrational spectrum, the IR probe beam had to be scanned over the spectral region of interest, making the measurement time consuming. This issue was overcome by the use of broadband lasers

and the collection of the entire spectrum simultaneously, both in SHG and SFG experiments.[142, 151-161] In these experiments the interference signal, between SHG from the sample and local oscillator, is separated in time by a fixed delay T, then dispersed on a multichannel detector (usually a CCD array) and thus collected in the frequency domain. Data obtained in this way contains interference fringes corresponding to the interference between the sample and LO, as can be seen in data from a p-nitroaniline film coated on a fused silica glass collected by Yamaguchi *et al*. (Figure 2.4a).[153] These spectra are then Fourier transformed into the time domain, where the terms from quadratic ($t = 0$) and interference ($t = \pm T$) terms are well separated (Figure 2.4b). Subsequently, the filtered interference term ($t = +T$) is Fourier transformed back into the frequency domain resulting in a spectrum from which the desired information can be obtained (Figure 2.4c). Additionally, in order to obtain the absolute phase, this process has to be repeated with a reference of a known phase (usually quartz) and compared with data obtained for the sample. Time-resolved experiments can also be performed in such a way, where the spectral evolution is monitored as a function of time.[160, 162-164] These experiments provide great insight into the system studied, however, they can be very time-consuming and thus requiring phase stability over several hours. This can be non-trivial, since that method requires very accurate positioning of the sample and reference beams. As a result, such experiments may become prohibitively difficult for measuring the ultrafast dynamics of species at low concentration.
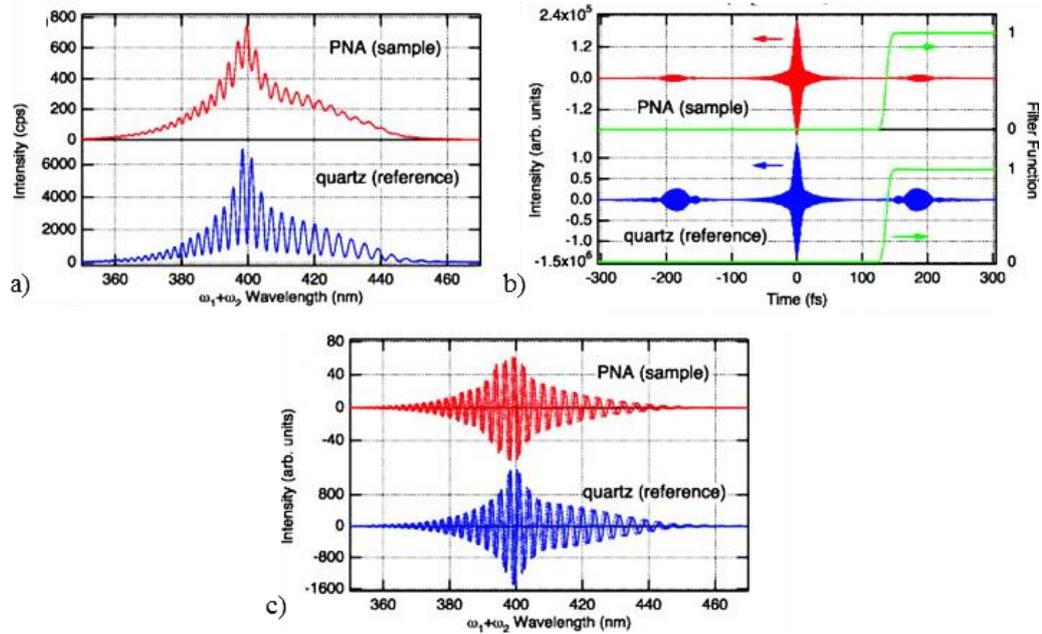
Figure 2.4. a) Raw spectrum of a p-nitroaniline film coated on fused silica glass (red) and of quartz (blue), obtained from the heterodyne detected SFG experiment. b) The same data after a Fourier transform into the time domain. The green line presents the filter function. c) The same spectra after filtered and Fourier transforming back into the frequency domain spectrum. Quartz is used as a reference in order to calibrate the phase of the measured sample. Larger fringes are present by quartz are due to the larger $|\chi^{(2)}|$ of the quartz surface. Reprinted with permission from ref. [153]. Copyright (2015), AIP Publishing LLC.

Implementation of the interference based measurements requires the introduction of an additional beam, to be used as a local oscillator. Such a beam needs to be coherent with the second harmonic (sum frequency) beam obtained from the sample. The easiest way to monitor interference is if two beams are of the same frequency. This is usually achieved by using the remaining fundamental beam in order to produce the reference beam in reflection or transmission from a material with a strong nonlinear response, located either after or before the sample. Control of the phase is then achieved by altering of the phase delay between the SHG beam from the sample and the fundamental beam. Different methods of obtaining phase measurements in the SHG experiments were reviewed by Stolle *et al.*[165] In most SHG measurements, the second harmonic produced at the sample propagates collinearly with fundamental beam and thus methods such as those presented on Figure 2.5 can be performed. All of these methods are based on virtue of the differing phase velocities of the driving field and the SHG fields in the medium through which they propagate (due to the difference in refractive index Δn at the two differing wavelengths). In the gas cell method, the beams propagate between the sample and reference in a gas cell, where the gas pressure can be

controlled resulting in a change in the difference in refractive index for ω and 2ω (Figure 2.5a). Another method is based on the variation of the distance over which the second harmonic and fundamental beams propagate together by moving the reference (Figure 2.5b). Here, the phase difference is increased when two beams travel for longer at different phase velocities. In two other methods reviewed by Stolle *et al.*, glass in form of a plate or a pair of wedges is placed between the sample and reference (Figure 2.5c,d). Glass has much higher dispersion than any gas, thus a small change in the distance the beams travel in it, achieved by rotating the plate or mutual shifting of the wedges, will have the same effect as moving the reference in the previous method.
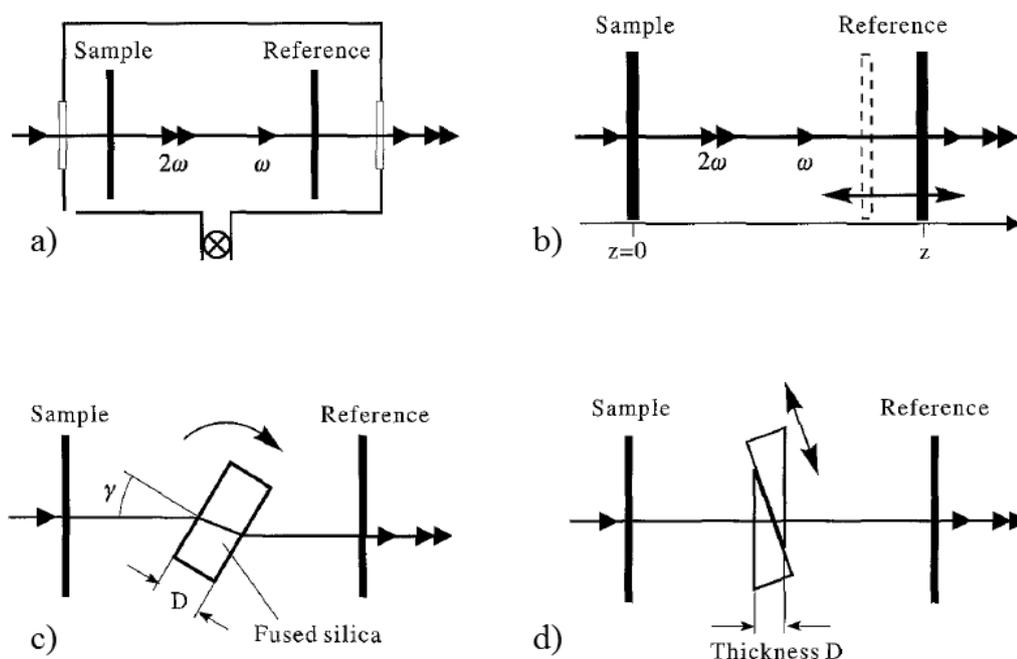
Figure 2.5. Basic schemes of four illustrative methods of controlling the phase difference in the interference SHG measurement. a) Gas cell, beams propagate in the gas cell, with the phase difference altered by a change of the gas pressure; b) variation of the distance, the phase difference is controlled here by changing the path length over which SH and fundamental beams propagate before generating the LO; c) rotating plate, both beams go through a glass or fused silica plate, and the phase is altered by change of the propagation length in glass plate, which is achieved by rotation of the plate; d) pair of wedges, both beams go through glass or fused silica wedges, the phase change controlled by adjusting the thickness D as shown. Reprinted from ref. [165] with permission of Springer.

In the case of SFG experiments, three common setups are used in order to obtain phase measurements. Phase sensitive SFG spectroscopy methods were reviewed recently by Shen.[166] In the first of these methods, all beams involved in the experiment travel collinearly. The input beams (at ω_1 and ω_2) together with the SFG

beam at the sample (at frequency ω) propagates through a phase modulator and to the reference, where the LO is generated (Figure 2.6a). In the other two setups, the beams propagate in a noncollinear way. The LO beam can be produced in a nonlinear crystal before the sample and aligned in such a way that it will propagate collinearly after the sample with the SF beam generated at the sample (Figure 2.6b). The phase in this case is set by delaying the LO beam to the SFG from the sample on the translation stage. In the last method, the input beams at ω_1 and ω_2, after generating the SFG beam at the surface, are reflected and focused with SFG beam onto a reference producing the LO beam. The phase difference is introduced by placing a glass plate between the sample and reference that only the SFG beam pass through it (Figure 2.6c). In these methods a large group velocity delay is usually introduced such that the SFG and LO pulses do not overlap in time. The interference is obtained by dispersing it onto a spectrometer, where an interference pattern is superimposed onto the spectral envelope, which depends on the temporal delay between the two pulses, as shown in Figure 2.4.
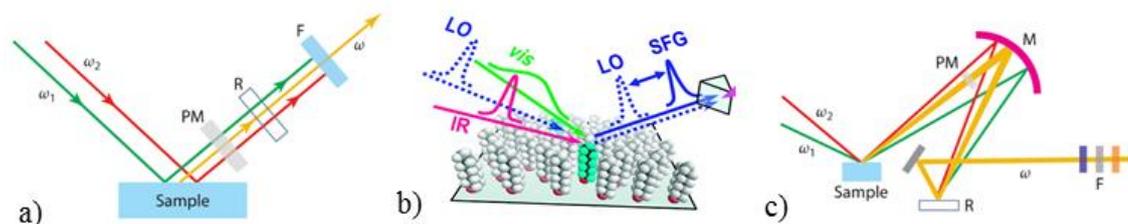
Figure 2.6. Basic schemes of the possible setups for the interference based SFG measurements. a) collinear method, input beams at ω_1 and ω_2 travel collinearly passing together with the SF beam generated at the sample through the glass plate placed between sample and reference; b) noncollinear method, in which LO is produced before the sample and is delayed by a translation stage, LO is directed onto the sample that after reflection it would propagate collinearly with, generated at the surface by the input beams traveling noncollinearly, SF beam; c) noncollinear method, in which travelling noncollinearly input beams after the sample are focused together with generated SF beam onto the reference, the delay here is introduced by placing a glass plate on the way of SF beam between sample and reference. PM- phase modulator, R- reference, F- filter, M- mirror. Adapted with permission from ref. [49]. Copyright (2015) American Chemical Society. [154, 166]

3 Experimental

Taking advantage of the surface specificity and sensitivity of SHG, we developed a technique which enables us to study the hydrated electron at the water/air interface under ambient conditions. In order to obtain data linear with concentration together with additional phase information, the experiment is an interference-based SHG. The study presented in this work concentrates on studying the dynamics of the hydrated electron, and thus the experiment is performed in a pump-probe fashion. Here, the details of the experimental design of the time-resolved phase-sensitive SHG are presented.

3.1 Femtosecond laser system

All of the laser beams used in the experiment are provided by the same commercial solid state laser system. Femtosecond laser pulses are generated in a mode-locked Ti:Sapphire oscillator (Tsunami, Spectra-Physics), pumped by a 5 W frequency-doubled continuous wave diode-pumped Nd:YVO$_4$ laser at 532 nm (Millennia Pro, Spectra-Physics). The output provided by the oscillator is a 0.5 W train of pulses at 76 MHz centred at 800 nm with a 40 nm bandwidth. This is subsequently amplified in a Ti:Sapphire regenerative amplifier system (Spitfire Pro, Spectra-Physics). Pulses from the oscillator are first stretched in duration and then selected pulses are

amplified in a Ti:Sapphire crystal, which is pumped by a diode pumped Nd:YLF pump laser (Empower, Spectra-Physics) providing ~18 W frequency doubled nanosecond pulses at 527 nm. After the amplification, pulses are compressed providing an output 3 W horizontally polarized beam of ~35 fs pulses centred at 800 nm with either 1 kHz or 950 Hz repetition rate.

In order to provide photons of the correct energy needed to study the hydrated electron, the laser beam provided by the laser system had to be divided and frequency converted. In the experiments described in the results chapter, beams at three different frequencies were used. A 250 nm beam was used as a pump beam, while beams at 1320 nm and 800 nm were used as probe beams.

250 nm pump beam

The 800 nm beam from the regenerative amplifier is split on a beam splitter BS1 (Figure 3.1). The beam reflected from BS1 is directed by two mirrors into a commercial optical parametric amplifier (OPA) (TOPAS Prime, Spectra-Physics), which can provide a tuneable signal beam in range of 1160-1600 nm (additionally it produces an idler beam in range of 1600-2600 nm). The OPA uses a small fraction (~1%) of the provided fundamental beam to produce a white light continuum (WLC) by focusing it in a sapphire plate. The WLC beam is then pre-amplified by another fraction (~5%) of the fundamental beam in a nonlinear crystal. The signal wavelength is tuned here by adjusting the delay between WLC and pump beam, and by adjusting the angle of the nonlinear crystal to achieve phase matching conditions in order to provide the most efficient amplification. The signal beam is then amplified by the majority (~94%) of the initially provided 800 nm beam in a second nonlinear crystal. The OPA outputs a vertically polarized signal, a horizontally polarized idler and the residual horizontally polarized fundamental beam at 800 nm.

The target wavelength of the pump beam for the experiments is 250 nm, which matches the lowest energy charge transfer to solvent (CTTS) transition of iodide located on the surface of water. In order to obtain this pump wavelength, the OPA was set to provide a signal beam at 1320 nm, which was then combined with the collinearly propagating residual 800 nm beam in the nonlinear crystal BBO1. The type-II sum

frequency generation process occurring in the crystal results in the generation of a vertically polarized 500 nm beam. Beams leaving the nonlinear crystal are directed to the pump-probe setup, which will be described later, where the 500 nm beam is separated from the signal and idler from the OPA and the remaining 800 nm beams. The 500 nm beam is subsequently frequency doubled in another nonlinear crystal giving the desired 250 nm pump beam.
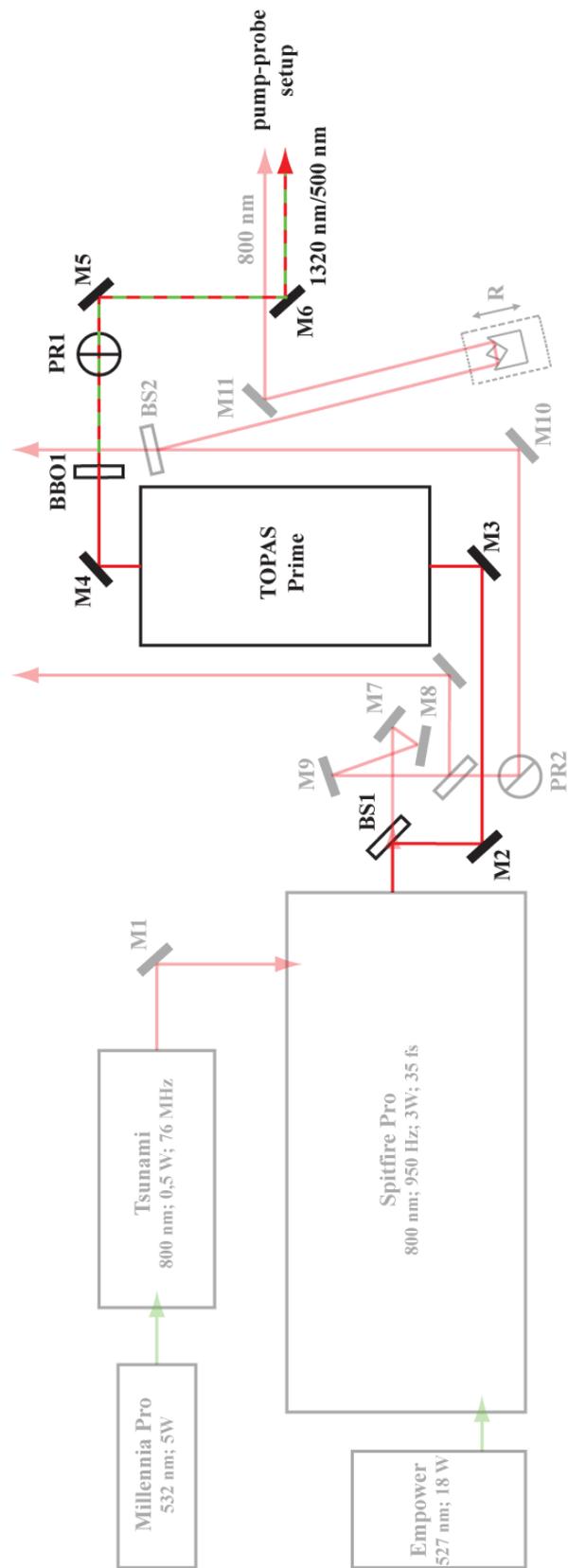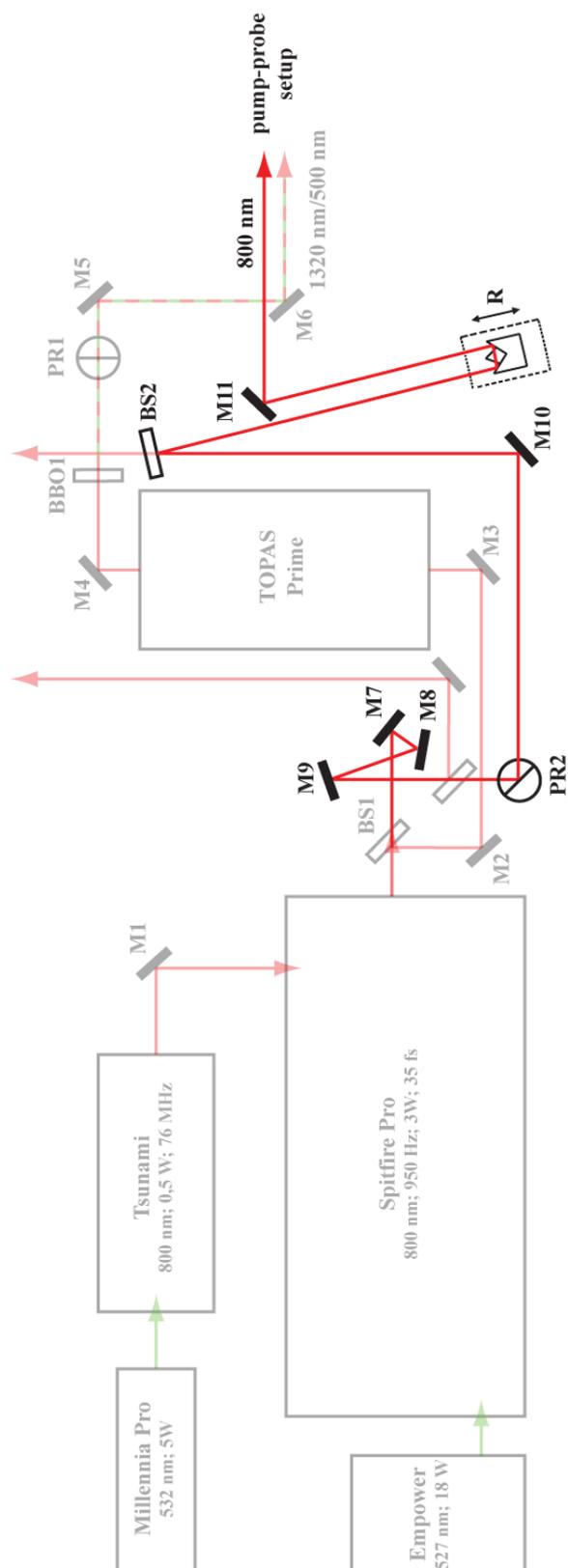
Figure 3.1. Simplified scheme of setup providing 1320 nm and 250 nm beams.

1320 nm probe beam

The 1320 nm probe beam is obtained from the OPA as described above (Figure **3.1**). The signal beam together with the idler, the 800 nm beam and the 500 nm generated in nonlinear crystal, travel to the pump-probe setup. There, it is separated from the aforementioned beams and the 1320 nm beam is used as a probe, while the idler and 800 nm beams are filtered out. In this case, since they follow the same beam path, the probe pulses match in time the pump pulses while entering the pump-probe setup (not considering dispersion in air).

800 nm probe beam

The probe beam at 800 nm is obtained directly from the laser system (Figure **3.2**). The part of the output from the amplifier separated on the beam splitter BS1 is directed into the periscope PR2 changing the polarization of the beam to vertical. Subsequently, the beam is directed onto a retroreflector, R, placed on a manual stage. The propagation length of the beam is set, with small adjustments achieved with the use of the manual stage, to match the pump pulses in time while entering the pump-probe setup.

Figure 3.2. Simplified scheme of the setup providing 800 nm beam. The path of the 800 nm beam is aligned so that it matches the 1320 nm/250 nm beams in time while entering the pump-probe setup.

3.2   Pump-probe setup

In order to observe an evolution in time of a given process, the experiment is performed in a pump-probe fashion. In this method two light pulses are used, where the first one (referred as a pump) initiates a desired process for the study, while the subsequent pulse probes the event at a given delay time. How this is achieved in the present experiments and how both beams reach the sample is described here. The specific optical elements used in the pump-probe setup are listed in Appendix A.

3.2.1   Pump

The beams, as presented before, enter the pump-probe setup and encounter a cold mirror M13 (Figure 3.4), which reflects the 500 nm beam, from which the pump will be derived, and transmits the beam used as a probe (either 1320 nm or 800 nm). The reflected pump beam is directed onto two mirrors M15-M16 located on a motorized delay stage. Mirrors M14-M17 have a coating providing high reflectance over 458-529 nm wavelength range and transmission outside of this range and this removes any residual beams. After leaving the delay stage, the pump beam reaches a concave mirror CM1. The purpose of the concave mirror here is to ensure high efficiency in the frequency conversion in a nonlinear crystal, BBO2, by concentrating beam to a smaller size. In order to avoid damage of the nonlinear crystal, the focus of the concave mirror is set several centimetres behind the crystal. Additionally, mirror CM1 enlarges the size of the pump beam on the CM2 mirror, which results in tighter focus of the pump beam on the sample. Before the pump beam reaches the nonlinear crystal BBO2, it passes through a half-wave plate WP1 and a shutter. The wave plate provides the ability to change the polarization of the pump beam. The role of the shutter will be discussed later. The conversion of the 500 nm beam into the desired 250 nm pump is accomplished by second harmonic generation in the nonlinear crystal BBO2. The output 250 nm beam from the BBO2 has polarization rotated 90° compared to 500 nm beam before the crystal, which is then rotated back 90° on the periscope PR3. The periscope PR3 and M18 consists of dielectric mirrors providing high reflectance in range over 244-257 nm wavelength and transmission outside of this range, which removes residual

500 nm. After the periscope the pump beam is directed onto a concave mirror CM2, which then focuses the beam on the sample surface.

Shutter

The shutter (Figure 3.3), which is placed in the pump beam path, is used in order to provide a background (probe-only) measurement. During the measurement, the shutter blocks the pump beam resulting in collection of data without pump beam reaching the sample. Background data collected this way allows compensation for slow changes in time resulting for example from evaporation of the liquid sample.

The mechanical shutter used in the experiment was constructed from a hard disk memory storage device.[167] A hard disk drive consists of a rotating platter, which stores data, and a read-write head assembly, which moves over the platter. The read-write head is mounted on a pivot arm, which is set in motion by a voice coil actuator. When a current is introduced to the coil, a magnetic field is produced, which reacts to the field of the permanent magnets situated on the sides of the coil. Thus, by the control of a current in the coil, the position of the arm can be adjusted, which was used in order to move the shutter. The read-write assembly was removed from the hard disk drive and mounted on an aluminum plate as shown on Figure 3.3.a. The shutter is powered by a 12 V power supply and a movement of the arm is triggered by a 5 V TTL signal from the data acquisition card (DAQ NI USB-6210, National Instruments) controlled by a computer. The schematic of the circuit for the shutter is shown on Figure 3.3.b. When 5 V is introduced from the DAQ card, the 12 V can reach the voice coil actuator and raises the shutter (made from a piece of paper card painted black) attached to the pivot arm thus blocking the pump beam. Otherwise, the 12 V cannot flow through the system and the pivot arm drops unblocking the beam.
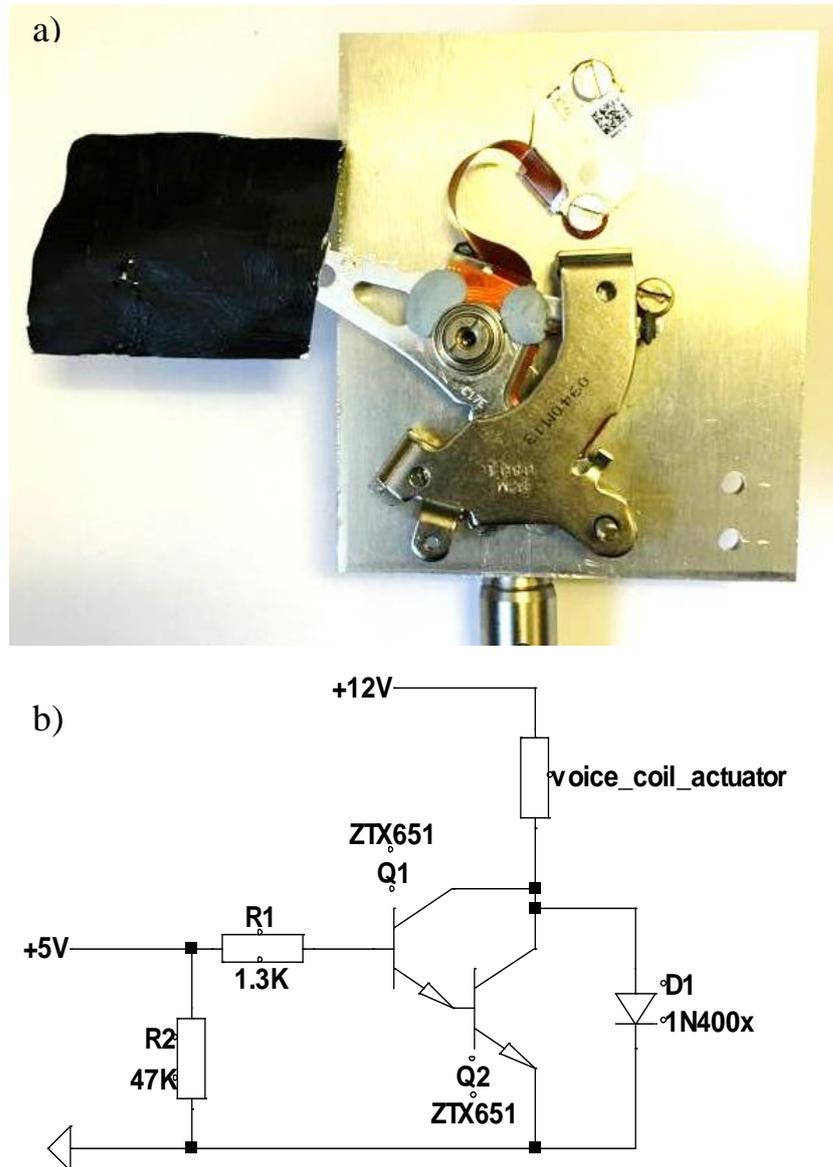
Figure 3.3. a) Picture of the shutter. b) Scheme of the circuit diagram for the shutter. A 5 V TTL input triggers transistors to enable a 12 V supply to flow through the system and thus move the shutter. R1 is 1.3 kΩ resistor, R2 is 47 kΩ resistor, Q1 and Q2 are ZTX651 bipolar (BJT) single transistors and D1 is 1N400x series diode.
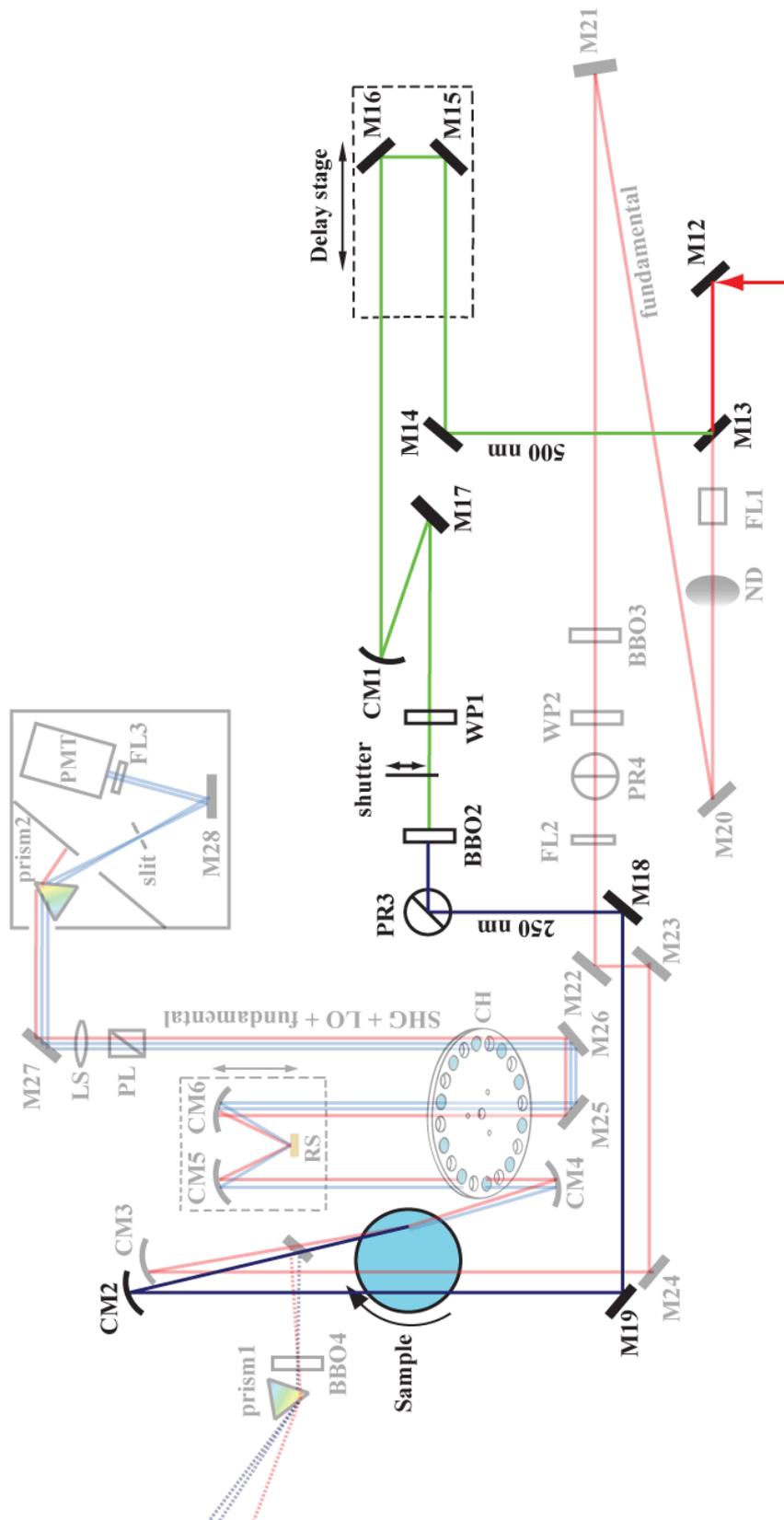
Figure 3.4. Scheme of the pump setup.

3.2.2   Probe

The probe beam, either 800 nm or 1320 nm, passes through the cold mirror M13, then is directed by set of silver mirrors M20-M24 and periscope PR4 onto a concave mirror CM3, which focus the probe beam on the sample surface (Figure 3.5). On the way to the sample the probe beam passes through a few optical elements that help to control it. A continuously variable metallic neutral density filter ND provides control of the power of the probe beam, while the half wave plate WP2 provides control of the polarization of the beam. Additionally, when using the 1320 nm as the probe beam, two filters FL1-FL2 are placed in the beam path. FL1 is a unit (supplied as part of TOPAS) consisting of two mirrors providing high reflectance in range over 1110-1600 nm, which removes residual idler and 800 nm from the beam path, while FL2 is a long pass filter providing additional filtering, removing the 800 nm beam and any other colours that might be present in the beam generated in TOPAS. For alignment purposes, a nonlinear crystal BBO3 can be placed in the beam path. The frequency doubled probe beam is easily visible by eye, which significantly aids alignment of the interference and detection setups. The beam path of the probe beam, as shown on Figure 3.5 is designed in a way to match the pump beam in time at the sample.
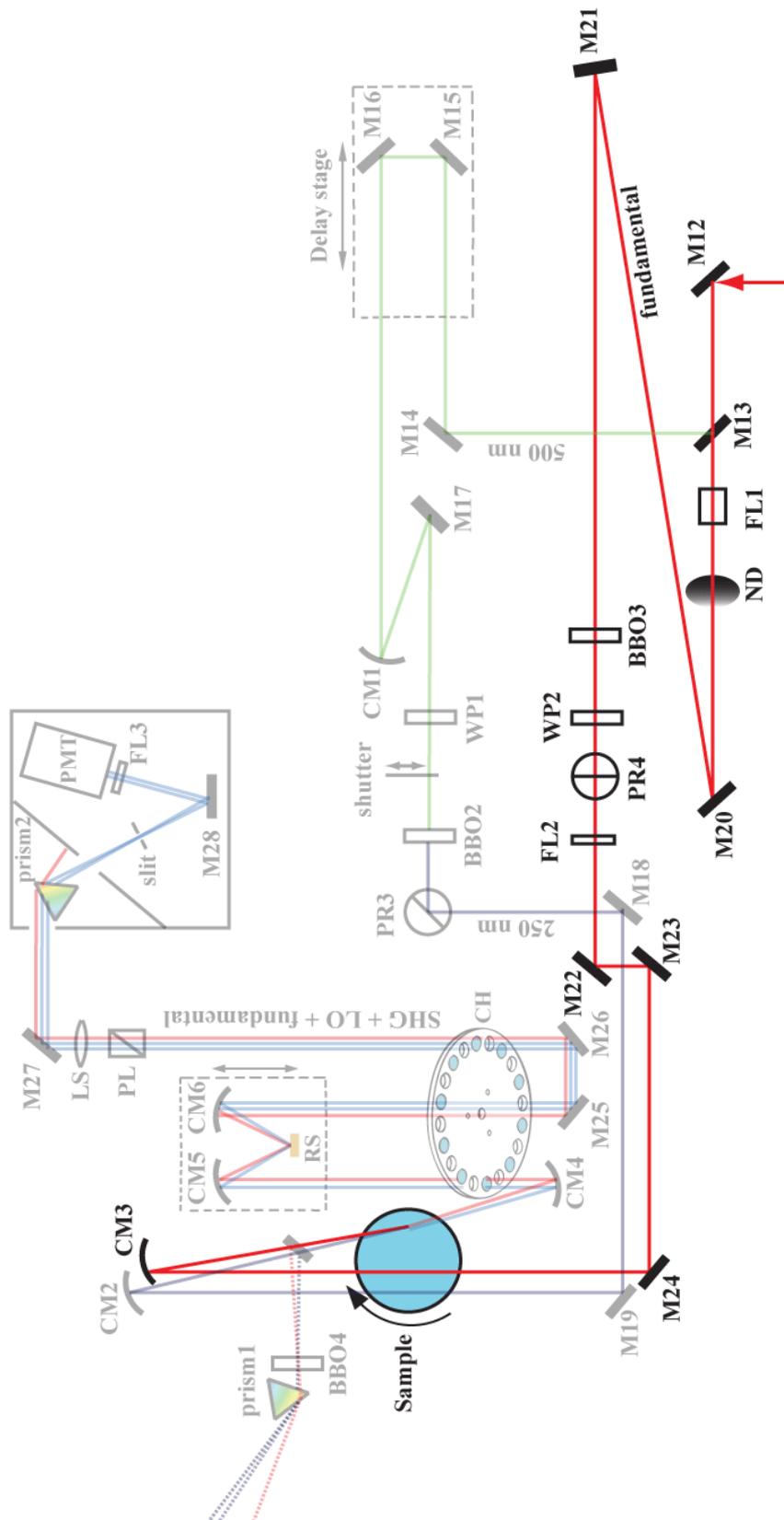
Figure 3.5. Scheme of the probe setup.

3.2.3   Spatial and temporal overlap

The pump-probe experiment requires for the pump and probe pulses to overlap in time and space at the sample surface. However, because both the pump and probe beams are tightly focused on the sample, this can be a challenging task. The probe beam needs to be focused for efficient SHG, which in general is not very efficient due to the quadratic dependence on the second-order term of polarization, and also due to the small distance over which frequency conversion occur (surface layer thickness). The pump beam needs to be focused to provide a sufficiently high concentration of electrons within the probed region.

Spatial overlap of the beams at the sample surface is obtained using a digital microscope (camera with magnifying lenses, 500X USB Digital Microscope Magnifier Endoscope Video Camera with 8LED TE050, XCSOURSE). For this procedure the liquid sample is replaced with a glass window, where the beams are easily visible on the surface. The window glass is positioned to match the height (vertical position) of the sample surface and the camera is placed above it. An example of an image provided by the microscope during the spatial overlapping of the beams is shown on Figure 3.6.
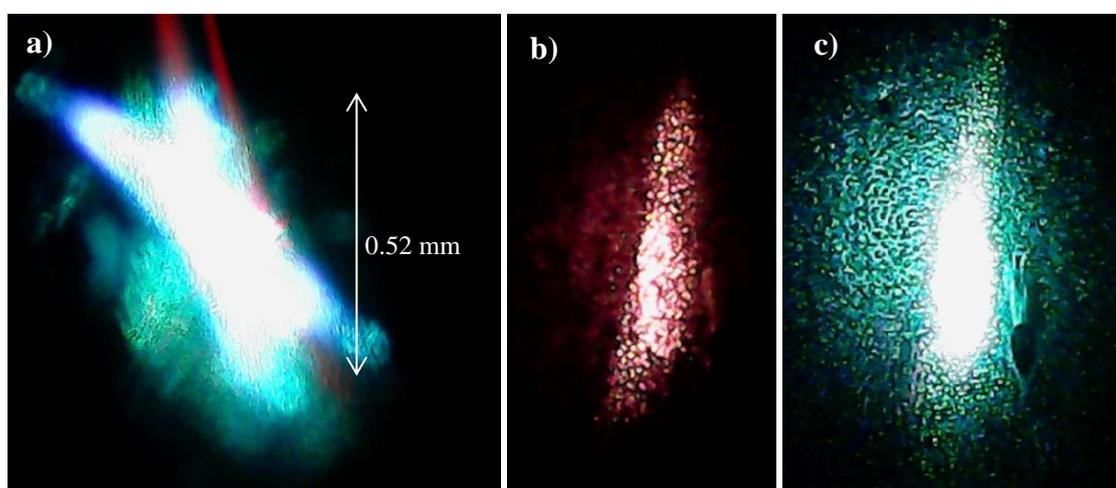
Figure 3.6. Image of a) spatially overlapping pump and probe beams, and b) probe and c) pump beams by their own on the surface of a glass window.

The timing of the pump and probe pulses is controlled by changing the distance through which the pump beam propagates, which is achieved with a motorized delay stage. In order to provide meaningful time resolved data, the delay between the pulses needs to be specified. For this purpose the delay time zero $t = 0$ between the pump and

probe pulses is obtained by mixing the pulses, using either sum or difference frequency generation, in the nonlinear crystal BBO4. This is shown on Figure 3.7. The beams are reflected from a mirror on a flip-mount, FM, located between curved mirrors CM2-CM3 and the sample, and are directed into the nonlinear crystal BBO4. The crystal is located at a distance from the FM where the beams overlap in space, which corresponds to the distance to the sample surface. After the crystal, the beams are spatially separated by a prism and the delay between the pulses is adjusted until the SFG or DFG signal is observed. The frequency mixing process occurs only when pulses are spatially and temporally overlapped in crystal, thus the observed mixed signal corresponds to $t = 0$.
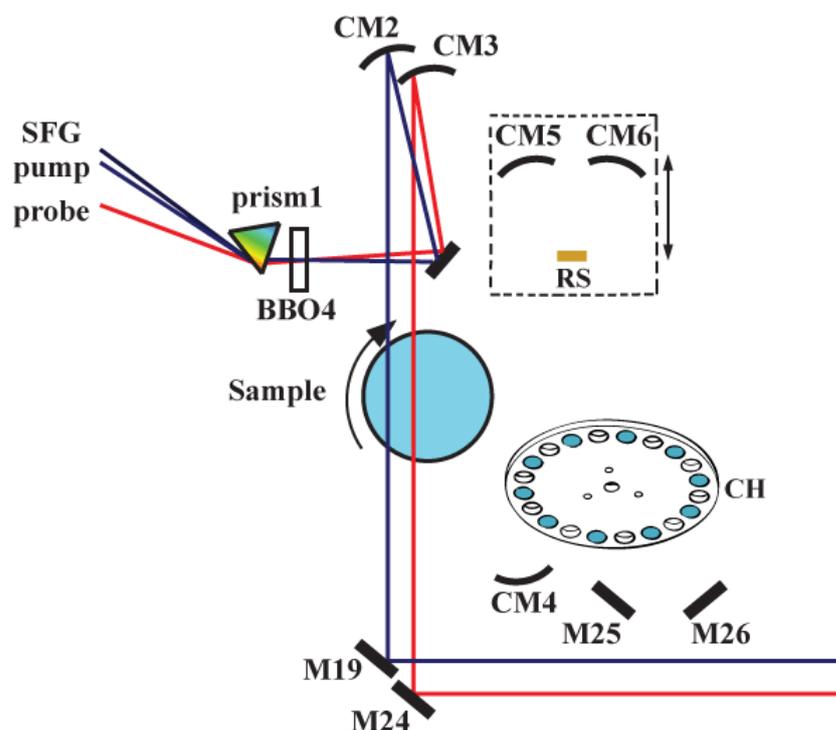
Figure 3.7. Part of the pump-probe setup presenting how the temporal overlap between pump and probe pulses is achieved by mixing of the pulses in nonlinear crystal BBO3.
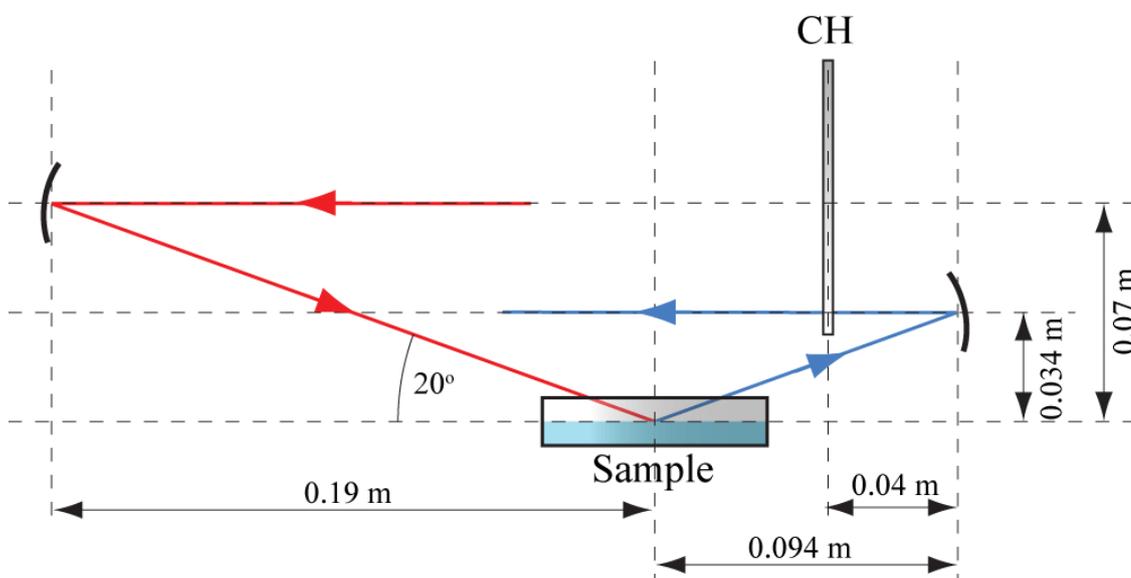
3.3   Sample setup

A liquid sample is placed in a glass dish which, in order to provide a constantly refreshed sample, rotates with an angular velocity of ~0.7 rad/s. The bottom of the dish

is black in order to prevent reflections from the glass, including from white light generated in solution, which can alter the detected signal. The rotating dish sits on a platform with sorbothane posts that eliminates vibrations. It is important for the sample surface to be positioned at a specific height, where pump and probe beams overlap and at which the SHG that is reflected from the surface reaches the detector. Due to the low efficiency of SHG from surfaces, the time-resolved measurement can take several hours, which has its consequences. For example, when studying liquid samples, evaporation with time changes the height and thus also the alignment. Therefore, the sample needs to be refilled in order to keep the same level. This is achieved monitoring the level of the sample surface using a simple laser pointer and a quadrant photodiode detector. A beam from the laser pointer (532 nm) reflects from the sample surface and is directed onto the detector, passing before through a lens in order to reduce fluctuations from the liquid sample. The detector is a quadrant photodiode, which gives an output signal in the form of a difference between the amount of light detected by the vertical diodes. This therefore provides a measure of the ideal height of the sample surface and sample can be added or removed to the desired level.

The probe beam reflected from the curved mirror CM3 impinges on the sample surface at an angle around $\vartheta_r \sim 70°$ from the surface normal. Equation (2.33) shows that the intensity of the SHG depends on the $\sec^2 \vartheta_r$, which means that it should be the strongest at 90° from the normal and becomes weaker as the angle goes to 0°. The probe beam is set to impinge the surface at the most shallow angle possible. Additionally, because the reflected fundamental light will be used to generate reference signal (local oscillator, LO) as discussed later, the angle of incidence should not be too close to the Brewster angle, which for water is around 53° at the used wavelengths.[168] Figure 3.8 shows the dimensions at which curved mirrors CM3 and CM4, sample and chopper wheel are kept relative to each other in order to provide the angle of incidence of the probe beam to be 70°. It also shows the smallest possible distance between the chopper wheel and mirror CM4, minimizing the distance between sample and reference surface L, in order to retain temporal overlap between SHG and LO pulses. The SHG reflected from the sample and the remaining fundamental probe beams enter the interference setup that is described later.

The pump beam impinges on the sample at an angle such that, after being reflected from the sample surface, it can easily be blocked while allowing the other beams to pass through. During the measurements, data was collected with the pump beam sharing the same plane of incidence as the probe beam, as well as with a ~3.5° difference between the pump and probe beams planes of incidence. The former is the preferred arrangement to simplify the symmetry of the excited sample system for reasons that will be described in the Results chapter.

Figure 3.8. Scheme of the relative distances and angles at which curved mirrors CM3-CM4, sample and chopper wheel are kept between each other.

3.4   Interference SHG setup

The SHG created at the sample surface propagates collinearly with the remaining fundamental beam and both enter the interference setup as shown in Figure 3.9. The basic idea of the phase-sensitive measurement follows one of the methods reviewed by Stolle *et al.* and described briefly earlier.[165] Second harmonic light generated at the sample propagates towards the reference surface RS, from which it is reflected. At the same time, the remaining fundamental light reflected from the sample surface is focused on the reference surface RS, producing the local oscillator SHG field, $\vec{E}_{LO}$. Because the beam paths for all the beams are identical, the spatial

overlap is preserved, causing $\vec{E}_{\text{SHG}}$ and $\vec{E}_{\text{LO}}$ fields to interfere. The measured interference signal can be expressed as

$$S^i = |\vec{E}_{\text{SHG}}|^2 + |\vec{E}_{\text{LO}}|^2 + 2f(L)|\vec{E}_{\text{SHG}}||\vec{E}_{\text{LO}}|\cos\left(\varphi + \frac{2\pi\omega\Delta n}{c}L\right) \qquad (3.1)$$

where φ is the phase between $\vec{E}_{\text{SHG}}$ and $\vec{E}_{\text{LO}}$ at the point they are generated and ω is the angular frequency of the second harmonic light. The phase can be controlled by virtue of the differing phase velocities of the driving field of the fundamental beam and the SHG fields in air (due to the difference in refractive index, Δn, at the two wavelengths). Hence, the phase can be conveniently controlled by altering the distance between the sample and the reference surfaces, L. If this distance is relatively small, then the group velocity mismatch is sufficiently small that both pulses remain temporally overlapped. Nevertheless, some attenuation will occur because of the group-velocity mismatch, which is included in equation (2.38) through the function $f(L)$.
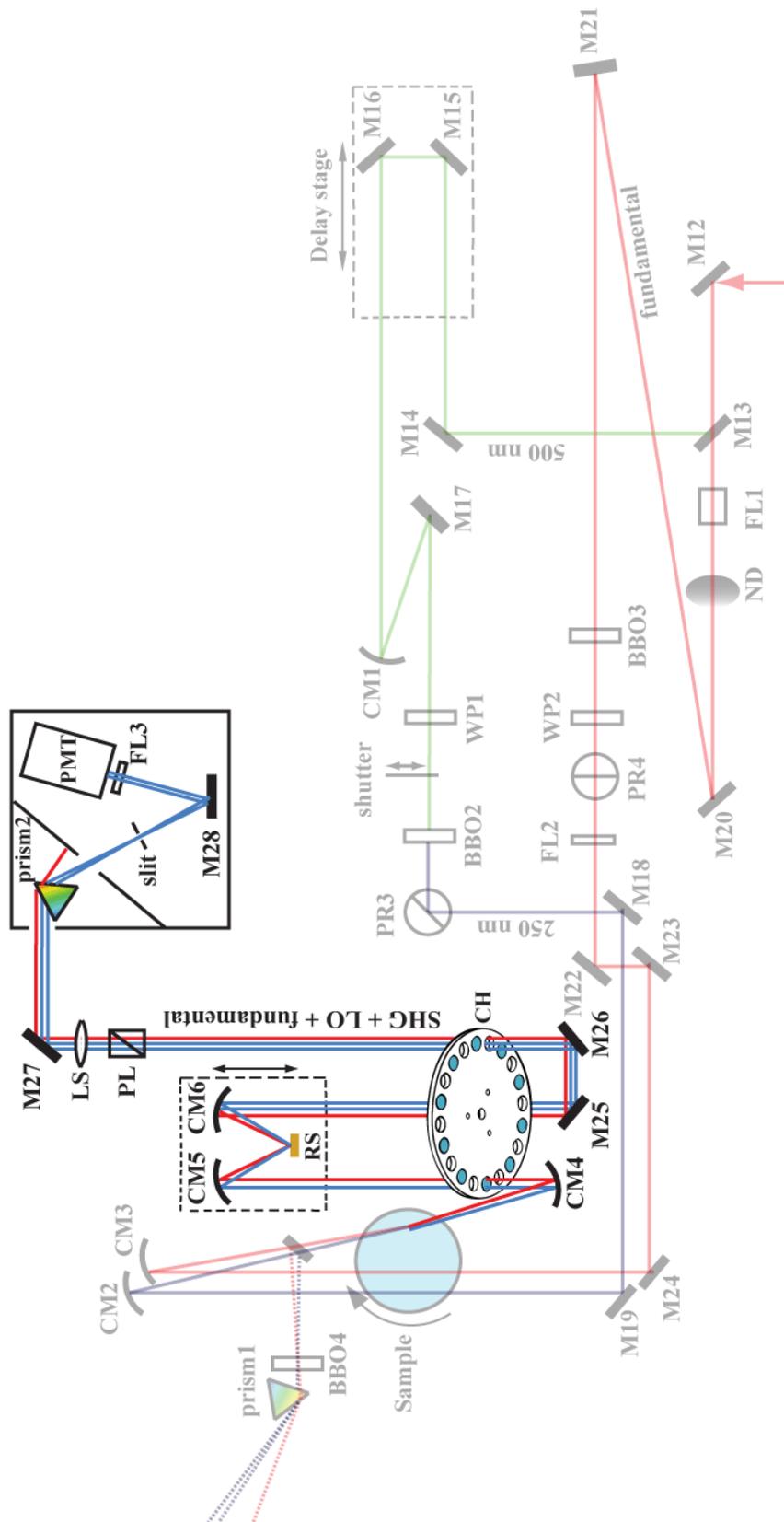
Figure 3.9. Scheme of the interference and detection setup.

Equation (3.1) consist of the quadratic terms from the sample SHG, $\vec{E}_{\mathrm{SHG}}{}^{2}$, and local oscillator, $\vec{E}_{\mathrm{LO}}{}^{2}$, and the interference term. As the last term is linear in $\vec{E}_{\mathrm{SHG}}$ and therefore also concentration, this is the term of interest here. To measure this term without the (large) constant offset imposed mostly by the $\vec{E}_{\mathrm{LO}}{}^{2}$ term (and $\vec{E}_{\mathrm{SHG}}{}^{2}$ in case of a strong SHG signal from the sample), a lock-in measurement is applied. The lock-in measurement employed here consists of two separate measurements. The first one occurs as described above (equation (3.1)), where $\vec{E}_{\mathrm{SHG}}$ and $\vec{E}_{\mathrm{LO}}$ temporally overlap and interfere. In a second measurement, the fundamental and $\vec{E}_{\mathrm{SHG}}$ beams are passed through a dispersive material which is placed between the sample and the reference surfaces. The result is that the group velocity mismatch between the harmonic and second harmonic is sufficiently large such that the two short pulses no longer temporally overlap. Hence, $\vec{E}_{\mathrm{LO}}$ will be generated before the $\vec{E}_{\mathrm{SHG}}$ pulse arrives at the reference surface and they can therefore not interfere. Such a measurement yields $S^{\mathrm{i}} = |\vec{E}_{\mathrm{SHG}}|^{2} + |\vec{E}_{\mathrm{LO}}|^{2}$. The difference between the two measurements provides the interference term of interest,

$$S^{\text{lock-in}} = 2f\left(L\right)\left|\vec{E}_{\mathrm{SHG}}\right|\left|\vec{E}_{\mathrm{LO}}\right|\cos\left(\varphi + \frac{2\pi\omega\Delta n}{c}L\right) \tag{3.2}$$

A simple scheme of the measurement is shown in Figure 3.10. The method works because of the integration over the entire pulse envelope in the frequency domain. If we attempted to record the spectrum by dispersing it onto a spectrometer, then the measurement yielding $S^{\mathrm{i}} = |\vec{E}_{\mathrm{SHG}}|^{2} + |\vec{E}_{\mathrm{LO}}|^{2}$ would be similar to the heterodyne detected methods described briefly before, and would show an interference pattern superimposed onto the spectral envelope.
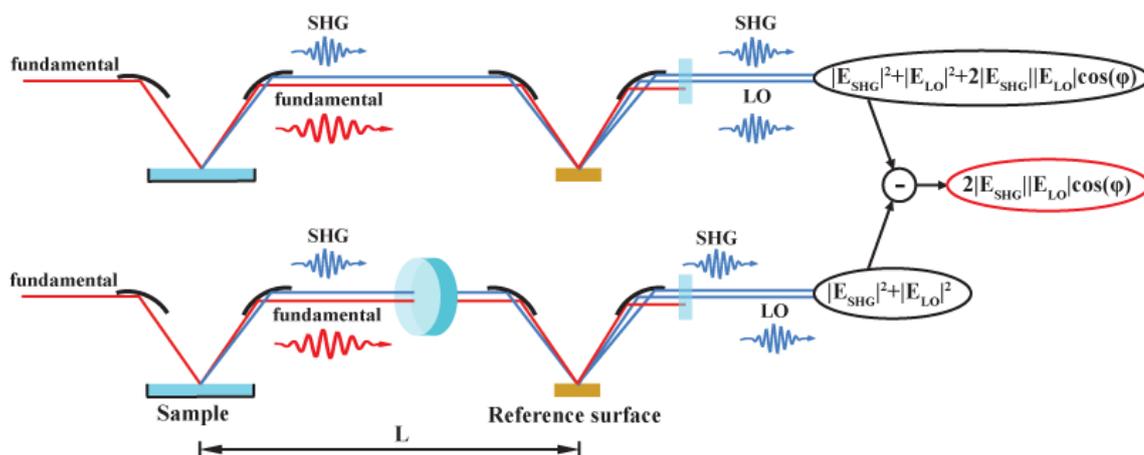
Figure 3.10. Schematic representation of the lock-in measurement. The top path shows the interference of a SHG field generated from the surface of interest with a LO from a reference surface. The bottom path shows the same, but the SHG and fundamental that will generate the LO are offset in time by the presence of a dispersive material leading to a group-velocity mismatch. In such a case, no interference takes place. The difference between the measurements recovers the interference term of interest.

In order to use this idea the setup, as shown in the Figure 3.9 was employed. The fundamental beam, together with the SHG beam generated at the sample surface, travel collinearly onto the curved mirror (CM4), which collimates the beams and directs them onto another curved mirror (CM5). The CM5 mirror focuses both beams on the reference surface, where the local oscillator beam is generated from the remaining fundamental beam.

As a reference surface, (110)-cut gallium arsenide ((110)-cut GaAs undoped crystal, MTI) was used. It provides a strong SHG signal due to its high second order susceptibility.[169] The reference surface is fixed to a rotatable mount, which provides control of the magnitude of the LO contributing to the interference signal (Figure 3.11). Rotation of the GaAs crystal changes the contribution of different $\chi^{(2)}$ tensor elements to the observed nonlinear response, which manifests in a change of the magnitude of the SHG. Table 3.1 presents the non-zero elements of the surface second order susceptibility tensor for the (110) face of GaAs, deduced by Stehlin *et al*., and the combination of polarization and sample orientation necessary to access them.[170]

Table 3.1. Non-zero $\chi_{surf}^{(2)}$ elements of the (110) face of the GaAs crystal and the corresponding experimental geometries used to obtain them determined by Stehlin *et al.*.[170]

$\chi_{surf}^{(2)}$ elements	Output polarization	Input polarization	Sample orientation (degree)
zzz	*p*	*p*	0[a]
zyy	*p*	*s*	0[b]
xxz=xzx	*s*	*p*	0[c]
yyz=yzy	*s*	*p*	36[c]
zxx	*p*	*s*	55[c]
yyy	*s*	*s*	0[b]
xxy=xyx	*s*	*p*	36[c]
yzz	*s*	*p*	36[c]
zzy=zyz	*p*	mix	#[d]
yxx	*p*	*p*	36[c]

Coordinate system is defined by *z* perpendicular to the surface and sample orientation 0° when *x* is lying in the plane of incidence.

sample orientation is determined by the input and output polarization.

[a] is accessible in combination with other $\chi_{surf}^{(2)}$ components, but it is much larger than the other components owing to the Fresnel factors.

[b] can be directly determined by the geometry given.

[c] is accessible only in combination with other $\chi_{surf}^{(2)}$ components.

[d] is mixed with bulk contribution.

The SHG produced from the (110)-cut GaAs, using 800 nm beam, as a function of the rotation around surface normal is presented in Figure 3.11 for the polarization combinations used during the experiments. The angle orientation of the reference surface is adjusted for experiments to provide relatively strong LO signal.
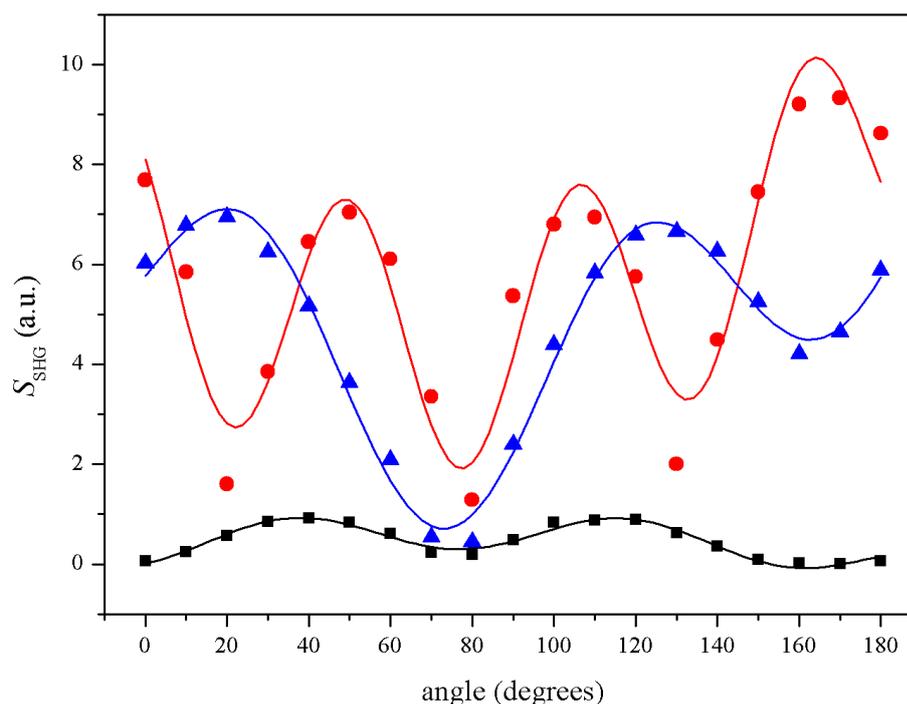
Figure 3.11. The change of SHG signal generated from the surface of (110)-cut GaAs with 800 nm beam for polarization combinations: PP (black squares), PS (red circles) and Smix (green triangles), with rotating GaAs around normal to the surface. The detected signal is a conventional SHG signal originating from the reference surface, SHG from sample was filtered before the RF for this measurement. Angles on the figure are arbitrary and do not relate to those in Table 3.1.

The second harmonic beam generated at the sample (SHG), the remaining fundamental beam and the second harmonic generated at the reference surface (LO) are collimated by curved mirror (CM6). These collinear beams are then directed into the detection setup.

As mentioned before, control of the phase in the experiment is achieved by changing the distance, L, over which SHG and fundamental beams travel together before generation of the LO at the reference surface. This is achieved by use of a manual translation stage on which reference surface and two focusing mirrors (CM5-CM6) are placed as shown on Figure 3.9.

In order to implement the lock-in measurement described on Figure 3.10 on a shot-to-shot basis, a rotating chopper (CH) is placed between the sample and reference surface. The custom chopper wheel (Figure 3.12) consist of 20 holes, where in every second hole a 2 mm thick glass window (SF10 for 1320 nm fundamental beam and CaF_2 for 800 nm fundamental) is placed in order to provide a delay between the SHG

from the sample and the fundamental pulses. However, as a consequence of this, in one of the lock-in measurements, the SHG from the sample experiences loss due to reflections from the window. This introduces an offset varying with SHG signal. To minimize this offset the beams are redirect to pass through the chopper once more after the generation of LO as shown on the Figure 3.9. The setup is aligned in such a way that for every shot, the SHG beam passes through the glass window once (i.e., if the window is present between the sample and reference surface, it is not present after the reference surface, and vice versa).
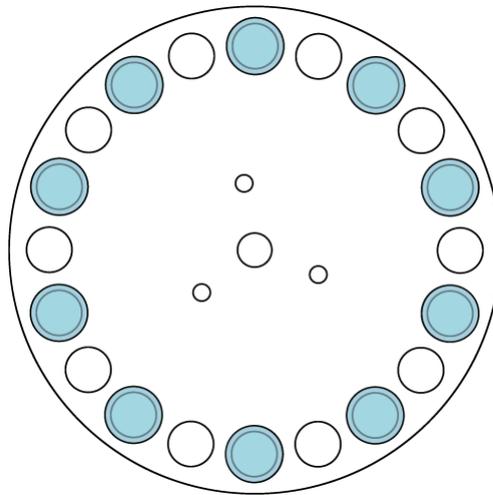
Figure 3.12. Custom chopper wheel made out of Teflon with a SF10 or CaF$_2$ glass window, for 1320 nm and 800 nm fundamental beam respectively, placed in every second hole. The technical drawing is shown in appendix B.

This arrangement ensures that the SHG from the sample always passes through a window, which in turn ensures that the $|\vec{E}_{\mathrm{SHG}}|^2$ term from equation (3.1) (which could vary with experimental conditions) is cancelled in the final lock-in measurement. However, a small constant offset remains, due to a difference in the reflection losses depending on whether the LO beam passes through the window or the fundamental beam that generates the LO passes through the glass window. However, this is relatively small.

With the chopper placed as described above, the lock-in measurement consist of two measurements, first one when the SHG and LO beams pass through the window after the reference surface, which can be described as:

$$S_1 = T_w(\omega)\left[|E_{SHG}|^2 + |E_{LO}|^2 + 2f(L)|E_{SHG}||E_{LO}|\cos\left(\varphi + \frac{2\pi\omega\Delta n}{c}L\right)\right]$$

$$= T_w(\omega)\left[C_1\left|\chi_{SHG}^{(2)}\right|^2 + C_2\left|\chi_{LO}^{(2)}\right|^2\right. \qquad\qquad (3.3)$$

$$\left. +2C_3 f(L)\left|\chi_{SHG}^{(2)}\right|\left|\chi_{LO}^{(2)}\right|\cos\left(\varphi + \frac{2\pi\omega\Delta n}{c}L\right)\right]|E_i(\omega/2)|^4$$

and the second one, when the SHG and the residual fundamental (used to produce LO) beams pass through the window between the sample and the reference surface:

$$S_2 = T_w(\omega)|E_{SHG}|^2 + |E_{LO}|^2$$

$$= \left(T_w(\omega)C_1\left|\chi_{SHG}^{(2)}\right|^2 + \left[T_w(\omega/2)\right]^2 C_2\left|\chi_{LO}^{(2)}\right|^2\right)|E_i(\omega/2)|^4 \qquad (3.4)$$

With that, the lock-in measurement, which is the difference between the both measurements ($S_1 - S_2$), is:

$$S^{lock-in}/\left|E_{in}(\omega/2)\right|^4 = C_2\left(T_w(\omega) - \left[T_w(\omega/2)\right]^2\right)\left|\chi_{LO}^{(2)}\right|^2$$

$$+2C_3 f(L)T_w(\omega)\left|\chi_{SHG}^{(2)}\right|\left|\chi_{LO}^{(2)}\right|\cos\left(\varphi + \frac{2\pi\omega\Delta n}{c}L\right) \qquad (3.5)$$

where the second term of the equation contains meaningful information about studied sample surface, while the first term is a constant offset mentioned before.

In the above equations (3.3)-(3.5) $E_{in}(\omega/2)$ is the electric field of the input beam at the fundamental frequency. $T(\omega)$ denotes the transmittance of the light at the indicated frequency through the window. From the Fresnel coefficients at the two surfaces of the window at normal incidence

$$T(\omega) = \left(\frac{4n}{(n+1)^2}\right)^2 \qquad\qquad (3.6)$$

where n is the refractive index of the window.

C_1 and C_3 contain the reflection losses of the SHG when it reflects from the reference surface. C_2 and C_3 contain the reflection loss of the fundamental beam at the sample, which then drives E_{LO}. Therefore

$$C_1 \propto |r_{RF}(\theta_{RF}, \omega)|^2 \qquad\qquad (3.7)$$

$$C_2 \propto |\, r_{\text{sample}} \left(\theta_{\text{sample}}, \omega/2 \right) |^4$$

$$C_3 \propto |\, r_{\text{RF}}(\theta_{\text{RF}}, \omega) \,||\, r_{\text{sample}} \left(\theta_{\text{sample}}, \omega/2 \right) |^2$$

where r_i is the polarization-dependent reflection Fresnel coefficient at i (sample or reference surface) and ϑ_i is the angle of the incidence at i (any phase shifts due to these reflections are neglected here).

The chopper wheel is controlled by a commercial controller (MC1000A, Optical Chopper System, Thorlabs) that can be phase locked to an external trigger. This is necessary so that it can be synchronized to the laser output frequency. The ideal laser frequency is 1 kHz, however, we found that the additional weight of the chopper wheel led to changes in the feedback circuitry that keeps the phase stability of the chopper. This meant that the chopper had to be operated at a reduced rate (close to 500 Hz).

Finally, we note that we have also explored the use of a reflective chopper wheel instead of the transmissive one described here, as this would avoid the offset completely. For this purpose, we designed a chopper wheel similar to the one shown in Figure 3.12 but entirely reflective, expect for the holes. The beam passing through the hole would then be redirected by the mirror located behind the chopper, thus achieving the phase difference. Unfortunately, it was not possible to achieve a sufficiently flat surface across the optic meaning that the beams were slightly divergent.

3.5   Detection setup

After the interference setup, the SHG, LO and residual fundamental beams are passed through a Glan-Taylor polarizer, placed on a rotation mount, where the output polarization of the SHG is selected (Figure 3.9). Subsequently, the beams pass through a lens, LS, which decreases the diameter of the beam travelling towards the detector. This helps to prevent any partial blockage of the beams, due to changes in sample height. After the lens, the beams are directed into the black box through an iris. Additionally, the lens is selected so that the beams are focused inside of the black box, and onto a slit. The width of the slit can be selected to avoid stray from reaching the detector. Inside the black box, the fundamental beam is separated from the SHG and LO

beams by a prism (Prism 2) and blocked. The SHG and LO beams are then directed into a photomultiplier tube detector (PMT, H7732-10 Photosensor Module, Hamamatsu Photonics) preceded by a bandpass filter FL3. The PMT detector sensitivity is controlled by adjustment of the voltage applied to it, which was kept at 700 V throughout the experiments presented. The signal detected by the PMT is passed across a 250 kΩ resistor to the data acquisition card DAQ (NI USB-6210, National Instrument), where the analog signal is converted into a digital signal and recorded on a computer. The 250 kΩ resistor is used to convert the PMT current pulse to a voltage and its value is chose to provide a time constant for the voltage decay that is slower than the DAQ rate but faster than the repetition rate of the experiment.

3.6 Experimental control and signal processing

After the experimental data has been received by the computer and before it is saved in an interpretable form, it is processed by a program created for this purpose. Also various different elements of the experiment, like the translation stage or shutter, are controlled from the computer. Functions and operations performed by a few different programs used in the investigation are described below. All of the programs were created using National Instruments LabVIEW 2011.

3.6.1 Monitor experiment

In order to be able to observe the lock-in signal described before, data obtained in the form of alternating pulses from two lock-in measurements (Figure 3.10) needs to be organized accordingly. For this purpose the 'Monitor experiment' program was created. This program by itself was used for alignment purposes and recording of the phase data. A simplified scheme of the operations performed by the program is showed in Figure 3.14.

It was found that the data forwarded by the DAQ card was being altered by harmonics of the 50 Hz mains noise, which interferes with the signal. To avoid this, the laser repetition rate is set to avoid interference with any harmonics of 50 Hz noise (475 Hz when laser operated at 950 Hz or 333 Hz when operating at 1 kHz).

Additionally, the 'Monitor experiment' program filters the signal from few mains harmonics, which result in substantial decrease in variation between the detected pulses. Such signal, which is the voltage generated across the resistor by the PMT, is then presented on a waveform graph.

Subsequently, the obtained signal is apportioned into cells containing separate laser pulses (Figure 3.13), which are defined as:

$$\frac{number\ of\ samples}{rate} = recording\ time$$

$$recording\ time \times laser\ frequency = number\ of\ laser\ shots \tag{3.8}$$

$$\frac{number\ of\ samples}{number\ of\ laser\ shots} = cell\ size$$

where *number of samples* specifies number of samples acquired by the program in a single data acquisition, each sample is a signal collected at finite time specified by 1/*rate*, *laser frequency* here is a laser repetition rate, and *number of laser shots* is number of laser shots recorded during a single data acquisition.

This can be presented by switching off 'show whole waveform' option on the waveform graph, which results in a graph showing all cells superimposed on each other. Data in each cell is then integrated within a range set by the user in the 'integration limits' control on the front panel.
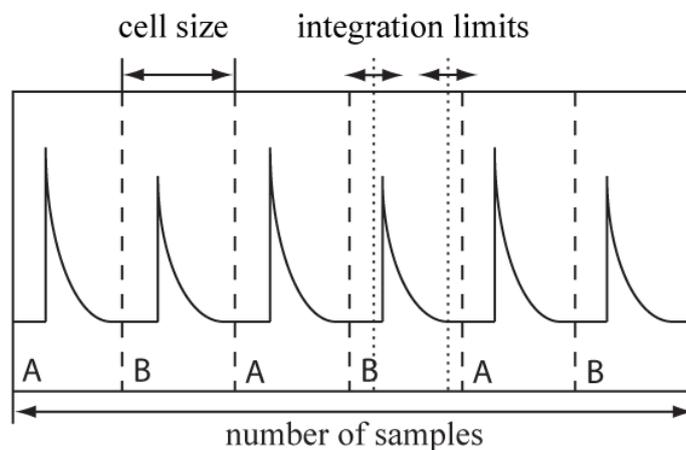
Figure 3.13. Illustration of how the obtained signal is portioned into cells and how the 'integration limits' is defined.

The integrated value of each cell is then arranged in a 1D array and sorted for A and B pulses, which correspond to the two measurements in the lock-in measurement. The A and B are then assigned to either the interfering or non-interfering parts of the lock-in measurement. Subsequently, an operation on A and B is performed. In this work, the operation of subtraction (A–B) was applied, however other actions such as 'A+B', '(A–B)/B', '(A/I_A^2)–(B/I_B^2)' can be performed, where last mode requires a photodiode to record the intensity of the laser that generates A (I_A) and B (I_B). Afterwards, the outliers from the mean value of the operation performed are removed. The outliers here are treated as the values deviating from the mean value by more than $n \times$ *standard deviation*, where n can be specified on the front panel ('standard deviation cut-off').
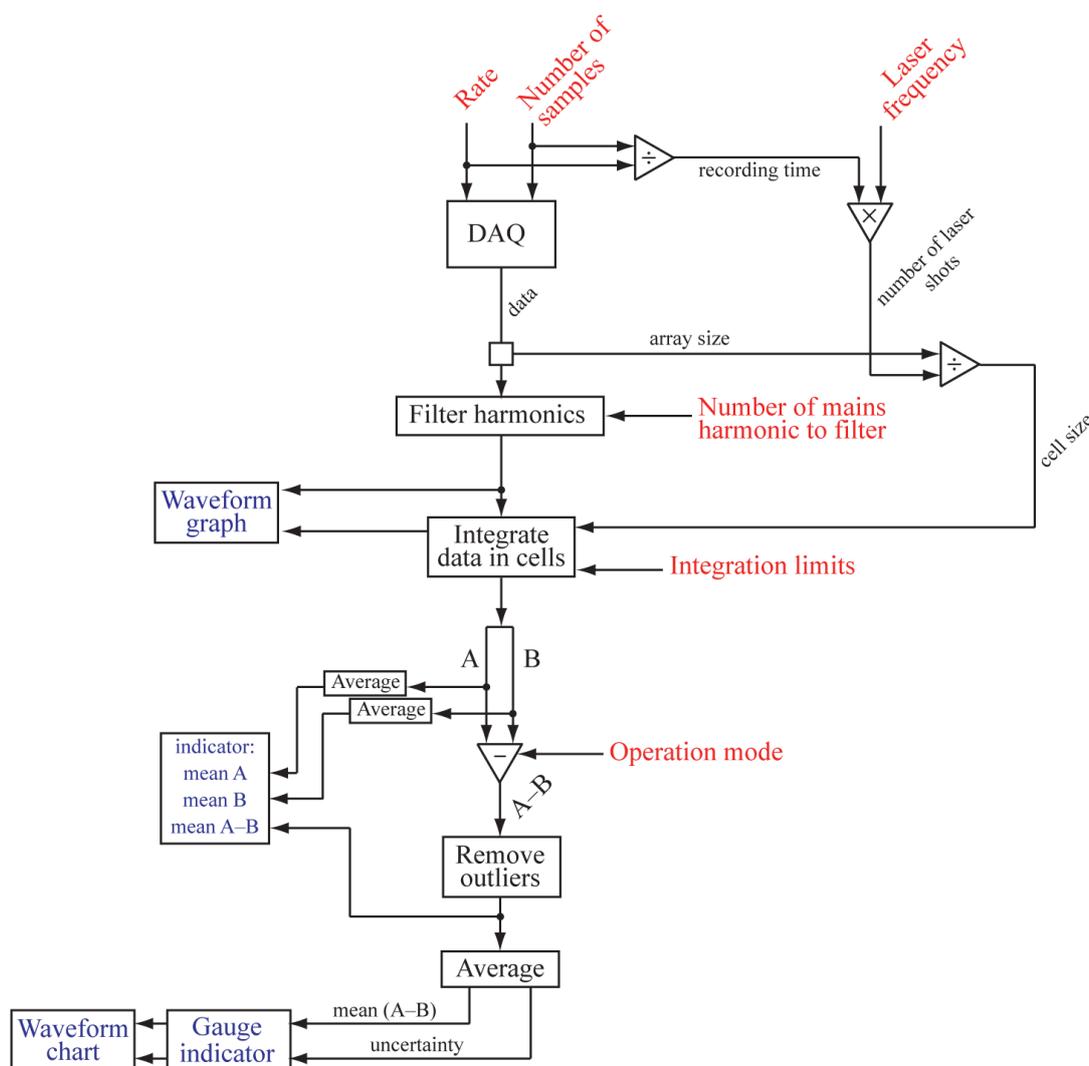
Figure 3.14. Scheme of the operations performed by program 'Monitor experiment' as described in text, with adjustable values showed in red and indicators showed in blue. Scheme is presented with operation mode 'A–B' as an example.

Around 5% of the values are treated as outliers for *2 × standard deviation* under normal experimental conditions. Once the outliers have been cleared, the results of the operation are then averaged and presented on the gauge indicator and waveform chart, with uncertainties specified as *standard deviation* / $\sqrt{array\, size}$. Additionally, the program displays the overall mean values of *A*, *B* and result of operation (e.g. '*A–B*') averaged over all the measurements taken, where one measurement here is a set of data detected from a single readout of the DAQ card (equation (3.8)).

3.6.2   Quadrant photodiode

Monitoring of the sample level, as described in 3.3, is controlled with the 'Quadrant photodiode' program. The program monitors the sample vertical level relative to the specified level, which has been chosen as an optimal level set during the alignment of the setup. The link to this program is placed in the 'Monitor experiment' and 'Time measurement' programs, so that an experimental run can be paused in order to check the sample level.

The quadrant photodiode has three outputs, which gives values corresponding to the difference between horizontal diodes, the difference between vertical diodes and the sum of all the diodes. The difference between the vertical diodes and the sum of all diodes are connected to the DAQ card and monitored using the LabView program.

The difference data is divided by the sum data, which then results in a value that varies between 1 and −1. A value of 1 indicates when one of the vertical photodiodes detects no light, and −1 when the other of the vertical diodes detects no light, while 0 indicates both vertical diodes detecting the same amount of light. The result of the division is then presented on a chart. The chart also presents a constant value ('marked height'), which can be set by user. This value is set by pressing the 'mark current height' button on the front panel, which sets the marked height value to equal the value detected at the moment of pressing the button. This value is also saved to a file, which is read and set as the marked height when the program is being launched (so that the target marked height is remembered). The marked height is usually set during the alignment of the setup, so that samples recorded later match the exact same height.
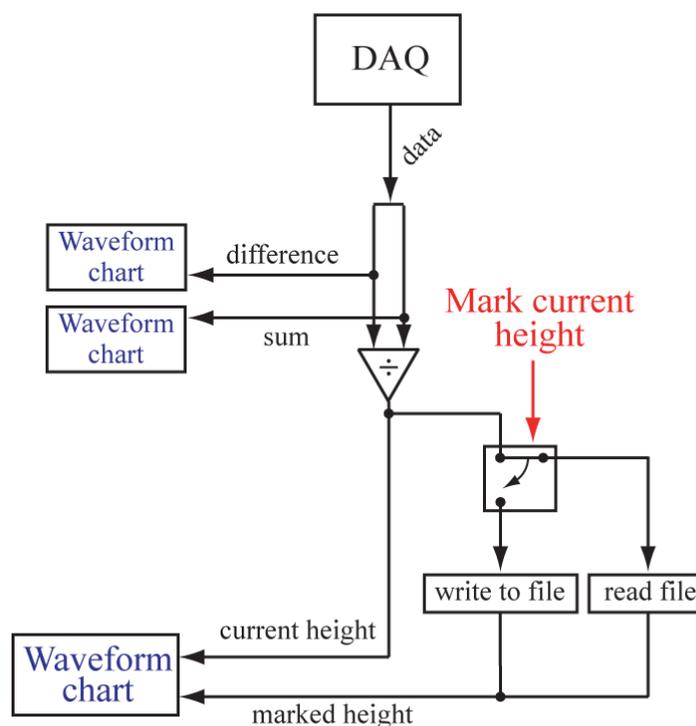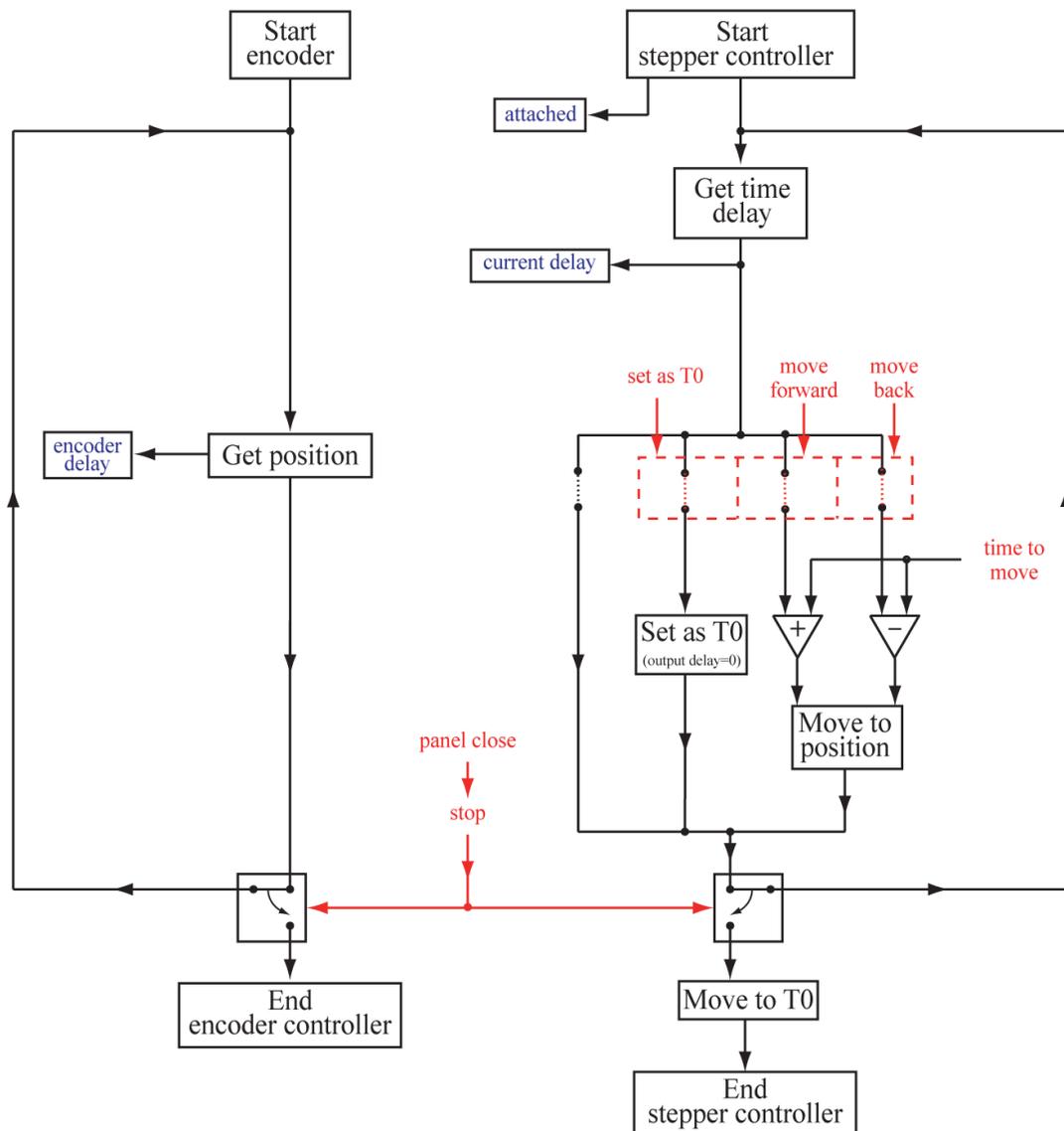
Figure 3.15. Scheme of the operations performed by the "Quadrant Photodiode" program as described in text, with indicators showed in blue.

3.6.3 Stage control

This program operates the delay stage placed in the pump beam setup. In the present experiment, a home build mechanical stage is used and was designed and constructed by Laurence Stanley. Movement is achieved using a leadscrew driven by a stepper motor (3302_0 - NEMA-17 Bipolar 48mm Stepper, Phidgets) with 0.9° step angle allowing changes in delay of ~3 fs. The stepper motor is controlled by a motor controller (1067_0 - PhidgetStepper Bipolar HC, Phidgets) operated from the computer. Additionally, in order to precisely determine position of the stage, a linear encoder (TONIC incremental encoder system with RSLM linear scale, Renishaw) is used. The sensor of the encoder is attached to the stage and during the movement scans over a fixed scale that determines the absolute position. The 'Stage control' program enables the operation of a stepper motor, moving the stage back and forward, and monitors the position of the stage, using the linear encoder. A simple scheme of the operations performed by the program is showed on Figure 3.16.

Initiation of the program engages the motor controller and sets current limit, acceleration and velocity limit of the motor (all these can be adjusted in the program). Proper initiation is indicated by a LED indicator on a front panel. Subsequently, a position, based on how many steps the motor has performed, is obtained and indicated as a current delay in femtoseconds. The delay is indicated with an offset so that zero ($t = 0$) refers to when the pump and probe beam pulses match each other in time at the sample, while negative and positive delay indicate pump pulse arriving after and before the probe pulse, respectively. At this point several actions can be performed by the program, however, if no action is perform the program keeps reading the current delay repeatedly. Pressing the 'move forward' control on the front panel (or the 'page down' button on the keyboard) causes addition 'time to move' control value to the current delay and the stage moves to that value. Pressing the move back control (or the 'page up' button on the keyboard) on the other hand subtracts the 'time to move' value from the current delay. "Set as T0" control sends the current position to the motor controller, where it is saved as the zero delay, and thus gives out value 0 as the current time delay. The 'stop' control causes the loop to stop, which then causes the stage to move to the 0 delay and stop the program after the 0 delay is achieved. The same action is performed if the program panel is closed without pressing the stop control beforehand. Additionally, in order to facilitate usage of the program keys F1 to F8 on the keyboard are assigned to enter values '100000', '50000', '10000', '5000', '1000', '500', '100' and '50' to the "time to move" control, respectively. The program also initiates the linear encoder, which reads the position according to the scale located below the stage. The delay according to the encoder is shown on the "encoder delay" indicator on the front panel. Pressing "Set as T0" control on the front panel works the same for the encoder as for the stepper controller and sets the current position as zero for it.

Figure 3.16. Scheme of the operations performed by program 'Stage control' as described in text, with controls showed in red and indicators showed in blue.

3.6.4   Time measurement

Collection of data for the time-resolved experiment is achieved using the "Time measurement" program, which is basically a combination of the "Monitor experiment" and "Stage control" programs. The program consist of two separate panels, the initiation panel which specifies all the parameters for the data collection, and the monitor panel which enables the monitoring of data during the measurement.

The function of the first panel is to provide the program with specification for the current experiment, which cannot be changed during data collection. The controls that can be specified in this panel are: rate, number of samples, standard deviation cut-off, number of harmonics to filter, integration limits, first pulse and operation mode, which are as specified for "Monitor experiment" in 3.6.1. The panel includes also controls which were not used in previously presented programs:

'Number in one step' control, specifies how many single acquisitions should be performed at each time delay. Single acquisition here is understood as the operations performed on data collected during *recording time* specified as in equation (3.8).

The 'do shutter measurement every' control specifies how often a measurement for the background (measurement with pump beam blocked by the shutter) is performed. Additionally, such a measurement is always taken at the first and last time step for the background. For example, if the time measurement were performed between 0 and 1000 fs in 10 steps with 'Do shutter measurement every' specified as 3, the measurement for the background would be taken at points 0, 300, 600, 900 and 1000 fs.

The panel contains also the section 'time points options', where delay points at which measurements are going to be taken are specified. The program allows this to be specified in three ways. 'Set spacing' mode requires values for starting and ending delay point, the number of steps and type of spacing (linear or logarithmic) between time delay points. With these an array with position points is created, which is then forward to the second panel. 'Set points' mode reads the values from an array, which is transferred to the second panel from either a one column table located in the front panel or from a file containing such table. Additionally, it can be selected whether the values are treated as specific delay points or step sizes between such points.

'Number of runs' defines how many times the full time measurement (data collected at all specified time steps) should be performed.

The 'name or relative path' control specifies name of the main folder in which all information from the performed experiment is to be stored. The name of the

folder that is actually created has the current date automatically added to the defined name.

After specifying all the conditions for the experiment in the initiation panel the data collection can be launched. Additionally, this disables all the controls in the initiation panel and opens the monitor panel.

There are three consecutive main actions performed by the program during the data collection. The first one moves the translation stage to the desired time delay. The second action records a dataset and is a data acquisition from the DAQ and its processing as was described for the 'monitor experiment' program. This is repeated as many times as it was specified by the 'number in one step' control. The third action of recording of the background, can take place, if requested. When the three main actions are finished, the background (function from the linear fit to the background) is subtracted from the recorded dataset removing any shift of the signal level due to evaporation of the sample. The cycle then repeats for the next time delay. When the data has been collected for all time delays, the program either stops or repeats all the actions described in this paragraph as many times as was specified in 'number of runs'. The data obtained is continuously presented on graphs and charts at specific stages of processing, as shown on Figure 3.17.

As a result the program saves data in text files as follows:

- "details" contains all parameters defined in the initiation panel.
- "raw/A" contains integrated data of the A cell for each acquisition from the dataset recording taken at each time delay.
- "raw/B" contains integrated data of the B cell for each acquisition from the dataset recording taken at each time delay.
- "raw/bg A" contains integrated data of the A cell for each acquisition from the background recording taken at each time delay.
- "raw/bg B" contains integrated data of the B cell for each acquisition from the background recording taken at each time delay.
- Main "separate" contains averaged data of the operation performed on the A and B cell during all acquisitions from the dataset recorded at one time delay, taken at each time delay presented with each run in separate column.

- Main "main" contains averaged runs from the main "separate".
- "Background/separate" contains averaged data of the operation performed on the A and B cell during all acquisitions from the background recorded at one time delay, taken at each time delay presented with each run in separate column.
- "Background/main" contains averaged runs from the background "separate".
- "Subtracted/separate" contains data obtained from background subtraction for each time delay separated for each run.
- "Subtracted/main" contains averaged runs from the subtracted "separate".
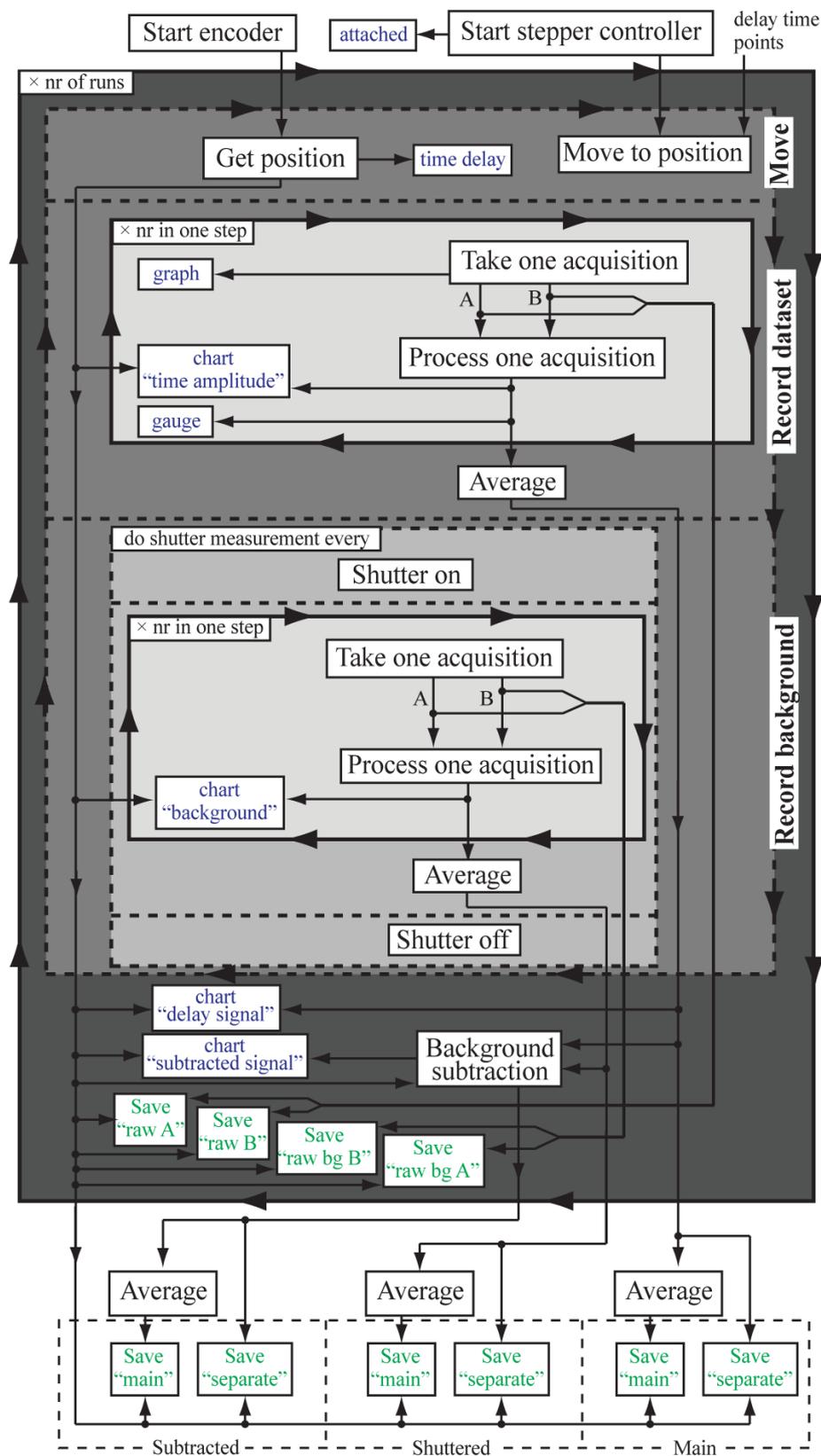
Figure 3.17. Scheme of the operations performed by program 'Time measurement' as described in the text, with indicators shown in blue and save operations showed in green.

3.7   Phase calibration

One of the advantages of the interference based SHG measurement is the ability to record the phase of the studied species. However, this phase is relative to the phase of the reference surface and, unless this is well characterized, it is not very insightful. To measure this, the sample is replaced with another surface of a known phase. This measurement provides the phase of the reference surface, and by comparing this with the measurement of the sample, the absolute phase of the studied species can be deduced. The absolute phase then represents the phase shift of the generated SHG light as compared to the incident light.

For such calibration measurement, a quartz crystal is used here. The SHG signal generated from quartz, due to the lack of absorption in the used fundamental or its second harmonic wavelength ranges, contains only the nonresonant (real) part in equation 2.36.[171, 172] However, because the SHG arises mainly from bulk contributions, an additional factor of i must be added, which shifts the phase by $\pi/2$ and thus appears as an imaginary (resonant) surface signal would.[127]
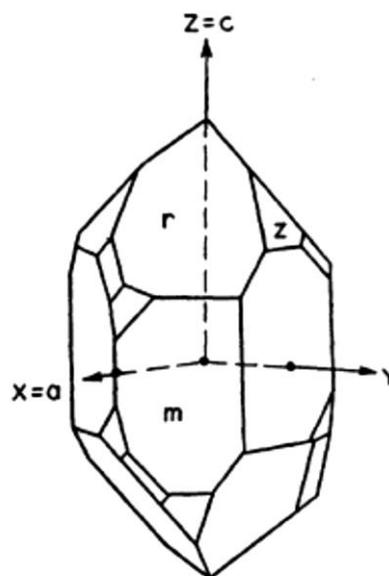
Figure 3.18. Left-handed quartz crystal.[173]

Quartz is a trigonal crystal with 32 (D$_3$) symmetry, with sixfold rotational symmetry around the c axis of the crystal, which gives three equivalent secondary axes, a_1, a_2, a_3, separated by 120° from each other in the plane normal to c. According to

established convention, the *z* axis is defined as parallel to the *c* axis of the quartz, *x* axis is parallel to any of the *a* quartz axes, and *y* is perpendicular to *z* and *x* axes.[173] Due to its symmetry, the quartz crystal has four independent $\chi^{(2)}$ tensor elements: $\chi^{(2)}_{xxx} = -\chi^{(2)}_{xyy} = -\chi^{(2)}_{yyx} = -\chi^{(2)}_{yxy}$, $\chi^{(2)}_{xyz} = -\chi^{(2)}_{yxz}$, $\chi^{(2)}_{xzy} = -\chi^{(2)}_{yzx}$, $\chi^{(2)}_{zxy} = -\chi^{(2)}_{zyx}$.[106] The $\chi^{(2)}$ response from the quartz is dominated by $\chi^{(2)}_{xxx}$ tensor element, which is real and positive for left-handed quartz.[172]

The quartz used here was left-handed (Figure 3.18) *z*-cut (*z* axis of the crystal perpendicular to the surface plane) quartz. The positive *x* axis (one of the *a* quartz axes) of quartz crystal was defined using the piezo-electric effect, and determined by measuring the sign of the brief potential generated when a force is applied to the crystal, as shown on Figure 3.19. For left-handed quartz a positive charge accumulates at positive end of *x* axis when tensile stress is applied along the *x* axis.[173]

Figure 3.19. Determination of the *a* axes of quartz crystal using piezo-electric effect.

In order to perform a calibration measurement, the quartz crystal is positioned in place of the sample and oriented with the positive end of the *x* axis along the direction of the probe beam propagation in the plane of propagation, as shown on Figure **3.20**. Therefore, the polarization combinations used in the experiment will align to the

corresponding $\chi^{(2)}$ elements: $\chi_{xxx}^{(2)}$ for PP, $-\chi_{xyy}^{(2)}$ for PS, and $-\chi_{yyx}^{(2)} = -\chi_{yxy}^{(2)}$ for Smix. Figure 3.21 shows phase measurements performed for quartz positioned as described here for PP, PS and Smix polarization combinations with an arbitrarily chosen GaAs orientation.
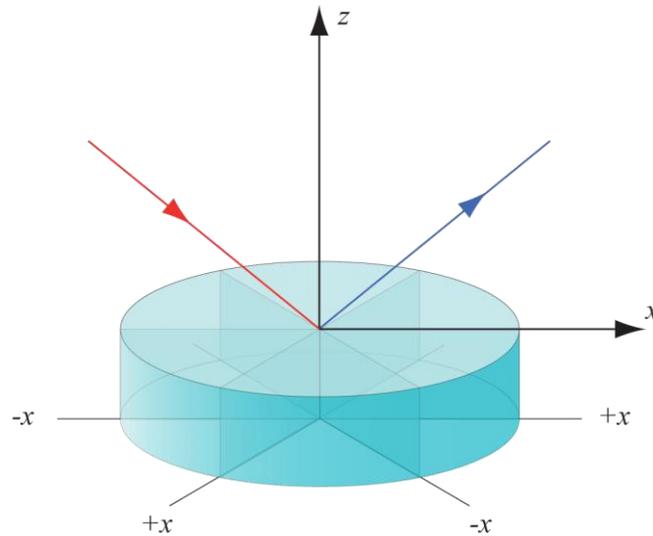
Figure 3.20. Schematic illustration showing the orientation of the quartz during the calibration measurement. The positive end of the *x* axis of the quartz crystal is oriented along the propagation of the probe beam.
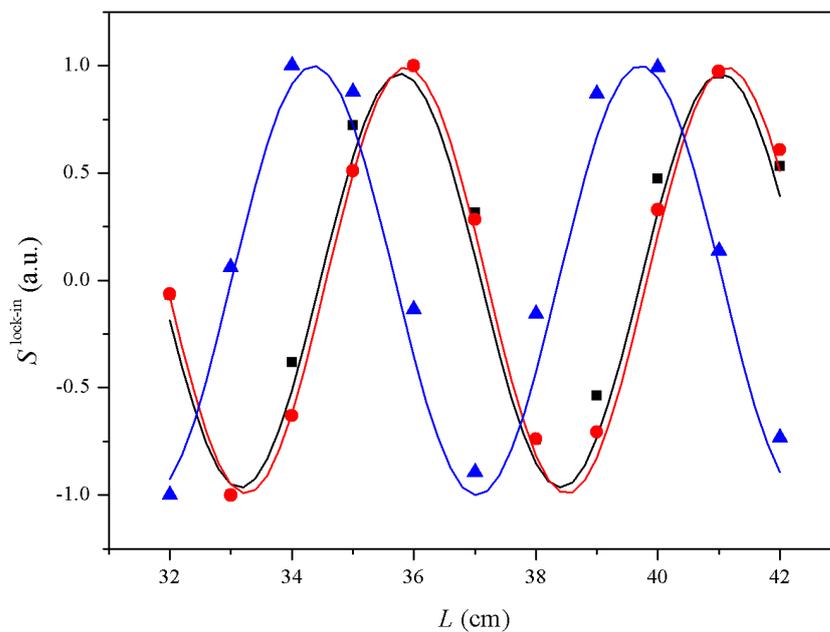
Figure 3.21. Phase measurements taken with quartz oriented as shown of Figure 3.20, and an arbitrarily chosen orientation of GaAs crystal. Symbols and lines represents normalized measured data points and fitted to it sine functions, respectively. Black (squares) for PP, red (circles) for PS, and blue (triangles) for Smix polarization combinations.

3.8   Malachite Green

In order to demonstrate the methodology and the setup described, a series of measurements were performed on malachite green (MG) at the water/air interface. Malachite green has been the subject of many investigations, including time-resolved SHG. It therefore serves as an ideal comparator. Moreover, it has readily accessible optical transitions peaking at around 610 nm for $S_1 \leftarrow S_0$ and 400 nm for $S_2 \leftarrow S_0$ (Figure 3.22), which can provide a strong SHG signal by a resonant enhancement.[174-179]
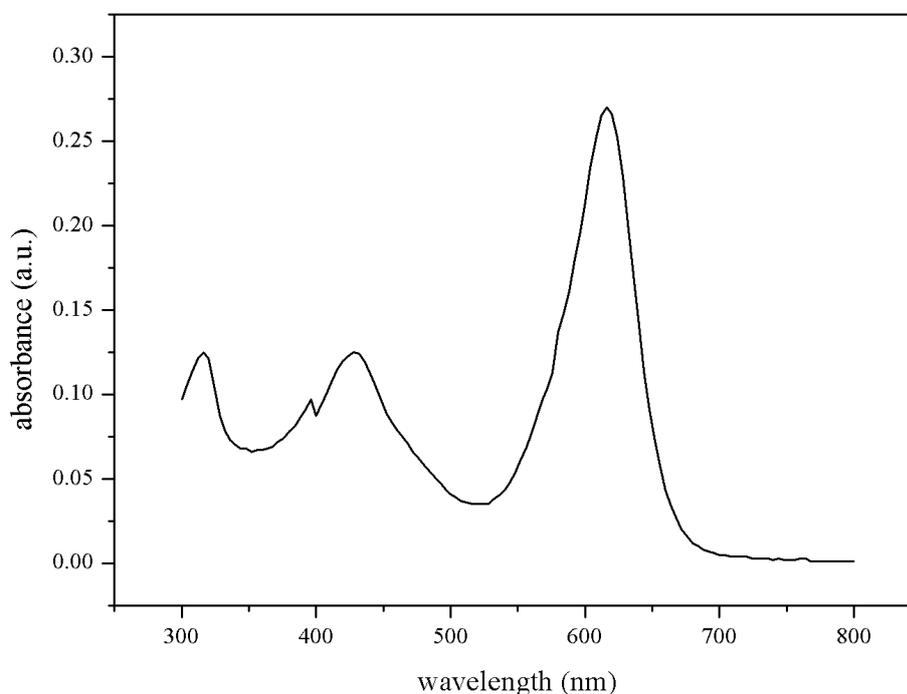
Figure 3.22. Absorption spectrum of MG solution in water.

Malachite green is a triphenylmethane dye, which exhibits a strong green colour due to the absorptions mentioned. Relaxation to the ground state of MG after the photoexcitation to the S_1 and S_2 excited states occurs mainly by a nonradiative decay. Relaxation from the S_1 state involves rotation of the phenyl groups about the central carbon atom (Figure 3.23), which leads to conical intersections with the S_0 state through which it decays to the ground state. Similarly, relaxation from the S_2 state involves motion of the phenyl rings. The molecule relaxes via a conical intersection between S_2 and S_1 state, and proceeds to the ground state through the S_1 state as described before.

This relaxation process occurs on a picoseconds timescale and, because of the nature of the dynamics, is strongly dependent on the viscosity of the solvent.[180-183]
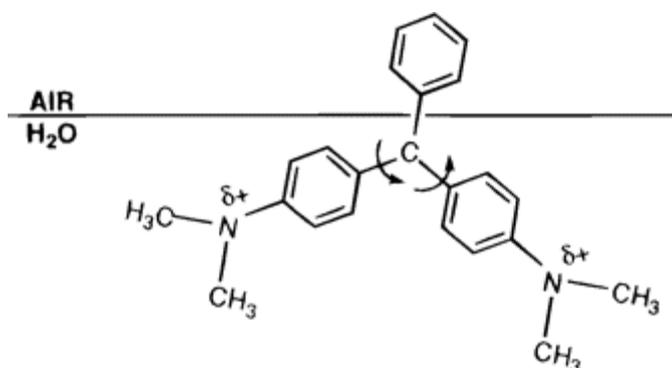

Figure 3.23. Schematic of orientation and isomerizing motions of MG at water/air interface.[176]

For the experiments presented here, a 10 μM solution of malachite green (Malachite Green Carbinol Hydrochloride, Sigma-Aldrich) in water from a filtration unit (Millipore Milli-Q Gradient A10, 18.2 MΩ cm, TOC< 4 ppb) was used. As a probe beam, either 800 nm light from the amplifier directly or 1220 nm output from OPA (obtained in the same way as showed on Figure 3.1 for 1320 nm) was used. The pump beam at 400 nm was provided by SHG in a BBO crystal from the fundamental 800 nm beam. These beams match the transitions of MG: the second harmonic of 1220 nm matches the $S_1 \leftarrow S_0$ transition, while second harmonic of 800 nm matches the $S_2 \leftarrow S_0$ transition. The laser repetition rate was 333 Hz. All data presented here for MG were collected for PP polarization combination.

Phase

In order to determine the phase of the measurements, the lock-in signal as a function of the distance between sample and reference surface, $S^{lock-in}(L)$, was measured. The results of this using both 1220 nm and 800 nm probe beams for MG, water and quartz are presented in Figure 3.24. Note that no pump beam was present in these phase measurements. Also shown in Figure 3.24 is the expected (calculated) signal based on the relative phase-velocity difference between fundamental beams and their second harmonics in air (assuming ∼30 fs FWHM Gaussian transform-limited pulses). Visible in Figure 3.24 are oscillations in signal, which arise from the SHG and LO pulses being in phase (constructive interference) and out of phase (destructive interference), while

the envelope arises from the group-velocity mismatch. Due to a bigger difference in refractive index between 800 and 400 nm in air, the oscillation frequency and damping are faster for it than for 1220 and 610 nm. The measured response over the range $0.2 < L < 0.4$ m reproduces the behaviour of the calculated interference pattern.
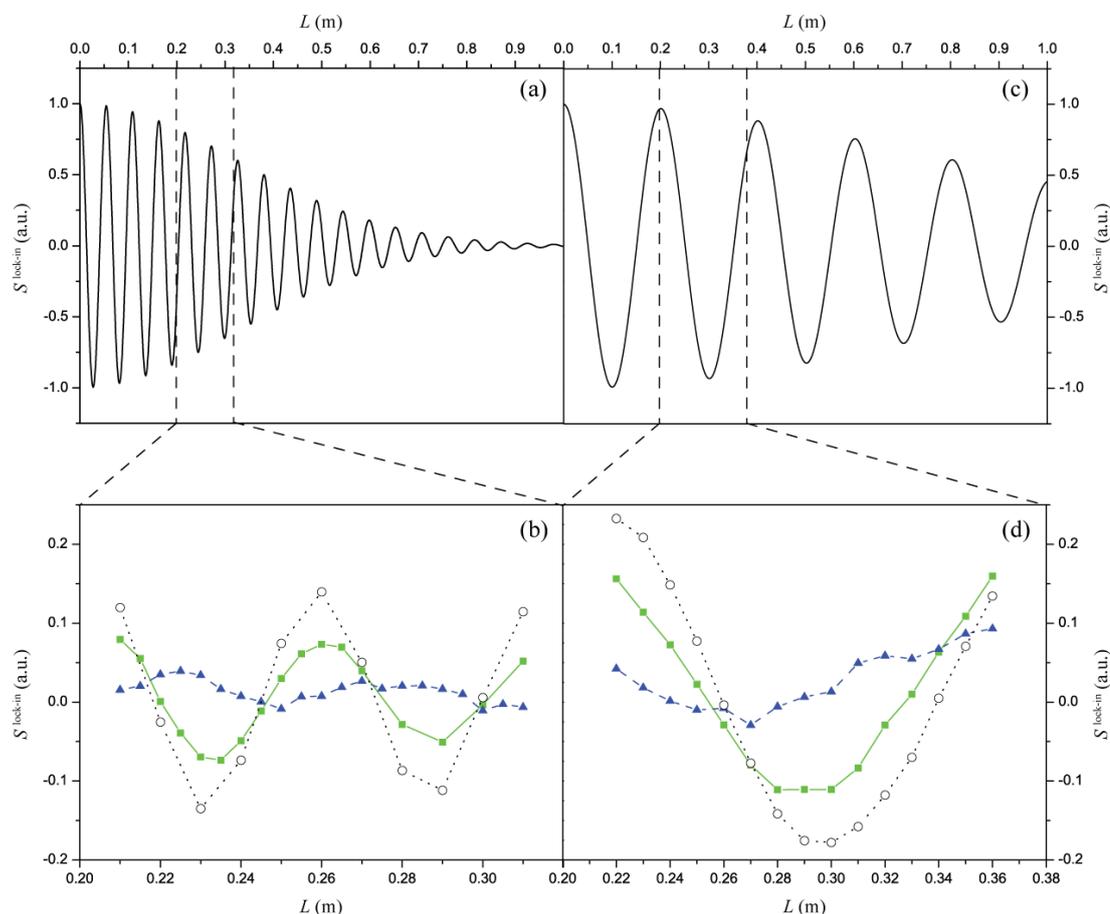
Figure 3.24. Dependence of interference signal on distance between sample and reference surface L. (a) Calculated signal and (b) measured signal with an 800 nm probe beam; (c) calculated signal; and (d) measured signal for a 1220 nm probe beam. The green squares represent signal obtained with malachite green as a sample, blue triangles represent water signal (magnified 10 times for (b) and 5 times for (d)) and open circles represent quartz.

Comparison of the signal obtained for MG and quartz shows close similarity in phases. As mentioned before, the beams used in the experiment are far from any resonances in quartz and so the signal originating from it is real. However, due to the bulk origin of the SHG from quartz its phase appears as it would for imaginary signal (shifted by $\pi/2$). Therefore, the match between MG and quartz suggests that the SHG signal from MG is mostly imaginary at the probed wavelengths. This is in line with the fact that the second harmonics of the used probes are in resonance with transitions of

MG. Additionally, this is further confirmed by comparison with the signal obtained for water. Similar to the case of quartz, the probe wavelengths are far from any water resonances resulting in the SHG signal being dominated by a nonresonant (real) response. However, as the signal from water originates from the surface, its phase should appear $\pi/2$ shifted from the resonant signal from quartz and MG, which can be seen on the graph. Additionally, it is worth noting that the signal obtained for water, where no resonant enhancement takes place, is much weaker than for MG (magnified 10-fold and 5-fold in Figure 3.24 for 800 and 1220 nm, respectively).

Linearity

The linearity of the technique as a function of interfacial concentration can be demonstrated using a pump-probe experiment. The strong signal for MG measured at 1220 nm probe arises from the resonance of the second harmonic with the $S_1 \leftarrow S_0$ transition of MG. If linear, the signal is therefore proportional to the number of MG molecules in S_0. By applying a pump pulse at 400 nm beforehand, which drives the $S_2 \leftarrow S_0$ transition, some of the population from S_0 will be removed, so that the measured signal from the probe will be depleted. By linearly varying the pump power, the interfacial concentration of MG in S_0 will also be varied linearly. The delay between pump and probe was set to 300 fs, and the subsequent interference signal was measured while varying the pump power by rotating a half wave plate placed before the BBO crystal that produces the 400 nm. The maximum pump energy (~ 1 µJ pulse^{-1}) was kept sufficiently low to ensure that no saturation effects were introduced as this would lead to a non-linearity of the concentration as a function of pump pulse energy. The results shown on Figure 3.25 confirm the linear dependence of the interference signal as a function of concertation. Additionally, to visualize what is measured here, the right panel of Figure 3.25 shows the difference in signal as a function of phase when the pump is present and absent.
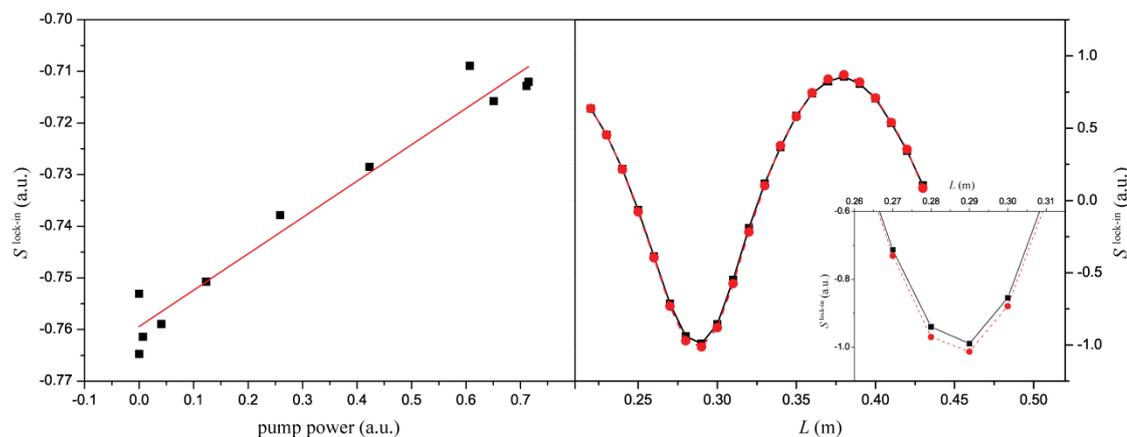
Figure 3.25. Left: Interference signal obtained with the varied pump power, taken at the distance between the surfaces $L = 0.29$ m, with the red line indicating linear fit. Right: The interference signal, with varying distance L, in absence of pump beam (red circles) and with a pump beam at maximum power (black squares), with a magnification of the destructive interference peak in the inset.

Time-resolved pump-probe experiment
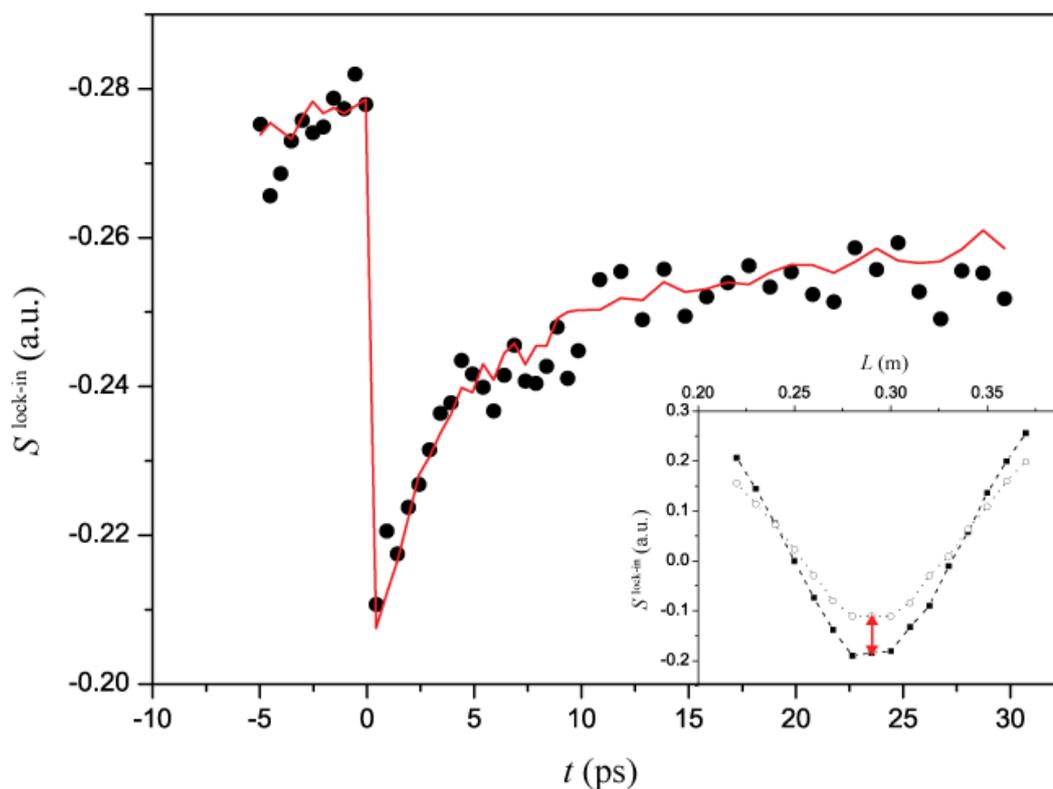
Figure 3.26. Time resolved recovery of the ground state MG. The red solid line shows an average of 10 measurements, while the dots show a single measurement. The inset presents an interference signal obtained in the presence (empty circles and dotted line) and absence (filled squares and dashed line) of the pump beam with varying distance L, with arrow showing the position at which the time resolved measurement was taken

As the above results indicate that the interference based signal is linear with the concentration, time-resolved pump-probe measurement can be considered linear as well. With that, the dynamics of the recovery of MG molecule to its ground state after the excitation to the S_2 state were measured (Figure 3.26). MG was excited with a 400 nm pump pulse (23 μJ pulse^{-1}) and probed at variable time delays using a 1220 nm probe pulse (50 μJ pulse^{-1}). The distance L between sample and reference surface was set so that the SHG and LO were in destructive interference, as is shown on the inset of Figure 3.26.

Immediately after excitation, the ground state is bleached as shown by a decrease in signal at zero delay between pump and probe pulses. The signal recovers to an offset in ~20 ps, which then decays further on a much longer time-scale. The data points in Figure 3.26 represent a single measurement where each point is an average of 3300 pulses (10 s). Hence, the entire trace could be measured in < 10 min. The solid line in Figure 3.26 is the average of 10 successive measurements (~1 h), demonstrating the ability in acquiring high quality data in a relatively quick time. Comparing these data with that measured by Sen *et al.* using the conventional SHG (proportional to $|\chi^{(2)}|^2$) reveals very similar dynamics and timescales when the square-root of their raw data is considered (Figure 3.27).[175] Additionally, in terms of signal to noise, a single run data-set from the measurement presented here (which contains about twice as many data points over the first 30 ps) is of comparable quality as that presented by Sen *et al.*.
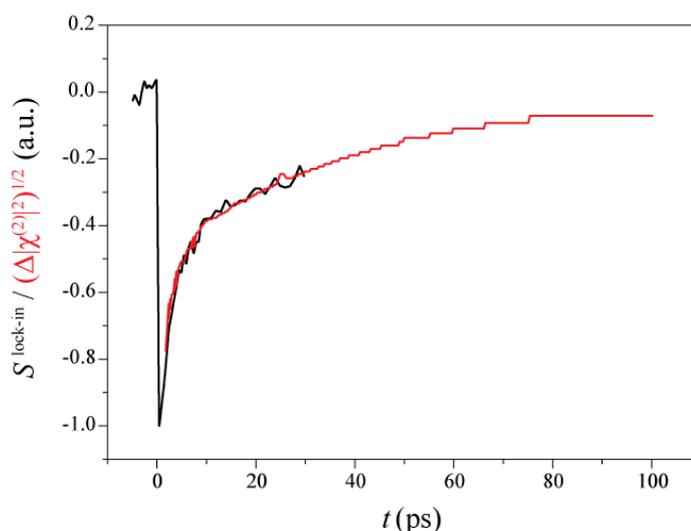
Figure 3.27. Normalized data from Figure 3.26 (black) compared to the square-root of data for 5 μM MG obtained by Sen *et al.*(red).[175]

In the measurement like the one presented on Figure 3.26, where the time-resolved data is obtained only at one phase point, the resulting signal can be a consequence of either change in the concentration or change in the absorption spectrum. Because the lock-in measurement is based on two points (with and without interference) it does not distinguish between a decreasing amplitude of the interference pattern (change in surface concentration) and a phase shift with a constant amplitude (change in absorption spectrum). Figure 3.28 presents this graphically on a hypothetical phase measurements. To clarify the ambiguity, either the interference pattern (as in Figure 3.24 and Figure 3.25) can be recorded at a few select pump-probe delays, or the dynamics at a number of different phase differences between 0 and π can be measured. For the data presented here on MG, there was only a change in amplitude (inset of Figure 3.26) and no significant phase shift was observed.
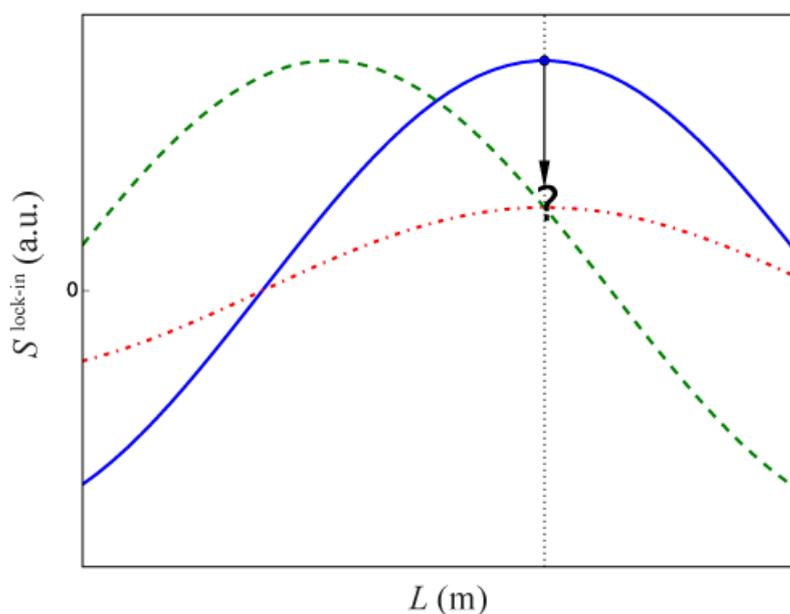
Figure 3.28. An illustration of the ambiguity inherent in taking a measurement at a single stage position (marked as the vertical black dotted line). It is unclear if the change in signal of a measurement (blue solid line) is due to a change in intensity (red dots and dashes) or a change in phase (green dashes).

4 Results

The experimental lock-in method as described in the previous chapter, providing time-resolved and phase-sensitive information about interfacial species, was used with the intention to observe the hydrated electron. Particular attention was devoted to the early time behaviour of the electron solvation, however, other results are also shown. Unless stated otherwise, in the presented experiments the electron was produced via excitation of the CTTS state of iodide ion. As it was noted in the first chapter, iodide exhibit enhanced concentration at the water/air interface. As excitation of the lowest CTTS band produces an electron in close proximity to the parent ion, the ejected electron has a high probability of being located at the interface. A 2M NaI (ACS grade, $\geq$99.5% purity, Alfa Aesar) solution in water from a Millipore filtration unit (Millipore Milli-Q Gradient A10, 18.2 MΩ cm, TOC< 4 ppb) was used unless stated otherwise. Experiments were performed using 250 nm pump and either 1320 nm or 800 nm fundamental probe beam. The pump is resonant with the lowest CTTS band of iodide.

4.1 Dynamics with a 1320 nm probe

The second harmonic of the 1320 nm probe at 660 nm is mostly resonant with the p $\leftarrow$ s transition of the hydrated electron, which has its maximum at 720 nm (Figure 1.13). However, the fundamental of the probe itself can be resonant as well. Iodide irradiated with light of energy above ~4.9 eV excites its lowest CTTS state. From this, the electron is detached in ~ 200 fs forming a close contact pair with the iodine atom. Iglev *et al*., using transient absorption in a range between 400 to 1100 nm, measured the kinetics following excitation of the iodide at 242 nm (5.1 eV).[184] They found a broad absorption in the near-infrared with a maximum at ~1000 nm (1.24 eV), which decayed with time constant of 220 fs. They assign this absorption to the transition of the transient CTTS state to the higher-lying CTTS states, and the decay of this signal to the escape of the electron from the parent solvent cavity. Figure 4.1 shows the absorption spectra of the different intermediate states, as assigned by Iglev *et al*..
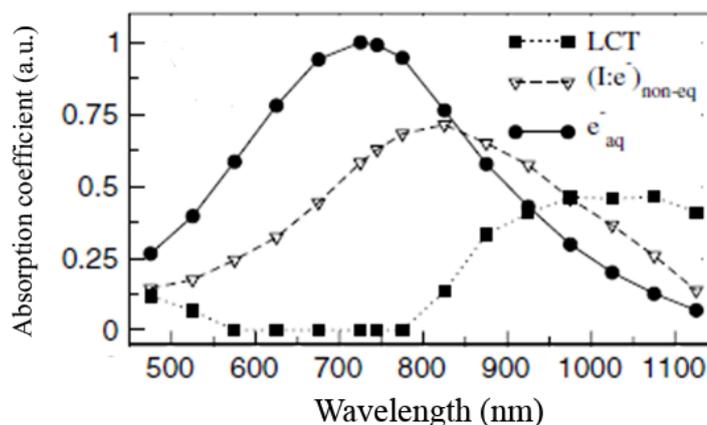
Figure 4.1. Molar absorption coefficients of the intermediates assigned to the initially excited lowest charge transfer state LCT (squares), the transient $(I^0:e^-)_{non-eq}$ state (triangles) and hydrated electron (circles). Reprinted from [184], Copyright (2016), with permission from Elsevier.

Similar results were obtained by Staib *et al*. in the mixed quantum-classical molecular dynamics calculations of the electron photodedatchment from chloride.[51] Their results show an absorption centred at 1130 nm due to the excitation from lowest CTTS state of chloride and the electron separates during the first 100 fs. The relaxation time of the signal observed by Iglev *et al*. at 1000 nm agrees also with an appearance time of the electron after ejection from the CTTS state of iodide obtained by Kloepfer *et al*..[185, 186] In one of these measurements, a transient absorption feature near zero delay, which

does not appear in the case of water ionization, was observed. They suggested that this transient arises from the absorption by the CTTS state of iodide.[185] Also the fluorescence measurements performed by Messina *et al*. after excitation of iodide with 266 nm light shows similar time scales, where the decay of the fluorescence signal from the lowest CTTS state decayed with a time constant of 100 to 400 fs (the life time of CTTS state increase with decrease of emission energy).[46]

According to the above, data measured at 1320 nm may correspond to the excitation from the lowest CTTS state in addition to the second harmonic being resonant with the hydrated electron absorption. Measurements presented here were performed for the three symmetry-allowed polarization combinations: PP, PS and Smix. Excitation of the iodide is achieved with the s-polarized pump with the same plane of incidence as the probe beam.

PP polarization combination
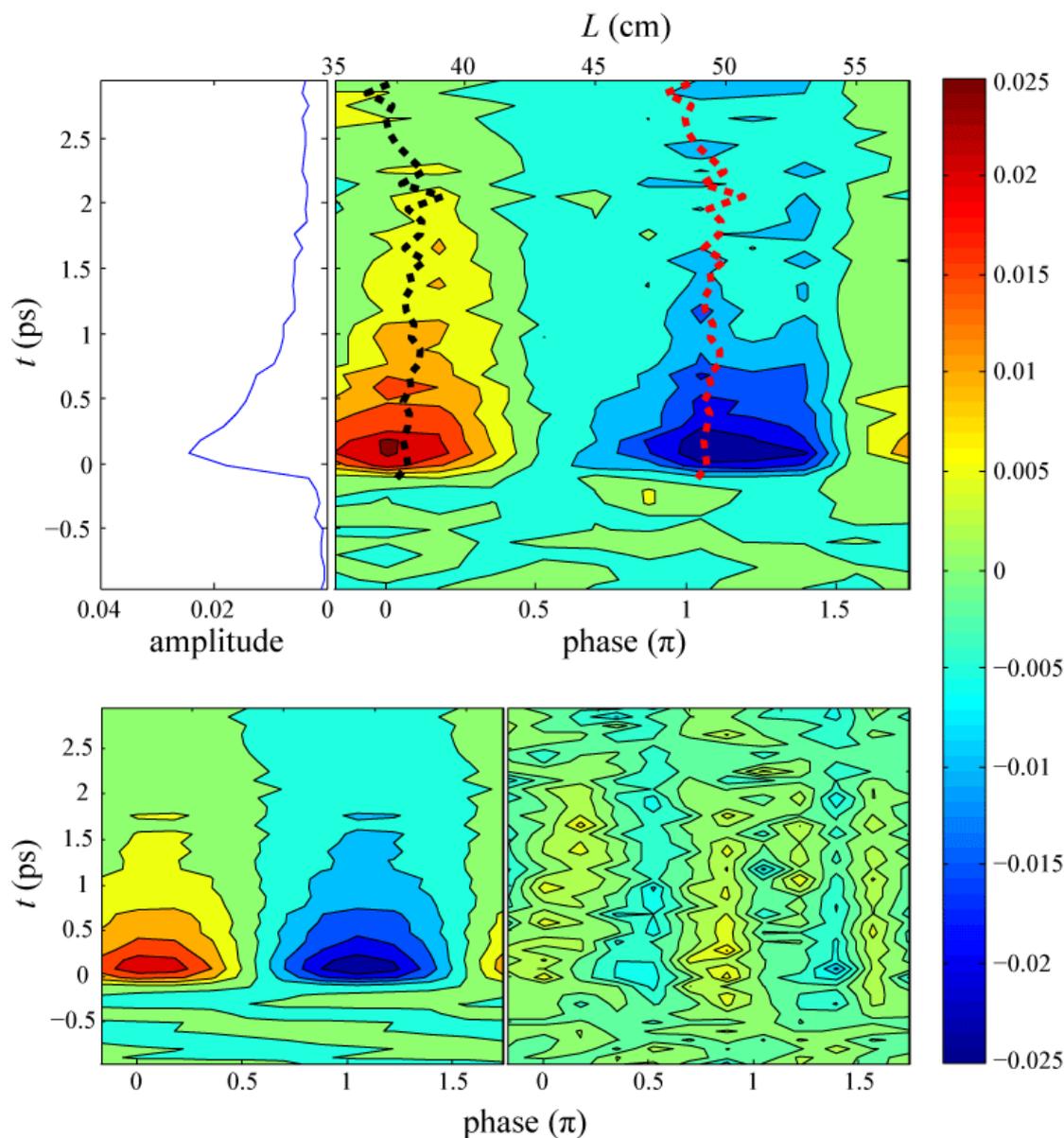
Figure 4.2. Kinetics measured at PP polarization combination (s-polarized pump)(top). The contour plot illustrates the signal from the lock-in measurement as a function of the stage position L (top axis) and phase calibrated using quartz (bottom axis). The black dashed line represents phase changing with time, while the red dashed line the same phase $+\pi$. The left-hand side of the plot shows the amplitude of the signal. The vertical axis of both plots corresponds to the pump-probe delay time. Besides collected data presented are here also global fit obtained for collected data (bottom left), as described in text, and residuals from comparing it with data (bottom right).

The data for the PP polarization combination is shown on Figure 4.2. Time-resolved data for this measurement was taken at 12 different lengths, L, between sample and reference. Data for each L was recorded at 40 different time delay points, where each of this point is an average of 5100 laser shots. Data from the lock-in

measurements here are presented in form of the contour plot. The horizontal axis indicates the length L between the sample and the reference surface as shown on the top of the plot and the associated phase (obtained by calibration with quartz) is shown at the bottom of the plot. The vertical axis of the plot is the time delay between pump and probe pulses. The colours (contours) show magnitude of the signal with the scale shown on the right.

The contour plot also includes the results from a global fit that yields the absolute phase as a function of time and its equivalent shifted by π, as well as the amplitude as a function of time (presented on the left side of the contour plot). The global fit involves fitting sine and cosine functions (each of which is multiplied by a Gaussian function, that accounts for drift of the SHG and LO pulses relative to each other with distance L) at each time delay. The weights of these sine and cosine functions gives two coefficients that state the amount of sine and cosine function at each delay. From this, the amplitude and phase relative to GaAs can be then calculated by means of the Euler's formula:

$$z = x + iy = |z|(\cos\varphi + i\sin\varphi) = re^{i\varphi} \tag{4.1}$$

where x is the weighting of the cosine function y is the weighting of the sine function, $r = |z| = \sqrt{x^2 + y^2}$ is the magnitude (amplitude), and $\varphi = \operatorname{atan2}(y, x)$ is the argument (phase). The absolute phase is then the difference between the observed phase, relative to GaAs, which had been calibrated relative to a quartz crystal placed instead of the sample. The global fit to the data is shown at the bottom left of Figure 4.2, as well as the residual from comparing it to data (bottom right). These residuals for PP polarization combination using 1320 nm probe, are the worst from all results presented in this chapter and provide some indication of the errors associated with the measurements.

The pump-probe data presented in Figure 4.2 shows a very fast rise of a strong initial signal, which then decays quickly over the first picosecond, leaving a small offset. $\chi^{(2)}$ here is primarily real and positive. There is possibly a very small phase shift during the first two picoseconds followed by a slightly larger shift afterwards.

The appearance of phase shifts can imply either the evolution of one species into another or the change of electronic structure of a single species. Therefore, a lack of any large phase shift might suggest that only a single species is being probed. The

observable decrease of the intensity can originate either from the decrease of the concentration of the species or changes in the magnitude of $\chi^{(2)}$. These are, however, not easily distinguishable. Additionally, the absolute values of the amplitudes between different polarization combinations cannot be readily compared. Their values change as the reflections from the surfaces change and magnitude of the generated LO due to different polarizations and wavelengths.

PS polarization combination
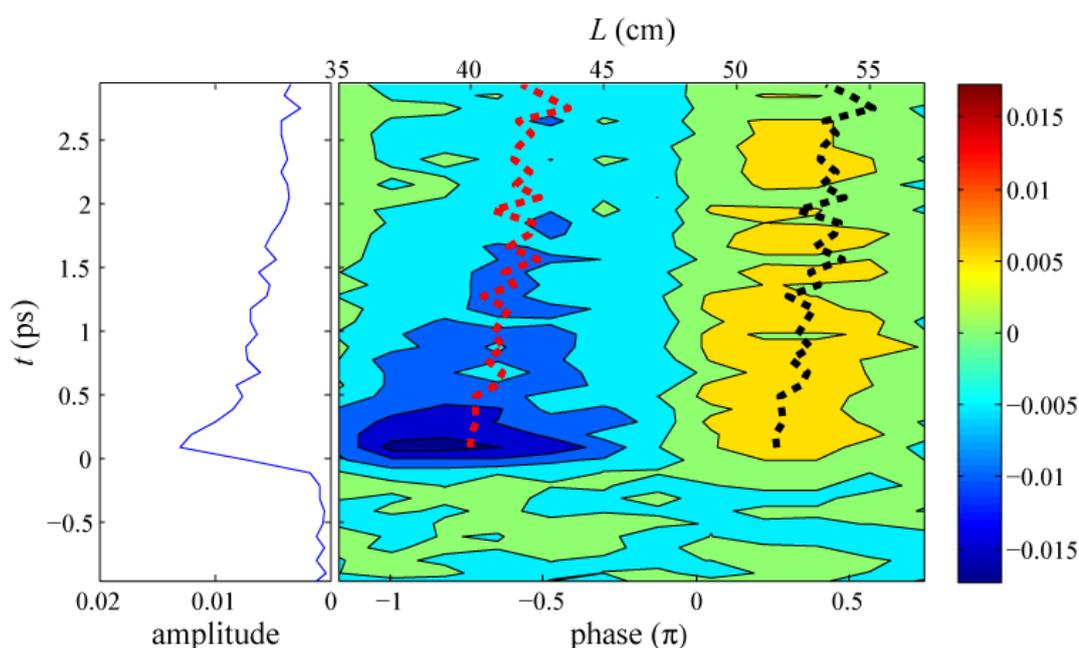
Figure 4.3. Kinetics measured at PS polarization combination (s-polarized pump). See caption of Figure **4.2** for description of the graph.

The data for PS polarization combination is shown on Figure 4.3. Time resolved data for this measurement was taken at 12 different lengths L between sample and reference. Data for each L was recorded at 40 different time delay points, where each of these points is an average of 5100 laser shots. Similar as in case of PP, data recorded for PS polarization combination shows a strong initial signal, which decays in around 1 ps, leaving a small offset. The difference between the maximum signal and the offset is however smaller in case of PS compared to PP. It is not possible here to distinguish if the offsets or the maxima (or both) of the two polarization combination is different. $\chi^{(2)}$ of the observed species in PS polarization is positive and possibly slightly shifts with time towards a more resonant signal.
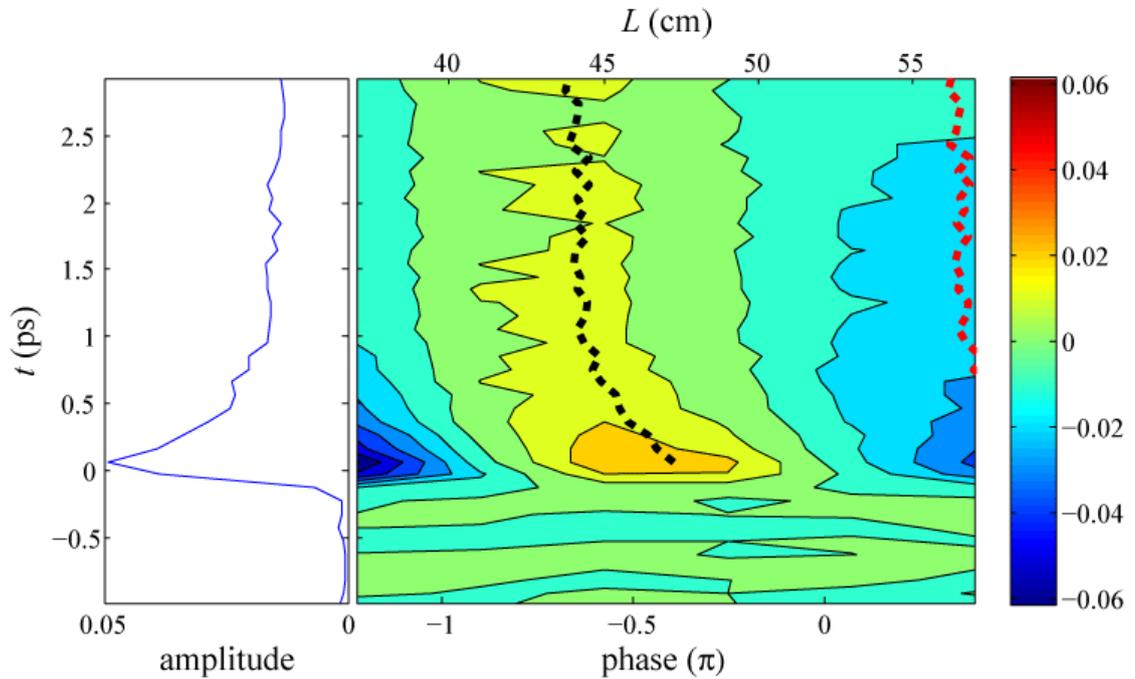
Smix polarization combination

Figure 4.4. Kinetics measured at Smix polarization combination (s-polarized pump). See caption of Figure 4.2 for description of the graph.

The data presented on Figure 4.4 is a result of time-resolved measurements performed at 6 different lengths L. Each of such measurement consists of 40 time delay points being a result of averaging 5100 laser shots. The data for the Smix polarization combination is noticeably different from that obtained for PP and PS polarizations. The observed signal in Figure 4.4 is primarily negative and resonant. A clear phase shift during the first picosecond is also observable, which matches in time the decrease of the initial intense signal. The difference between the maximum signal and the offset is similar in proportion to that from data for PS polarization.

Kinetics

Data obtained using the 1320 nm probe for different polarization combinations differ between each other in phase, in phase shifts and in the ratios of the maximum to the offset at longer times. However, the change of the amplitude over time, and duration of the phase shifts, is in all of them rather similar, showing fast growing signal, that decays in a similar timescale, leaving a smaller offset. Figure 4.5 shows amplitudes of all three polarization combinations with superimposed double exponential function

fitted to each of them with time constants of 220 fs and 700 fs, which are the same as those obtained by Iglev *et al*. for decay of the CTTS state and relaxation of the non-equilibrated contact pair $(I^0:e^-)_{non-eq}$.[184] On the whole, the fitted exponential decay agree very well with the SHG data in all of the polarization combinations (Figure 4.5).
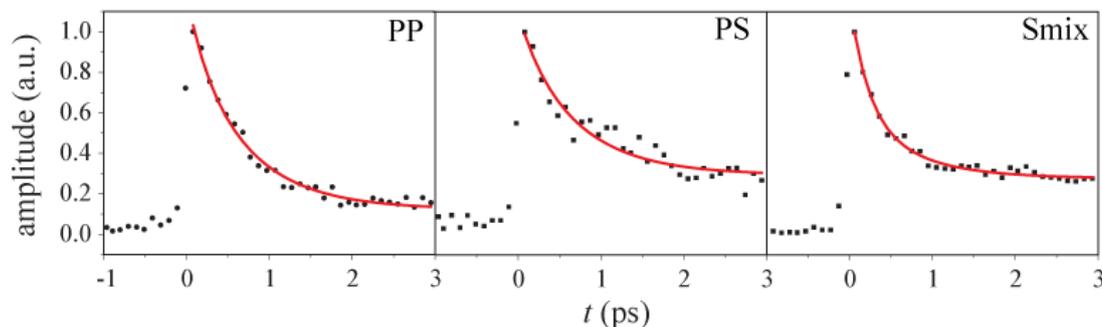
Figure 4.5. Black dots represent data points of the normalized amplitude obtained for PP, PS and Smix polarization combinations at 1320 nm as shown on Figure 4.2,Figure 4.3,Figure 4.4. Red line presents a double exponential function with time constants of 220 fs and 700 fs as obtained by Iglev *et al*. for relaxation of CTTS state and non-equilibrated contact pair $(I^0:e^-)_{non-eq}$, respectively.[184]

Subtraction

All of the performed experiments using iodide presented in this chapter exhibited an offset, which was subtracted in order to obtain the data presented here. An example is shown on Figure 4.6, which shows data obtained for PS polarization before the subtraction where this effect was the most pronounced. A signal offset is visible at time delays 'before' zero indicating it is not a fast time-resolved signal. When measured to time delays of –50 ps, the offset remains constant, but it does disappear in the absence of the pump pulse. The offset was attributed to the signal from long-lived products, which have a lifetime of at least 2 ms (the interval between successive laser pulses). Reduction of the laser repetition rate causes the offset to disappear, however, this also results in a much increased data acquisition time. Reduction of the pump intensity reduces the short-lived pump-probe signal linearly, however, does not affect the offset significantly. The offset was simply subtracted from the data, which could otherwise exhibit misleading phase shifts.
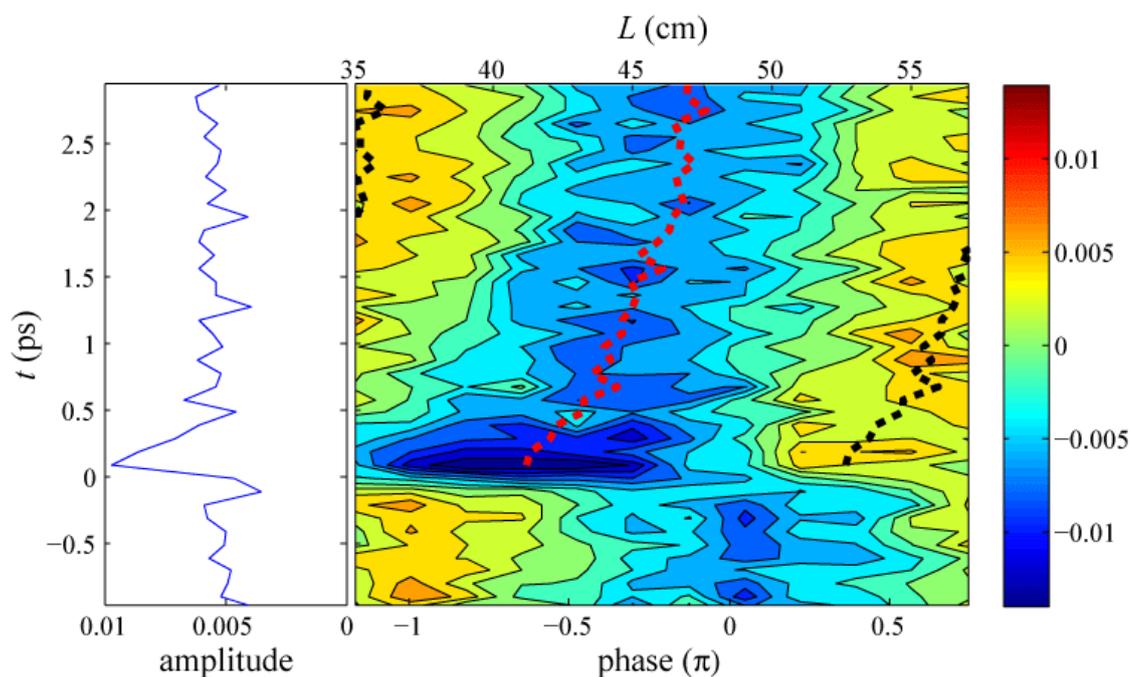
Figure 4.6. Data for PS polarization combination before subtraction of the offset visible here at time delays before zero.

Pump polarization

The experiments were also performed in order to determine possible differences due to different pump polarizations. The measurements taken for iodide with both p- and s-polarized pump beam show no noticeable difference both in amplitude and phase. Figure 4.7 presents detailed kinetic runs measured with PP and PS polarization combinations of the probe after excitation with s- and p-polarized pump. These data were measured at a single point of the phase curve, which gives the largest signal. For PP polarization, data was collected at $L = 49$ cm (as shown on Figure 4.2) and for PS polarization at $L = 41$cm (as shown on Figure 4.3). Each of the 40 delay time points here is an average of 25500 laser shots.
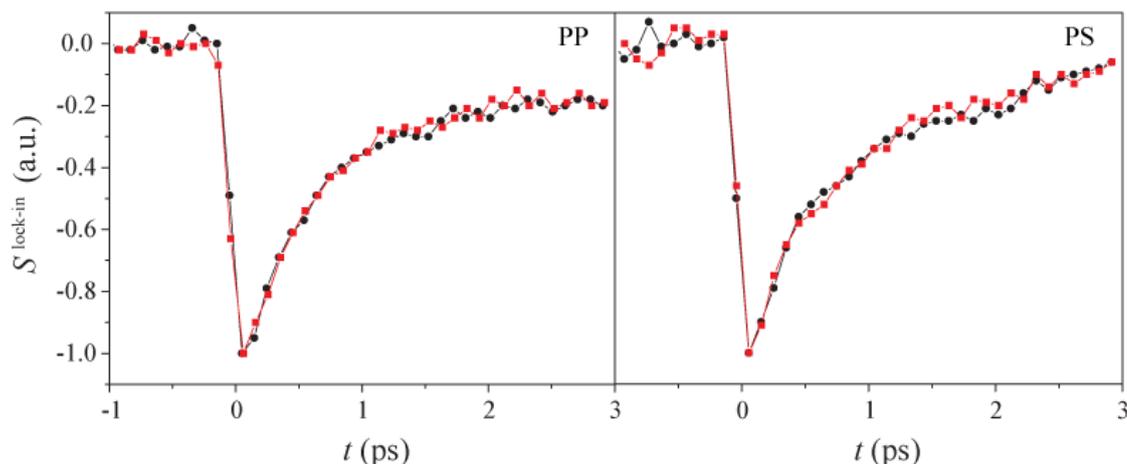
Figure 4.7. Detail kinetic measurements taken at $L = 49$ cm for PP (left) and $L = 41$ cm for PS (right) polarization combinations of the probe, after excitation with p- (red squares) and s-polarized (black dots) pump.

Pump orientation

All the data shown this far has been obtained for the measurements taken using a pump and probe (1320 nm) that shares the same plane of incidence. With this arrangement, data were collected at all possible polarization combinations: PP, PS, Smix, SP and SS. Data for SP and SS polarization combinations were not shown here, because these polarization combinations are not allowed at the interface between two isotropic media, and no signal was observed in this case. However, various measurements were also performed with pump and probe beams no longer sharing the same plane of incidence, but instead had ~3.5° difference between the two planes. Data obtained at this configuration for PP, PS and Smix polarization combinations are very similar to the data shown in Figure 4.2, Figure 4.3 and Figure 4.4, respectively, and are not reproduced here. However, besides these "symmetry allowed" polarization combinations, the pump-probe signal was also observed for SP and SS polarization combinations as shown in Figure 4.8. In order to ensure Smix polarization combination is not the source of the detected signal, presented data were obtained by taking a number of small perturbations ($< 5°$) from a purely p- or s-polarized input beam and picking the component that varies as $\cos^2\vartheta_p$, where ϑ_p is the polarization angle away from the pure polarization. These data were obtained from experiments performed at 12 different lengths L, where each consists of 40 points at different delay times. Each time delay

point is an average of 2664 laser shots for SP and 3400 laser shots for SS polarization combinations.
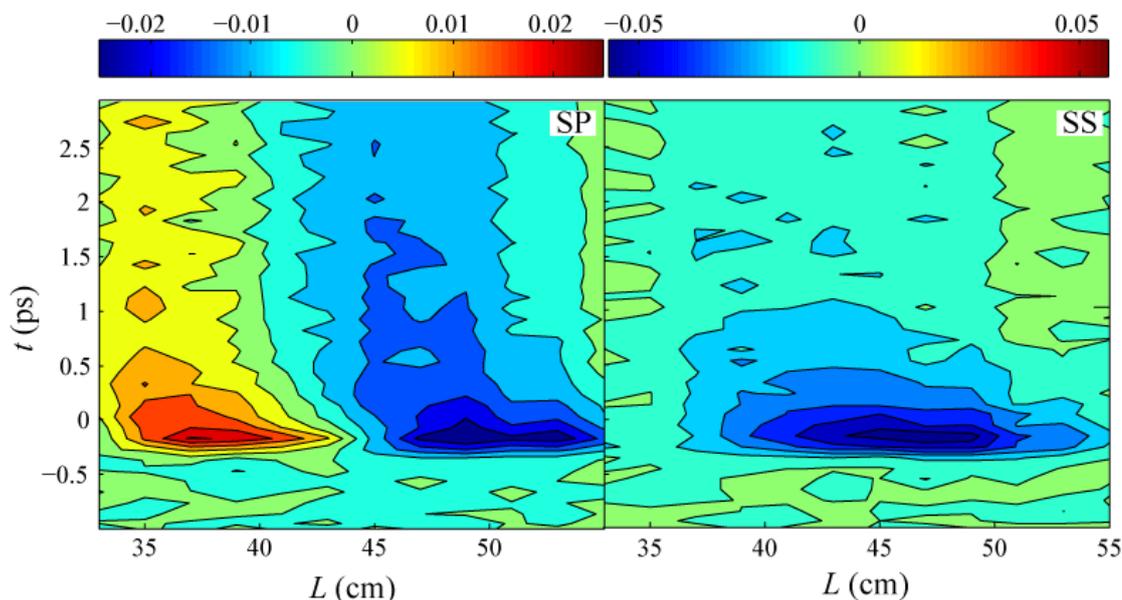
Figure 4.8. Kinetics observed for SP (left) and SS (right) polarization combinations in case when pump and probe has planes of incidence different by ~3.5°. Instead of measuring directly, due to the risk of the signal originating from the mixture of p and s polarization, data here were obtained by taking a number of small perturbations (<5°) from the purely p or s polarization of the incident fundamental beam and picking the component that varies as $\cos^2 \vartheta_p$, where ϑ_p indicates the angle away from the pure polarization.

The observable pump-probe signal for SP and SS polarization combination when the pump and probe beams do not share plane of incidence, suggests that the observed species has a different symmetry than that of the interface, which has ∞m ($C_{\infty v}$) spatial symmetry. This result can be justified if the observed species follows the symmetry of the pump beam which created it.

4.2   Dynamics with a 800 nm probe

In order to avoid the possible resonance following excitation of the CTTS state at the probe wavelength, the experiments were also performed using an 800 nm probe. The fundamental of the probe in this case is resonant with the hydrated electron p ← s transition. However, following the results obtained by Iglev *et al.* mentioned earlier, at early times, the fundamental of the probe is also resonant with the intermediate state

assigned as the non-equilibrated contact pair $(I^0{:}e^-)_{non-eq}$.[184] The absorption band obtained by them for this intermediate peaks at 825 nm (Figure 4.1) and decays to the equilibrated contact pair $I^0{:}e^-$ with the time constant of 700 fs.

Below, data for PP, PS and Smix polarization combinations using a probe at 800 nm are presented. There might be resonance-enhancement with both hydrated electron (or contact pair $I^0{:}e^-$) and precursor to the equilibrated contact pair $(I^0{:}e^-)_{non-eq}$. Additionally, the second harmonic of the probe at 400 nm can also be resonant with the hydrated electron. An s-polarized pump sharing the same plane of symmetry as the probe beam was used.

PP polarization combination
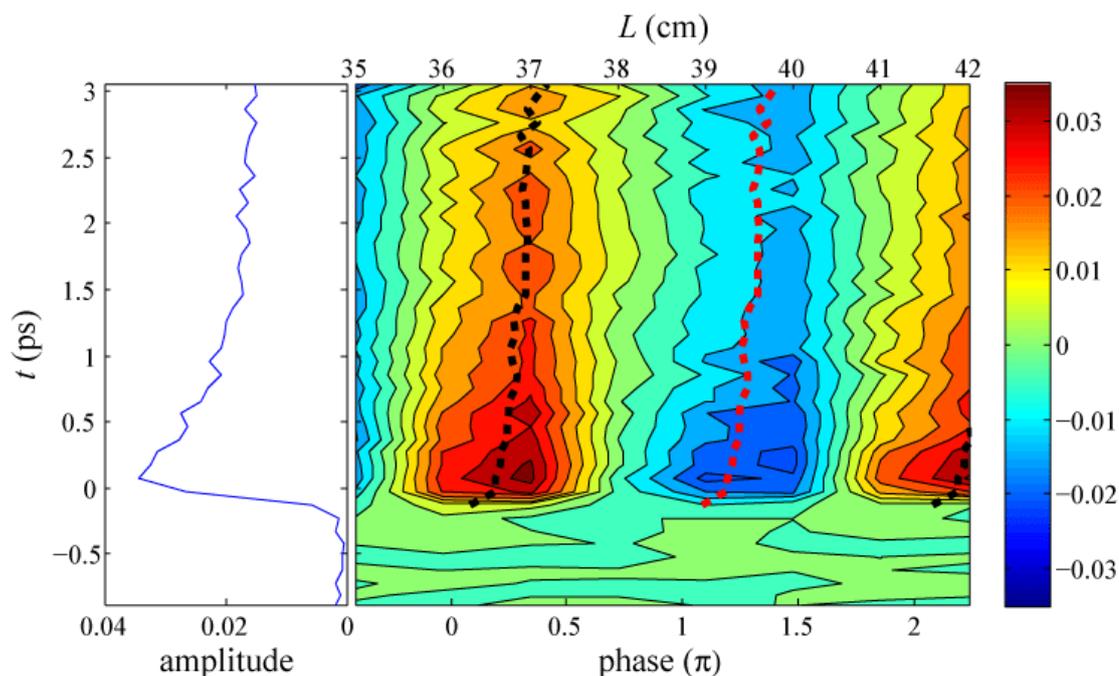
Figure 4.9. Kinetics measured for PP polarization combination (s-polarized pump). See caption of Figure 4.2 for description of the graph.

The data for PP polarization at 800 nm fundamental of the probe is shown on Figure 4.9. The contour plot is a result of 8 time-resolved measurements at different lengths *L*. Each of those measurements consists of 40 time delay points, where each is an average of 5100 laser shots. The signal is positive and experiences a small phase shift at early times, less than a picosecond. The phase shift occurs toward the signal being more resonant. The ratio between the maximum signal and offset at longer times

is much smaller here than in case of the same measurement with probe at 1320 nm. Also the decay of the initial signal might be slightly slower than in case of 1320 nm probe.

PS polarization combination

Figure 4.10. Kinetics measured for PS polarization combination (s-polarized pump). See caption of Figure 4.2 for description of the graph.

The data obtained for PS polarization combination with probe beam at 800 nm shown in Figure 4.10 is composed of 8 time-resolved measurements at different lengths *L*, with 40 time delay points. Each of the points is an average of 5100 laser shots. Results obtained here are significantly different than any other result presented this far as do not show a strong initial signal. Instead, appearance of the pump-probe signal is followed by a very slow decay making the amplitude observed in the measured time almost constant. However, it is possible that the initial signal as observed in other results is still measured, but the ratio between it and the offset change such that it is equal to it or buried in the offset signal. The phase of the measured pump-probe signal is positive and does not exhibit any phase shift for majority of the time delays here. The only phase shift observable here is a very fast shift occurring around zero time delay from more resonant towards more non-resonant signal, which occur in time ~100 fs. This might point towards an earlier suggestion that the early signal shown on results

obtained with different conditions (different wavelength or polarization combination of the probe) might still be measured but it is buried in the signal from the offset. As shown for example in Figure 4.9, the PP polarization signal at early time has slightly different phase than measured at longer time delays as well.
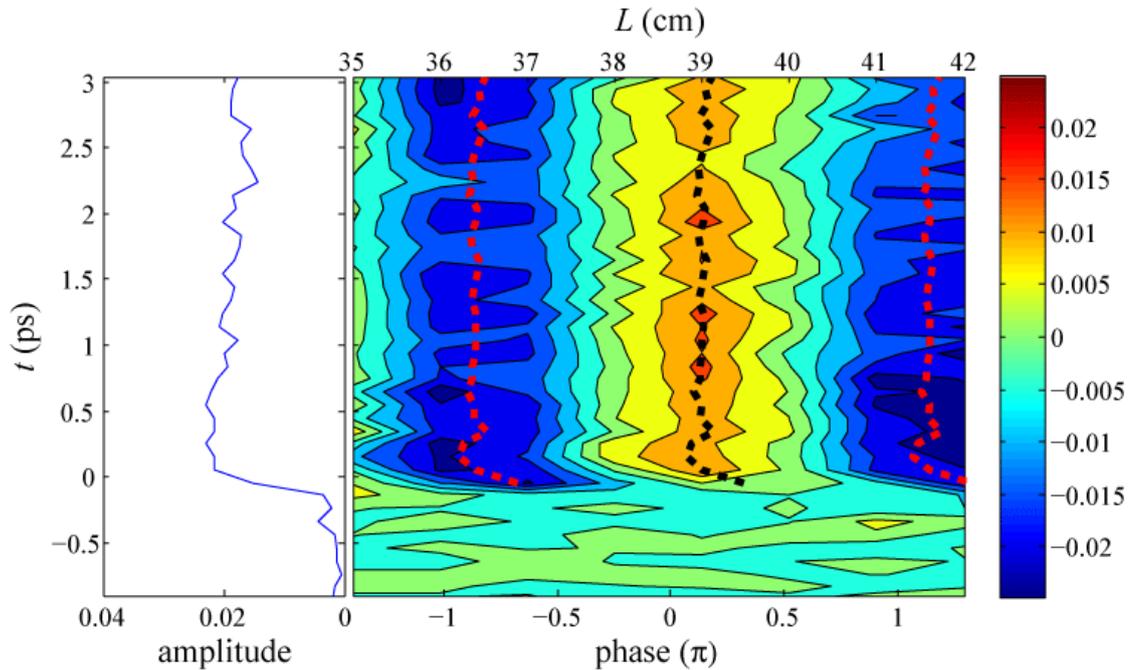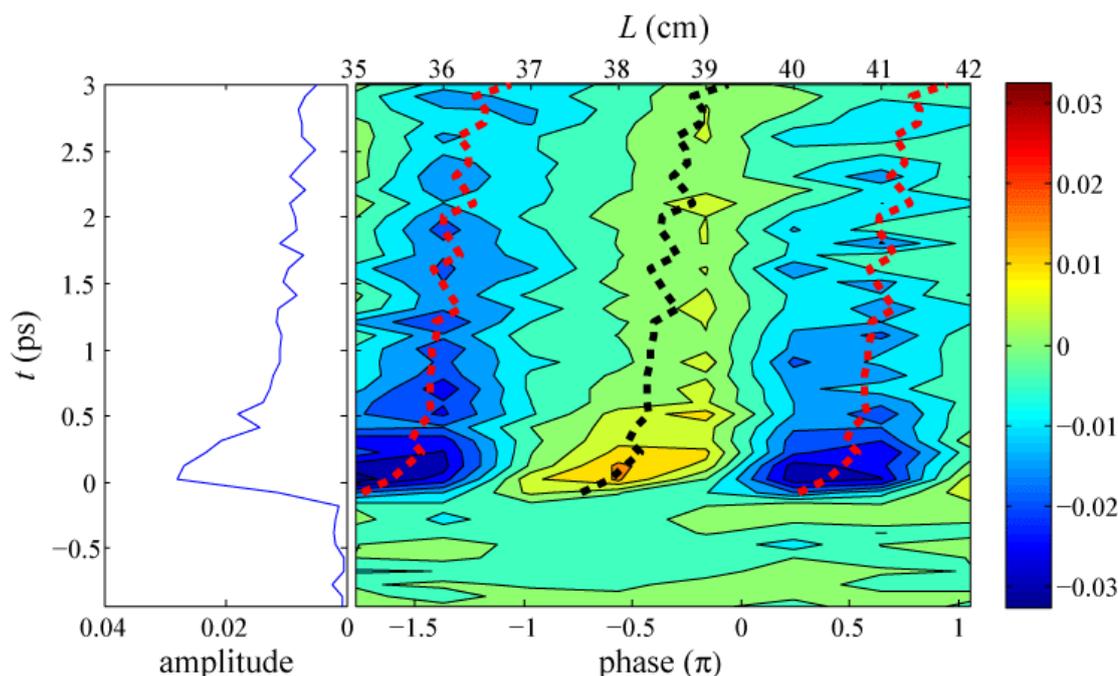
Smix polarization combination

Figure 4.11. Kinetics measured for Smix polarization combination (s-polarized pump). See caption of Figure 4.2 for description of the graph.

The data collected for measurements with Smix polarization combination of 800 nm probe is shown in Figure 4.11. The contour plot consists of 8 time-resolved measurements at different lengths L, with 40 time delay points. Each of the time delay points here is an average of 6375 laser shots. The ratio between the maximum of the initial signal and the offset measured for Smix polarization is bigger than in the case of PP polarization, however, it shows similar decay time. The pump-probe signal resembles the signal obtained from a 1320 nm probe with the same polarization combination. The phase of the signal is negative and it exhibits the most pronounces phase shift of all polarization combinations measured for this wavelength, which changes going through a resonant signal. The difference between the Smix measurement

at 800 nm and 1320 nm probe is that the phase shift of the former occurs in the opposite direction, from more negative to more positive.

Kinetics

As shown for the data at 1320 nm probe beam, the amplitudes for measurements with 800 nm probe are summarized next to each other on Figure 4.12. On the plots are superimposed fits of the single exponential function to each data set with time constant of 700 fs. This was done because the 800 nm can result from probe beam being in resonance with the non-equilibrated contact pair $(I^0:e^-)_{non-eq}$, as discussed by Iglev *et al.*.[184] For PP and Smix polarization combinations, the single exponential functions fit the measured data rather well. In the case of PS polarization, the initial strong signal is not pronounced making this comparison difficult, but nevertheless broadly shows this decay. Additionally, the appearance of the pump-probe signal might be slightly slower than in the case of data collected for 1320 nm probe, which would be expected if the observed signal appear after relaxation of the CTTS state.
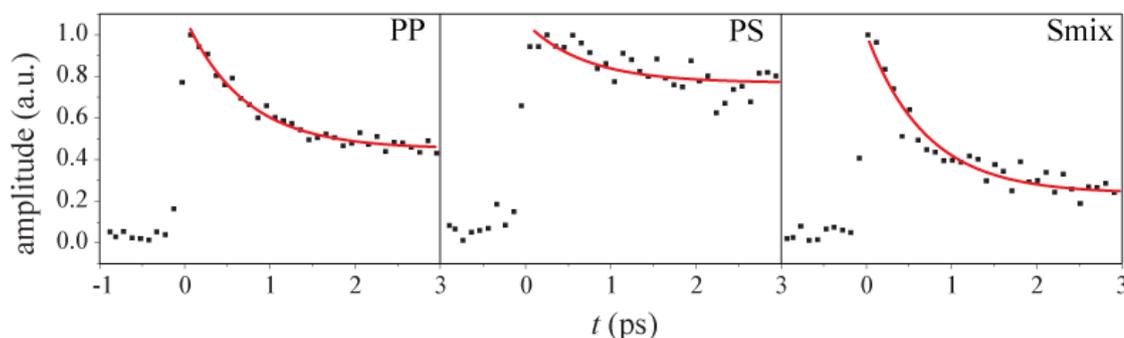
Figure 4.12. Black dots represent data points of the normalized amplitude obtained for PP, PS and Smix polarization combinations at 800 nm as shown on Figure 4.9, Figure 4.10 and Figure 4.11. Red line presents a single exponential function with time constants of 700 fs as obtained by Iglev *et al.* for relaxation of the non-equilibrated contact pair $(I^0:e^-)_{non-eq}$.[184]

4.3   Long-time kinetics

The time-resolved phase-sensitive experiment on hydrated electron detached from iodide was also performed over longer time delays. Data collected at PP

polarization combination for time delays reaching 100 ps, using 1320 nm fundamental probe beam with p-polarized pump beam, is shown in Figure 4.13. The data was collected with pump beam plane of incidence 3.5° shifted to probe beam plane of incidence. However, for PP polarizations at early times, no difference was observed between a 3.5° and a 0° difference in incidence planes. The contour plot consists of 6 time-resolved measurements at different lengths L, each being a result of 100 points with different time delays. Each of the time delay points here is an average of 6800 laser shots.
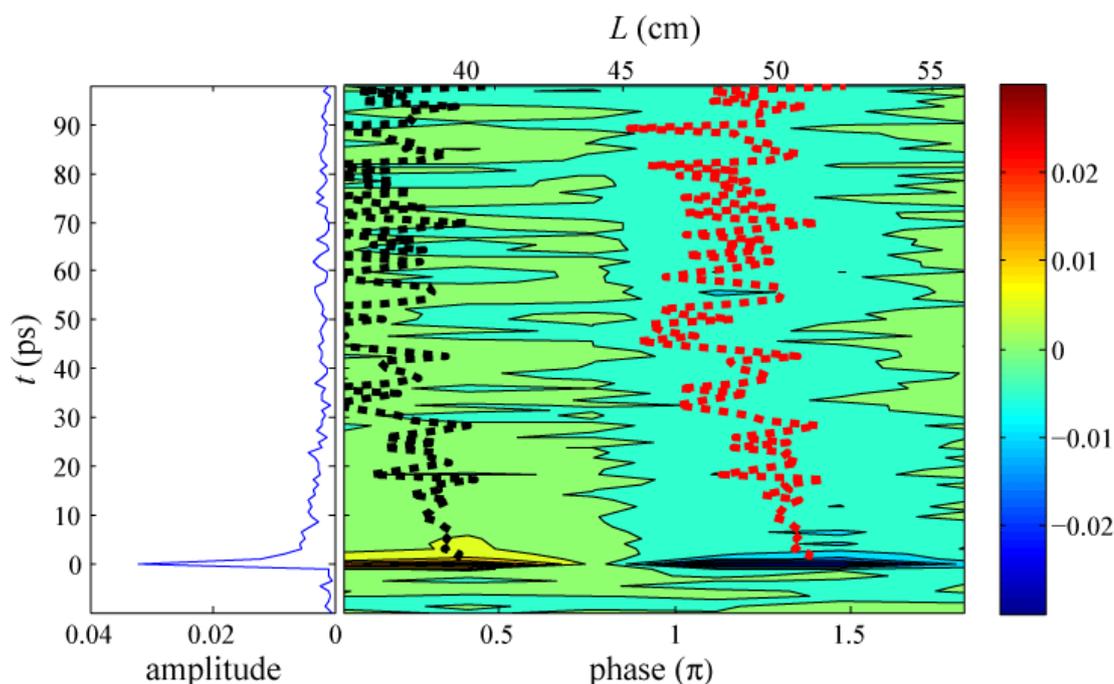
Figure 4.13. Kinetics measured in PP polarization combination (p-polarized pump). See the caption of Figure 4.2 for an explanation of the graph.

Besides the small phase shift at short time (< 3 ps) shown earlier, Figure 4.13 shows an additional phase shift occurring over a 30 ps timescale. This timescale resembles the inverse rate of the recombination of the hydrated electron with the parent ion as obtained by Kloepfer *et al*. for the electron-iodine contact pair in bulk (33 ps). In these transient absorption experiments, iodide was pumped at 255 nm and probed at both 510 and 800 nm.[186] The electron ejected from the CTTS state is located in the close proximity to the iodine forming a contact pair I^0:e$^-$, with rate k_p.[50] Such pair can then either dissociate, with rate k_d, forming separate hydrated electron and iodine atom, or undergo geminate recombination, with rate k_n, reforming iodide (Figure 4.14).[51]
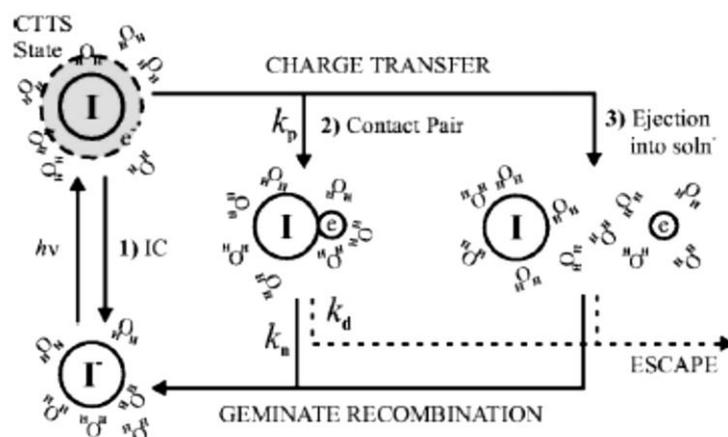
Figure 4.14. Scheme showing possible routes following excitation of the iodide to its CTTS state and their rates. 1) Internal conversion to the ground state iodide; 2) forming a I^0:e^- contact pair; 3) ejection of the electron far into the solvent. Reprinted with permission from [186]. Copyright (2016), AIP Publishing LLC.

The kinetic model considering these events was proposed by Staib *et al.* for electron ejection from the CTTS state of chloride, where a time-dependent signal constructed from the number density $N(t)$ of the contact pair and the hydrated electron is:[51]

$$N(t) = \frac{k_d}{k_d + k_n} + \frac{k_p}{k_d + k_n - k_p}\left[\frac{k_p - k_d}{k_p}\exp(-k_p t) - \frac{k_n}{k_n + k_d}\exp(-(k_d + k_n)t)\right] \quad (4.2)$$

Using this kinetic model, Kloepfer *et al.* obtained time constants of 33 ps and 70 ps for geminate recombination ($1/k_n$) and electron escape from the pair ($1/k_d$), respectively, following CTTS from iodide.[186]

The kinetic model in equation (4.2) was fitted to the amplitude shown in Figure 4.13 and is shown in Figure 4.15. The kinetic model ignored the initial spike in signal, which is believed to originate from the precursor state of the contact pair. The time constants of 23 ± 4 ps for geminate recombination and 54 ± 13 ps for electron escape were obtained, which are close to times obtained by Kloepfer *et al.* (Figure 4.15).

The results obtained here support the bulk kinetic model and suggests that at the surface the formation of the I^0:e^- contact pair occurs. However, the hydrated contact pair and free electron might have different resonances, as indicated by a phase change shown on Figure 4.13.
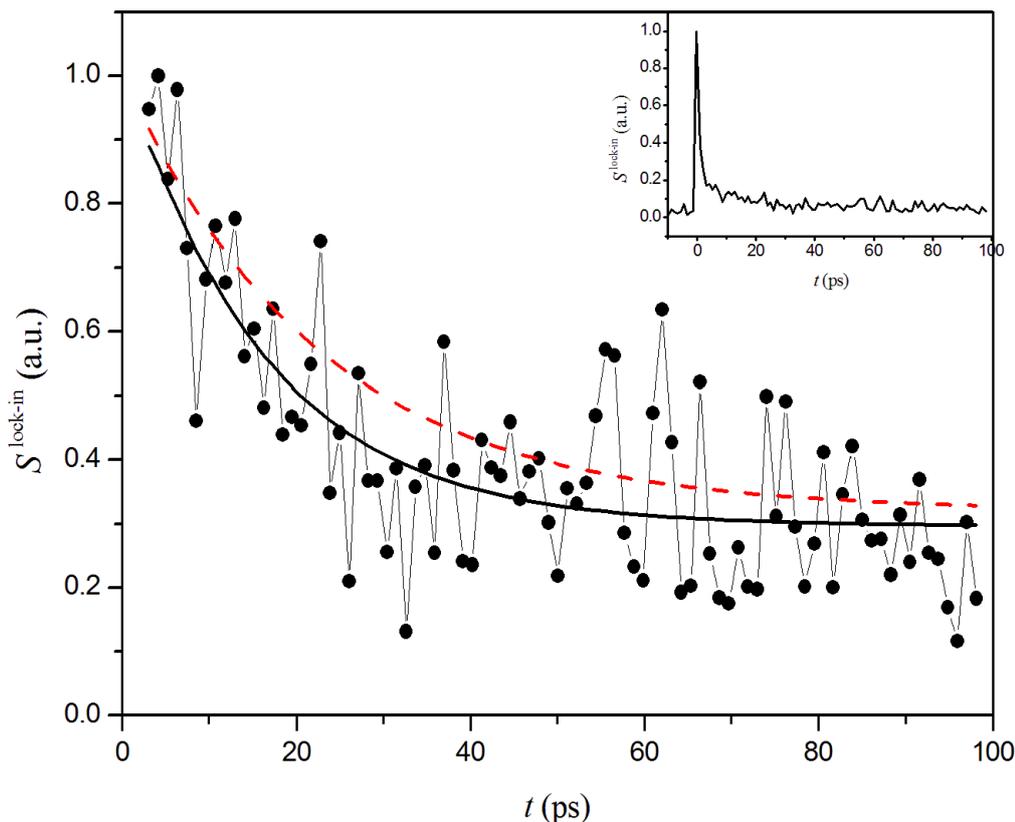
Figure 4.15. Black dots connected by a thin line are normalized time-dependent amplitude from kinetics measured in PP polarization combination (with p-polarized pump) excluding the initial spike (whole time-dependent amplitude showed in the inset). Black line presents fit to data using model described in equation (4.2). Red dashed line presents fit obtained by Kloepfer *et al.* using the same model.

4.4   Potassium ferrocyanide

In addition to experiments in which the hydrated electron was ejected from the iodide, experiments using potassium ferrocyanide were also performed. Excitation of the ferrocyanide ion, $[Fe(CN)_6]^{4-}$, with light at wavelengths $\lambda \leq 313$ nm results in the ejection of an electron via a CTTS state.[187] This process has a high quantum yield, which is associated with the small geminate recombination due to a strong Coulomb repulsion between the solvated electron and ferrocyanide 3– anion that leads to a large electron ejection distance. Lenchenkov *et al.*, from their multicolour pump-probe spectroscopy studies of the electron photodetachment from $[Fe(CN)_6]^{4-}$ in the bulk, observed relaxation behaviour similar to the ejection of the electrons from two-photon ionization of water, and a longer appearance time of the hydrated electron as compared

to ejection from water or iodide.[188] Assuming a diffusion limited geminate recombination, they estimated an ejection distance of ~15 Å of the electron. This is in contrast to the ejection of the electron via CTTS state by iodide or chloride, which occurs at small distances creating a contact pair.[51, 186, 189] Moreover, ferrocyanide is repelled from the surface. Therefore, signals due to the hydrated electron measured by SHG from the water/air interface are not necessarily expected. However, the possibility exist that, due to the long ejection length and high yield, a weak signal may appear at longer time scale as a fraction of the produced hydrated electrons diffuse from bulk towards the surface.

For this experiment, a 0.5 M solution of potassium hexacyanoferrate (II) trihydrate, $K_4Fe(CN)_6 \cdot 3H_2O$, (Sigma-Aldrich, BioUltra, ≥99.5%) with high purity water was used. Measurements were performed using 1320 nm fundamental probe beam with p-polarized 250 nm pump. The pump beam plane of incident was at 3.5° relative to the probe beam plane of incidence. Data were collected for the PP polarization combination and are presented in Figure 4.16. The contour plot consists of 6 time resolved measurement performed at different lengths L, with 40 time delay points each. Each of the time delay points here is an average of 3400 laser shots.
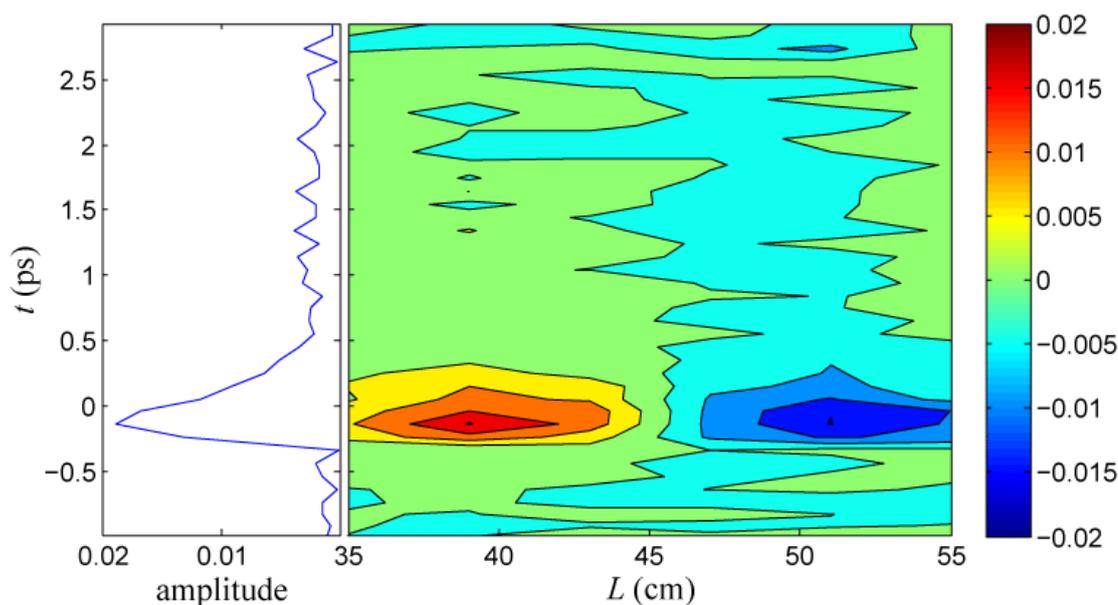
Figure 4.16. Kinetics measured in PP polarization combination (p-polarized pump) for 0.5 M solution of potassium ferrocyanide in water. See the caption of Figure 4.2 for an explanation of the graph.

Figure 4.16 shows signal at early times, which decays rapidly to leave a very weak signal after around 500 fs. Due to the fast decay of the initial signal and low signal level at longer delays, it is not clear if any phase shift occurs. The amplitude kinetics resembles the kinetics measured by Gauduel *et al*..[190] In their experiment, they irradiated a 0.45 M ferrocyanide solution with 310 nm light and subsequently observed an electron solvation dynamics by transient absorption at various wavelengths. Special attention was given on the dynamics measured at 1250 nm, which they assigned to the prehydrated electron. From their measurements, they obtained time constants of 120 fs and 240 fs for the signal appearance and relaxation, respectively. Figure 4.17 shows our data with single exponential functions superimposed for the appearance and decay of the signal with time constants as those obtained by Gauduel *et al*.. A best fit to our data gives a slightly longer relaxation time constant of 290 fs and a similar appearance around 120 fs (although this fit is based on very few data points). We note, however, that these timescales are very close to our time resolution (and also those by Guaduel *et al*.). The good agreement between our data and that of Gauduel *et al*. using 1250 nm probe, might suggest that the pump-probe signal visible on Figure 4.16 originates entirely (or at least mostly) from the resonance with the fundamental 1320 nm probe and not its second harmonic (at 660 nm).
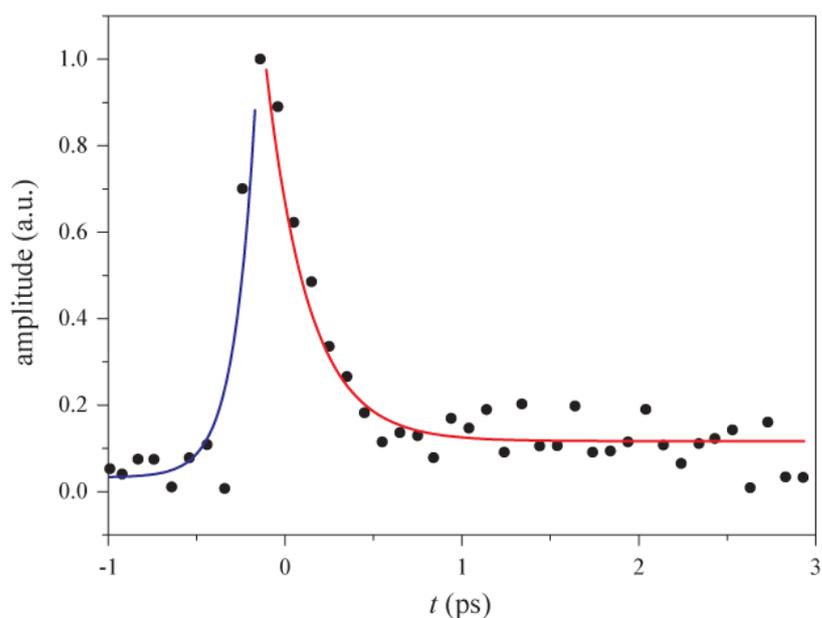
Figure 4.17. Black dots represent normalized data points from the amplitude as seen on Figure 4.16. Blue and red lines are single exponential functions with time constants 120 fs and 240 fs, as obtained by Gauduel *et al*. for appearance and relaxation of signal measured at 1250 nm after irradiation of 0.45 M with 310 nm pump, respectively.

Measurements over a time delay reaching 200 ps were also made, however, no rise in the signal or phase shift was seen on this time scale. This time scale might, however, still be insufficient to observe diffusion of the electron towards surface, if this occurs.

4.5   Reflectivity

In all of the lock-in time-resolved SHG measurements presented in this work, we have assumed that the reflectivity of the sample surface remains constant during the experiment. However, in reality this changes slightly when the hydrated electron is formed. A sample solution of NaI will have different refractive index with and without the hydrated electron in it, thus the reflectivity might change. As a consequence, the amount of fundamental light reflected from the sample, which produces LO, will depend on the presence of the hydrated electron in the sample. The change in the reflectivity can be measured by looking at the pump-probe kinetics of the S_2 measurement ($S_2 \propto |E_{SHG}|^2 + |E_{LO}|^2$) of the lock-in measurement (equation 3.4), i.e. in which the beams pass through the glass window between the sample and reference surface (Figure 3.10), thus resulting in lack of the interference term. Under the conditions used throughout this work experiments $|E_{SHG}|^2 \ll |E_{LO}|^2$ and thus it can be assumed that $S_2 \propto R^2$ where R is the reflectivity of the sample at the fundamental wavelength.

Figure 4.18 shows the reflectivity obtained for 800 nm and 1320 nm with PP and PS polarization combinations. The data are averaged time-resolved measurements from all performed L positions. The biggest change in the reflectivity is observed for 800 nm light, which might be due to the hydrated electron absorption band, which has its maximum at 720 nm. For 1320 nm light, changes in the reflectivity are only seen at short times, which is expected since the absorption band of the precursor to the hydrated electron is accessible at this wavelength. At both wavelengths s-polarized light experiences a decrease in reflectivity, while p-polarized light experiences an increase. Additionally, the change in reflectivity is bigger for s-polarized light.
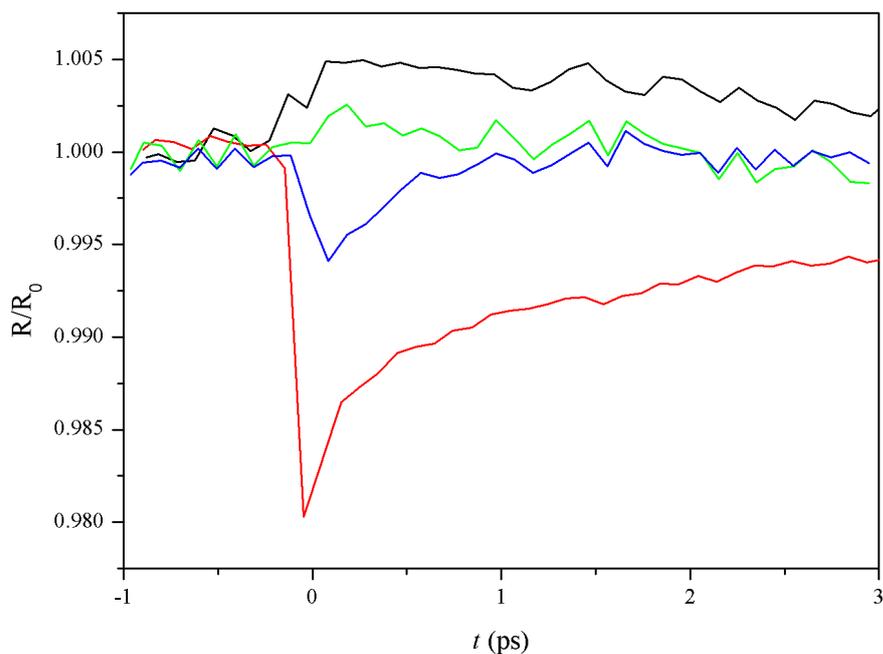
Figure 4.18. Time-resolved reflectance signal for: black line – p-polarized 800 nm light; red line – s-polarized 800 nm light; green line – p-polarized 1320 nm light; blue line – s-polarized 1320 nm light. In all cases pump beam was s-polarized.

Besides the effect on the intensity of the generated LO, the reflectivity will also manifest itself in the SHG from the sample surface. As described in chapter 2, the intensity of the SHG generated at the surface depends on the refractive index of the media (in chapter 2 this is indicated by angle ϑ_t, which depends on refractive index, necessary to get the component of the wave vector k_{2z} and Fresnel transmission coefficients). Unlike the intensity of the LO term, which appears as an intensity reduction across the whole phase curve, the change in SHG from the sample surface due to the change in refractive indices will show phase behaviour, which in the investigations presented here is indistinguishable from the change in $\chi^{(2)}$.

4.6 Discussion

The results showed an evolution of the hydrated electron ejected from iodide following excitation of iodide to its lowest CTTS state measured at the water/air interface. Due to the different probing wavelengths used, different intermediate states of the creation of the hydrated electron could be observed. As such, in agreement with investigations in bulk, the process which was observed can proceed as follows.

The 250 nm pump probe excites iodide to its lowest CTTS state. The CTTS state is observed with a 1320 nm probe. The 1320 nm probe excites the lowest CTTS state to the higher-lying states and the decay of the signal corresponds to the ejection (or separation) of the electron from the CTTS state (iodide centred). This happens at a timescale of ~200 fs. The newly ejected electron is located in close proximity to the iodine atom and forms a contact pair, as described in detail in the bulk.[42, 49-51] This initially non-equilibrated pair is then probed with the 800 nm probe (and partly with second harmonic of the 1320 nm at 660 nm). As the pair equilibrates in water, its absorption spectrum shifts towards shorter wavelengths. This happens at a timescale of ~1 ps. The equilibrated pair is then probed through resonance-enhancement of the SHG of the 1320 nm, or at probe at 800 nm and the second harmonic of it at 400 nm. The contact pair can then either undergo geminate recombination forming iodide, or dissociate forming separate iodine atom and hydrated electron. These happen then at ~30 ps and ~70 ps timescales, respectively.

These processes are observed as decays of the signal with time, as well as phase shifts in phase-sensitive measurements. According to the above hypothetical description of the origin of the observed pump-probe signal, the biggest difference between measurements performed using 1320 nm and 800 nm probe is that the former can additionally probe the CTTS state. Therefore, it would be expected that the biggest difference between two probes is observed at early time delays. This is observed for PP and PS polarization combinations, while in case of Smix both probes wavelengths give similar results. Figure 4.19 presents a comparison of the amplitudes obtained with different polarization combinations for 1320 nm and 800 nm probes normalized to match the long-time offset. It can be noticed here, that the difference between PP and PS with both probes has the same trend, where the initial signal appears weaker in case of PS polarization combination. However, the magnitudes cannot be directly compared between different probe wavelengths or different polarization combinations.
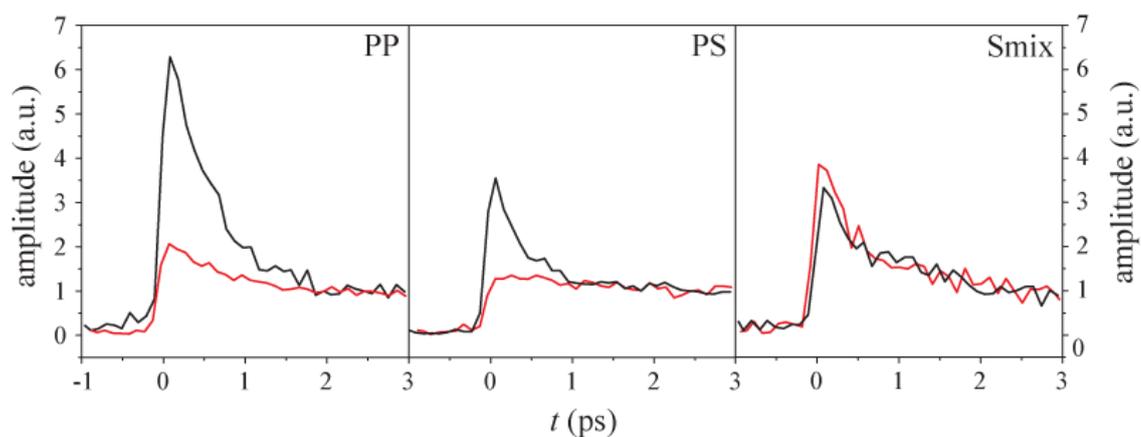
Figure 4.19. Comparison of the obtained amplitudes using 1320 nm (black line) and 800 nm (red line) probe, with different polarization combinations. Amplitudes were normalized to match at delay time ~2.5 ps.

The amplitudes as well as phase information from the Smix polarization combination differs significantly from the other measured polarization combinations. The amplitude in this case seems to be nearly identical for 1320 nm and 800 nm probes. Phase for Smix is negative and exhibits strong shift, as opposed to PP and PS polarization combinations, which exhibit positive phase with small or no shifts. Exhibited phase shifts in Smix measurements occur in opposite directions for 1320 nm and 800 nm probe. Additionally, the data collected with different pump and probe planes of incidence for SP polarization combination exhibit similar strong phase shift. However, as it was performed using only 1320 nm probe and the phase calibration was not performed, no more details can be obtained in that case.

The above observations seem to indicate a significant difference when either p- or s-polarized signal is collected by the detector. Different behaviour of the electron could be caused by the presence of air or iodine atoms. If for example the ejected electron has a part protruded slightly in the air phase, either just after the ejection or after equilibration (or both), then its air and water phase would differ from each other. Therefore the SHG measured in z axis may be expected to be different then in the y or x axis. Similarly, an iodine atom located next to the ejected electron might also influence the electron. From the long-time measurement (Figure 4.13), the separation from iodine manifests itself with a small but measureable phase shift. If the electron would have a preferential site where it locates against the iodine, such a difference in the probed direction could be expected as well in this case. There is no reason to expect such

behaviour in the bulk, however, in case of an iodide located at the surface, the electron could potentially locate itself in specific preferential orientation. Near the surface, the water structure is not as compact as in the bulk, creating possibly more voids into which electron could be ejected. In that case, an electron located next to iodine in the xy plane could result in different signal with detected s- compared to p-polarization. A way to test this could be, for example, to study the electron ejected from other systems, where it does not create a contact pair. For example, more detailed studies using ferrocyanide should be performed. This was done only using 1320 nm probe and PP polarization combination, but repeating this for all polarization combinations and other probe wavelengths would be useful.

The detected signals could also possibly originate from other sources. For example, the time-resolved signal could arise from changes in the water non-resonant background. Note that the detected pump-probe signal in some of the measured polarization combinations is primarily real and positive, as opposed to real and negative measured for non-resonant water.[134, 191] Therefore, the signals could be explained by a disruption of the water structure due to the ejection of the electron. However, as the used probe wavelengths are not in resonance with water, the obtained signal should not depend on probe used. Nevertheless, if the non-resonant signal from water would be strong enough, it could interfere with the resonant signal. The same applies to iodide. Iodide located at the surface takes an asymmetric shape, which then changes after excitation and ejection of the electron. This could potentially be observed using SHG technique. However, similar as in case of water, the used probes are not resonant with transitions of iodide or iodine and the resulting signal would be non-resonant. The imaginary and real parts of the performed measurements are shown in Figure 4.20. As it was mentioned before, phase-sensitive measurements enable the real and imaginary parts of the measured signal to be obtained, which correspond to non-resonant and mostly resonant signal, respectively. Figure 4.20 presents real and imaginary parts obtained from the normalized amplitudes, as shown on Figure 4.19. The real signal in all of the polarization combinations depends strongly on the probe wavelength used, which provides evidence that the measured pump-probe signal originates from the generated electron (and CTTS state).
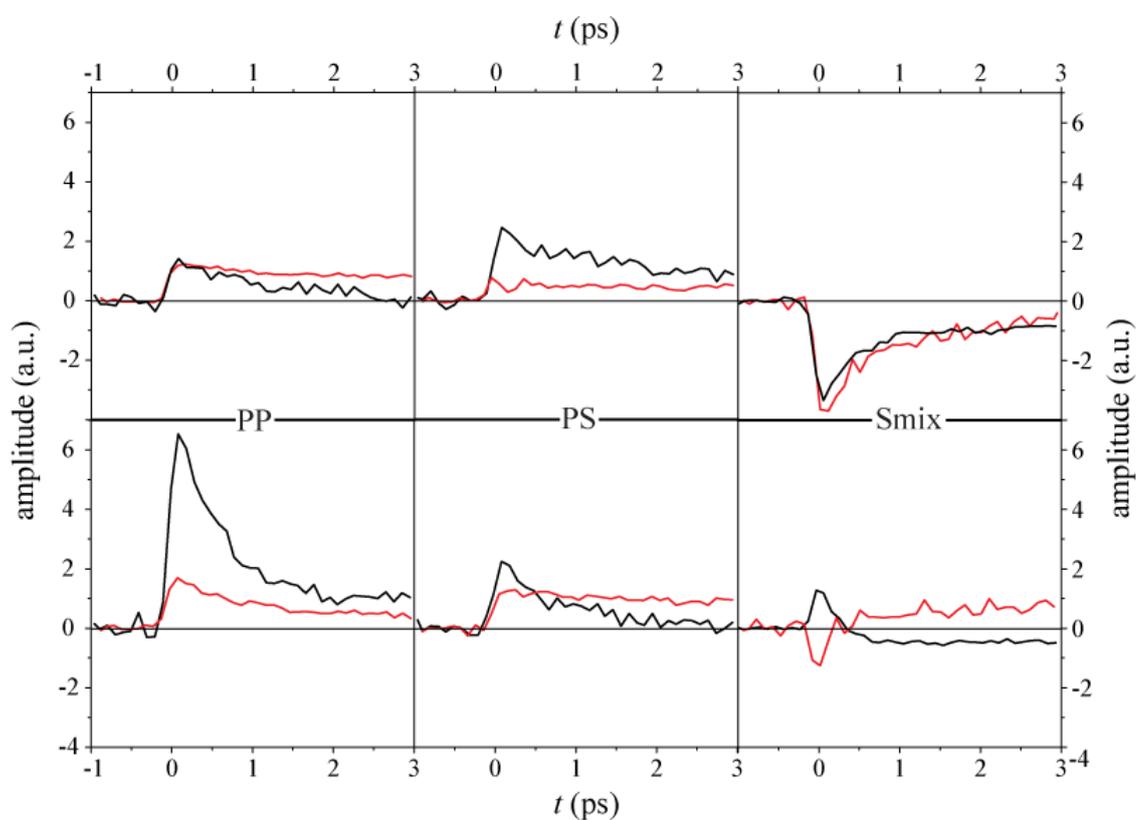
Figure 4.20. Obtained imaginary (top row) and real (bottom row) parts of the measurements performed at different polarization combinations with 1320 nm (black line) and 800 nm (red line) probe. Imaginary and real data were obtained from the normalized amplitude match as shown in Figure 4.19.

Pump orientation and polarization

Returning to the fact that, if the plane of incidence of the pump beam is different or the same as that of the probe beam, the forbidden polarization combinations for the interface between two isotropic media (i.e. SP and SS) can or cannot be probed. This result suggests that the hydrated electron cannot be described by the same symmetry as that of the interface. It is possible then, that the created electron follows the symmetry of the pump that created it, as illustrated in Figure 4.21.
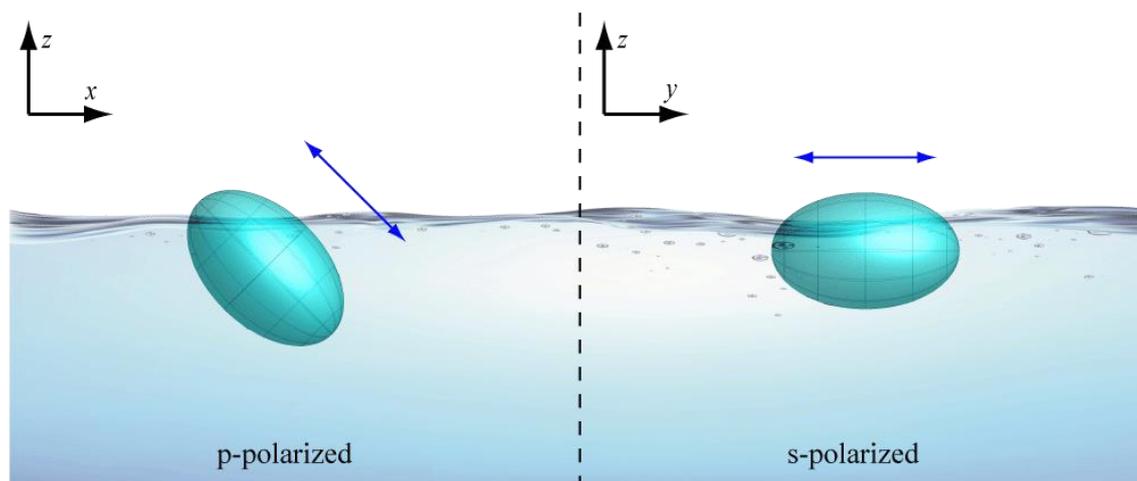
Figure 4.21. Illustration of the proposed possible orientation of the produced hydrated electron with p-polarized (on the left) and s-polarized (on the right) pump. Blue arrows present the pump beam polarization orientation.

If this is the case, then the interfacial electron created with the p-polarized pump would take C_s (m) symmetry, while that created with the s-polarized pump would take C_{2v} (mm2) symmetry. An electron located in the bulk, created with either p- or s-polarized pump, would take $D_{\infty h}$ (mmm) symmetry. Change of the plane of incidence (zx plane) of the probe beam relative to the plane of incidence of the pump beam means that the new x' and y' direction of the probe beam can probe both x and y tensor elements of the electron. However, if the planes of incidence of both beams are the same, then $x'=x$ and $y'=y$. Table 4.1 shows the nonzero tensor elements for the relevant symmetries in the cases of aligned and non-aligned planes of incidence of pump and probe beams. Also shown are the corresponding polarization combinations probing them. If the proposed symmetries for the electron are correct, then the electron at the surface generated either by p- or s-polarized pump can be probed only by using PP, PS and Smix polarization combinations, which is the same as in case of water surface itself. However, for non-aligned pump and probe beam plane of incidence, the electron can be probed also using SP and Pmix polarization combinations in case of using the s-polarized pump, and SS, SP and Pmix polarization combinations in case of the p-polarized pump.

Table 4.1. Non-vanishing tensor elements for considered in the discussion symmetries, and corresponding polarization combinations, with which they can be probed in the configurations of aligned and non-aligned pump and probe beams planes of incidence. Underlined are polarization combinations, which are forbidden in case of aligned planes of incidence or at the interference between two isotropic media.

Symmetry	Tensor elements [192]	Aligned planes of incidence	Non-aligned planes of incidence
Isotropic bulk	All elements vanish		
Interface between two isotropic media ($C_{\infty v}$)	$xzx=yzy$	PP, Smix	*x* and *y* are equivalent, thus it is the same as in aligned planes of incidence
	$xxz=yyz$	PP, Smix	
	$zxx=zyy$	PP, PS	
	zzz	PP	
Electron in bulk ($D_{\infty h}$)	All elements vanish		
Electron at the surface, excited with s-polarized pump (C_{2v})	xzx, xxz	PP	PP, Smix, SP, Pmix
	yyz, yzy	Smix	Smix, PP, SP, Pmix
	zxx	PP	PP, PS, Pmix
	zyy	PS	PS, PP, Pmix
	zzz	PP	PP
Electron at the surface, excited with p-polarized pump (C_s)	xxx	PP	PP, SS, SP, Pmix, Smix, PS
	xyy	PS	PP, SS, SP, Pmix, Smix, PS
	xzx, xxz	PP	PP, Smix, Pmix, SP
	xzz	PP	PP, SP
	yxy, yyx	Smix	PP, SS, SP, Pmix, Smix, PS
	yzy, yyz	Smix	Smix, PP, SP, Pmix
	zxx	PP	PP, PS, Pmix
	zzx, zxz	PP	PP, Pmix
	zyy	PS	PS, PP, Pmix
	zzz	PP	PP

The fact that pump-probe signal using SS and SP polarization combinations were detected for non-aligned planes of incidence seems to support the idea that an electron produced with the p-polarized pump beam has C_s symmetry. However, Figure

4.8 shows that the pump-probe signal obtained with the SS polarization combination is visible only during ~1 ps. This could for example indicate that the observed signal originates from the intermediate state (CTTS state or $(I^0{:}e^-)_{non-eq}$) and the electron in the contact pair have C_{2v} symmetry instead, since pump-probe signal for SP polarization combination is seen at times longer than 1 ps. It could also indicate that the ejected electron is initially localized along the polarization axis of the pump beam, similar as shown on the left side of Figure 4.21, and with time it orients itself along the surface plane, similar as on the right side of Figure 4.21. These scenarios could also explain why no difference was observable between used s- and p-polarized pump, measured with pump and probe sharing the same plane of incidence, suggesting that ejection of the electron from iodide proceeds preferably by ejecting the electron into pre-existing in the solvent void, and not in the direction governed by polarization of the pump.

In order to investigate the initial injection more precisely, experiments with both s- and p-polarized pump for all polarization combinations with aligned and non-aligned pump and probe plane of incidence are suggested. Proposed C_{2v} symmetry for electron generated with s-polarized pump, in contrast to C_s symmetry, should not be detected using SS polarization combination of the probe. Therefore, it is possible to distinguish such two symmetries. Additionally, measurements at different angles between pump and probe plane of incidence could be very insightful.

5   Outlook

The thesis presents a method for studying the dynamics of adsorbates on liquid surfaces. It is based on the surface sensitivity of the second harmonic generation process, however, it exhibits a number of advantages over the conventional SHG technique by using the interference with a local oscillator beam. Using a well-studied system, malachite green, it was shown that the developed method, unlike conventional SHG, provides a signal that is proportional to concentration. This feature is significant in studying systems at low concentration, which is often a case in studying dynamics of the interfacial adsorbates. When using conventional SHG, where the signal depends quadratically on the concentration, an already small signal becomes even smaller. Besides the linearity, it was also shown that the interference based measurements can provide phase information, by comparison with system of a known phase. Because the second order susceptibility, $\chi^{(2)}$, is a complex number, the phase enables real and imaginary parts of the detected signal to be retrieved, which correspond to non-resonant and mostly resonant response, respectively. This means that the signal from the adsorbate can be separated from the signal originating from the non-resonant background. Or as it was shown for the hydrated electron, it enables one to track changes in resonances with time.

By using a lock-in technique, the measurements become very quick and comparatively insensitive to drifts in laser power or alignment. This is due to the elimination of the quadratic terms in equation (2.38) on a shot to shot basis, which otherwise introduces a large offset to the measurement.

The biggest disadvantage of the technique, comparing to the interface based SHG or SFG techniques using broadband beam described in chapter 2, is lack of spectral dispersion. In order to apply this here, the bandwidth of the used pulses would need to be large compared to $1/\Delta t$, where Δt is the delay introduced between SHG and LO by a window placed in the chopper wheel. This could be achieved by increasing Δt, by using thicker windows or windows with higher dispersion, such that delayed between each other SHG and LO pulses would not overlap. However, in that case the group velocity dispersion of the pulses, as they pass through the window, would be significant, thus it would significantly alter the LO measurement with and without the chopper. In the present arrangement, where relatively thin windows are used, this effect is small, and can be mostly neglected. Additionally, the setup would also need a CCD camera instead of PMT and a way to disperse the obtained signal on it. However, in case of studying electronic spectroscopy of the hydrated electron, the bandwidth of the probe would need to be very large, which would require use of a very thick windows.

The methods using broadband beams, where interference fringes are recorded as a function of frequency (due to the interference of the narrowband input beam with different frequencies of the broadband input beam) are however experimentally demanding, requiring micrometre accuracy in the path length to ensure long-term phase stability. In contrast, here, where fringes are recorded as a function of distance L between sample and reference surface, only millimetre to centimetre stability (depending on the probe wavelength) in distance L is required, which is trivially achieved. Another advantage of our method is the short time required in order to achieve relatively good signal to noise ratio. This is especially important in time-resolved measurements, which require collecting data at multiple time delays, making measurements very time consuming. In present work, each time delay point was recorded for 10 s to a few minutes compared to ~50 min for a spectroscopic technique using a broadband beam.[163] However, as it was mentioned before, this is achieved by a trade-off for not recording spectral information.

The experimental setup of the interference based SHG as described in chapter 3 introduces certain inconveniences due to the moving optical elements (including curved mirrors CM5-CM6 and reference surface RS, as seen on Figure 3.9). Generating the LO in reflection from a reference surface located on a translation requires paths of the beams going into the translation stage and leaving it to be precisely parallel with a translation axis of the stage, which can be a challenging task to obtain. Imperfection of proper alignment can, for example cause beams to miss the detector or be cut on the way to it while changing the distance L. Moreover, the movement of and changes in the liquid sample height, due to the vibrations or evaporation of the sample, will cause fundamental beam to impinge the reference at slightly different angle. Hence, slightly different tensor elements of $\chi^{(2)}$ of the reference can take part in generating LO. In order to overcome some of these experimental difficulties, a new experimental arrangement is proposed (as shown in Figure 5.1).
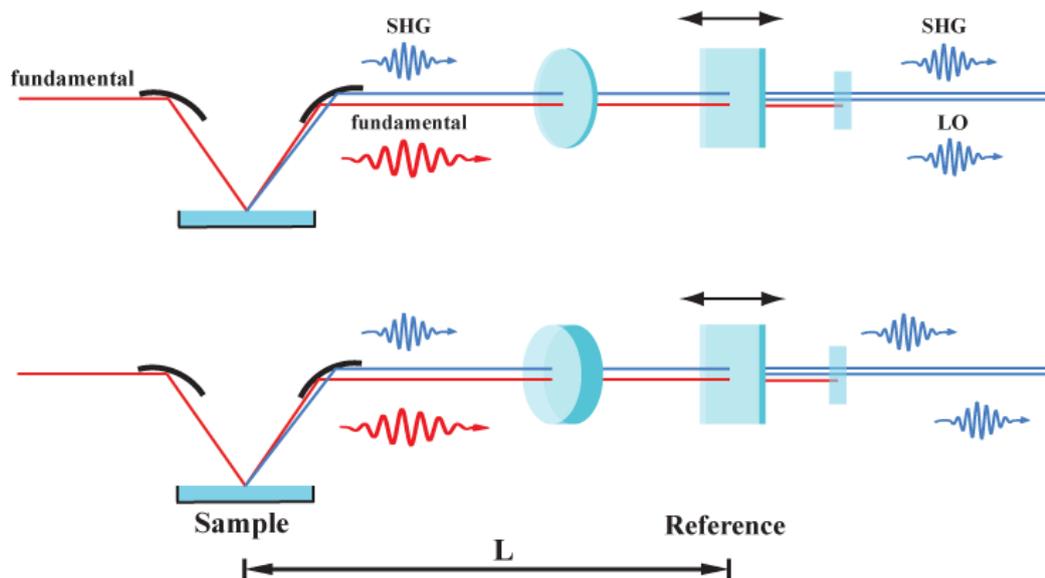
Figure 5.1. Proposed modification to the experimental setup with LO generated in transmission and chopper containing alternating thin and thick windows.

In Figure 5.1, the LO is generated in transmission instead of reflection using a non-linear crystal. The phase change is then obtained by moving the reference along the beam propagation direction, thus no change in beam propagation can be introduced by changing the distance L. In order to maintain overlap of the SHG and LO pulses used in this way, the nonlinear material serving as a reference needs to be accordingly thin.

Additionally, in order to remove the offset introduced by the fact that LO experience loses due to the reflection from the glass window in one of the lock-in measurements as a fundamental and in the other one as a second harmonic, it is proposed that in both of the measurements beams pass through the window such that reflection losses would be the same. The windows for two measurements in this case would have to differ in thickness, such that one would be thick enough to cause SHG and LO pulses to not be temporally overlapped, while the other window so thin that the pulses after it would still be overlapped. Moreover, with this alignment, beams would not need to pass through the chopper twice.
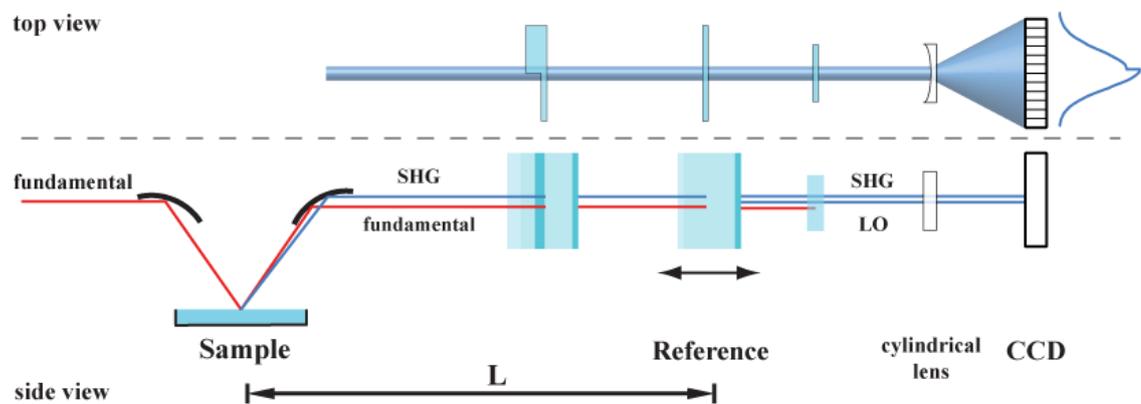
Figure 5.2. Proposed modification to the experimental setup, with LO generated in transmission and without using a chopper.

Another idea (Figure 5.2) is to perform the lock-in measurement without using a chopper at all. Instead, a single glass window could be used, in which one half of the window is thicker than the other one. Two halves of the detected beam would in that case correspond to two different lock-in measurements. Projected on the CCD camera two measurements could be then separated and subtracted from each other. This way would also allow the repetition rate of the experiment to be increased. At present, the repetition rate is restricted by a chopper, which due to the added weight of the custom chopper wheel and inserted windows cannot rotate faster.

Appendix A:

List of optic elements in the pump-probe setup

M12, M20-21, M23, M25-26	PF10-03-P01 - Ø1" (Ø25.4 mm) Protected Silver Mirror, Thorlabs
M13	M254C45 - Ø1" UVFS Cold Mirror, T>92% @ 710-1200nm, R>97% @ 400-690nm, 45° AOI, Thorlabs
M14-16	NB1-J10 - Ø1" Ar-Ion Laser Mirror, 458-528 nm, 45° AOI, Thorlabs
M17	NB1-J10 - Ø1" Ar-Ion Laser Mirror, 458 - 528 nm, 0° AOI, Thorlabs
M18, M22	PF10-03-F01 - Ø1" (Ø25.4 mm) UV Enhanced Aluminum Mirror, Thorlabs
M19, M24, M28	PF10-03-G01 - Ø1" (Ø25.4 mm) Protected Aluminum Mirror, Thorlabs
M27	BB1-E01 - Ø1" Broadband Dielectric Mirror, 350-400 nm, 0-45° AOI, Thorlabs
CM1	092-0125R-1500 - Ø1" Protected Silver Plano-concave Spherical Mirror, r=-1500mm, Eksma Optics
CM2-3	106192- Ø1" Protected Aluminum Plano-concave Spherical Mirror, r=400mm, Layertec
CM4-5	105869 - Ø1" Protected Aluminum Plano-concave Spherical Mirror, r=200mm, Layertec
CM6	106190 - Ø1" Protected Aluminum Plano-concave Spherical Mirror, r=100mm, Layertec
FL1	1110-1600 nm filter supplied as a part of TOPAS Prime, Spectra-Physics
FL2	FGL1000- Ø1" RG1000 Colored Glass Filter, 1000 nm Longpass, Thorlabs
FL3	FF01-675/67-25 - Ø1" BrightLine® single-band bandpass filter, T>90% @ 641.5-708.5nm, Semrock FF01-400/40-25 - Ø1" BrightLine® single-band bandpass filter, T>90% @ 380-420nm, Semrock
ND	NDC-100C-2 - Unmounted Continuously Variable ND Filter, Ø100 mm, OD: 0-2.0, Thorlabs

BBO2	BBO type 1 crystal, ϑ=52.4°, Photox Optical Systems
BBO3	BBO type 1 crystal, ϑ=29.2°, Photox Optical Systems
BBO4	BBO type 1 crystal, ϑ=44.3°, Photox Optical Systems
PR3	2x NB1-J02 - Ø1" Ar-Ion Laser Mirror, 244-257 nm, 45° AOI, Thorlabs
PR4	2x PF10-03-P01 - Ø1" (Ø25.4 mm) Protected Silver Mirror, Thorlabs
WP1	AHWP10M-600 - Ø1" Mounted Achromatic Half-Wave Plate, 400-800nm, Thorlabs
WP2	WPH05M-780 - Ø1/2" Mounted Zero-Order Half-Wave Plate, 780nm, Thorlabs
PL	GT5-A – Glan-Taylor Calcite Polarizer, AR Coated, 350-700nm, Thorlabs
CH	10x CaF_2 Polished Windows, 10x2mm, Crystran Limited or 10x SF10 Polished Windows, 10x2mm, UQG Optics
RS	(110)-cut GaAs undoped crystal, 10x10x0.5mm, MTI

Appendix B
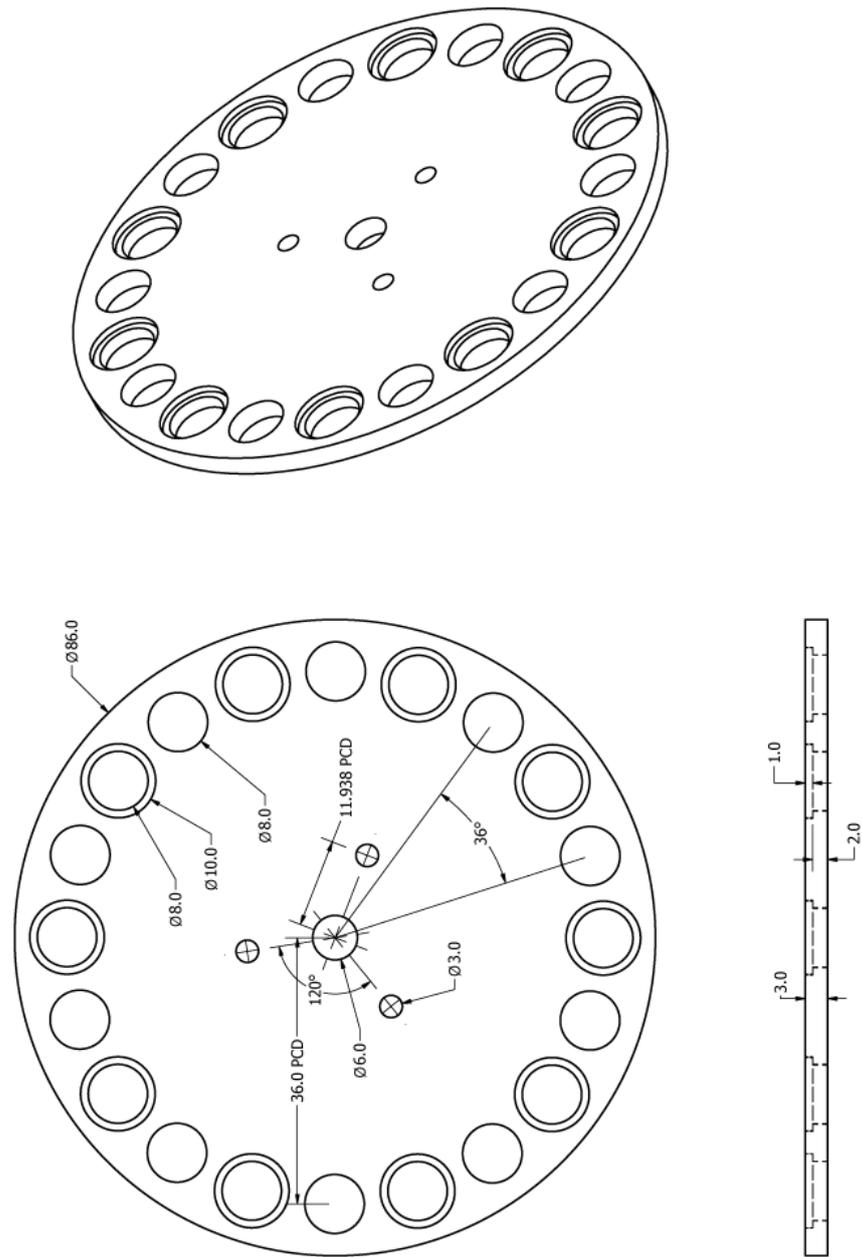
Figure. Technical drawing of custom designed chopper wheel. Values given in (mm).

Bibliography

1.   Kraus, C.A., *Solutions of metals in non-metallic solvents, I General properties of solutions of metals in liquid ammonia.* Journal of the American Chemical Society, **29**(1907): p. 1557.

2.   Kraus, C.A., *Solutions of metals in non-metallic solvents; IV. Material effects accompanying the passage of an electrical current through solutions of metals in liquid ammonia, migration experiments.* Journal of the American Chemical Society, **30**(1908): p. 1323.

3.   Kraus, C.A., *Solutions of metals in non-metallic solvents V The electromotive force of concentration cells of solutions of sodium in liquid ammonia and the relative speed of the ions in these solutions.* Journal of the American Chemical Society, **36**(1914): p. 864.

4.   Kraus, C.A., *Solutions of metals in non-metallic solvents. VI. The conductance of the alkali metals in liquid ammonia.* Journal of the American Chemical Society, **43**(1921): p. 749.

5.   Gibson, G.E. and Argo, W.L., *The Absorption Spectra of the Blue Solutions of Certain Alkali and Alkaline Earth Metals in Liquid Ammonia and in Methylamine.* Journal of the American Chemical Society, **40**(1918): p. 1327.

6.   Radiobiology, N.R.C.S.o., *Basic Mechanisms in Radiobiology II. Physical and Chemical Aspects: Proceedings of an Informal Conference Held at Highland Park, Illinois, May 7-9, 1953*. 1953: National Research Council.

7.   Hart, E.J. and Boag, J.W., *Absorption Spectrum of Hydrated Electron in Water and in Aqueous Solutions.* Journal of the American Chemical Society, **84**(1962): p. 4090.

8.   Boag, J.W. and Hart, E.J., *Absorption Spectra in Irradiated Water and Some Solutions - Absorption Spectra of Hydrated Electron.* Nature, **197**(1963): p. 45.

9.   Keene, J.P., *Absorption Spectra in Irradiated Water and Some Solutions - Optical Absorptions in Irradiated Water.* Nature, **197**(1963): p. 47.

10.   Boudaiffa, B., Cloutier, P., Hunting, D., Huels, M.A., and Sanche, L., *Resonant formation of DNA strand breaks by low-energy (3 to 20 eV) electrons.* Science, **287**(2000): p. 1658.

11.   Huels, M.A., Boudaiffa, B., Cloutier, P., Hunting, D., and Sanche, L., *Single, double, and multiple double strand breaks induced in DNA by 3-100 eV electrons.* Journal of the American Chemical Society, **125**(2003): p. 4467.

12.   Wang, C.R., Nguyen, J., and Lu, Q.B., *Bond Breaks of Nucleotides by Dissociative Electron Transfer of Nonequilibrium Prehydrated Electrons: A New Molecular Mechanism for Reductive DNA Damage.* Journal of the American Chemical Society, **131**(2009): p. 11320.

13.   Michael, B.D. and O'Neill, P., *Molecular biology - A sting in the tail of electron tracks.* Science, **287**(2000): p. 1603.

14.   Wang, C.R., Hu, A., and Lu, Q.B., *Direct observation of the transition state of ultrafast electron transfer reaction of a radiosensitizing drug bromodeoxyuridine.* Journal of Chemical Physics, **124**(2006): p. 241102.

15.   Wang, C.R. and Lu, Q.B., *Real-time observation of a molecular reaction mechanism of aqueous 5-Halo-2 '-deoxyuridines under UV/ionizing radiation.* Angewandte Chemie-International Edition, **46**(2007): p. 6316.

16.   Lu, Q.B., *Molecular reaction mechanisms of combination treatments of low-dose cisplatin with radiotherapy and photodynamic therapy.* Journal of Medicinal Chemistry, **50**(2007): p. 2601.

17.   Lu, Q.B., Kalantari, S., and Wang, C.R., *Electron transfer reaction mechanism of cisplatin with DNA at the molecular level.* Molecular Pharmaceutics, **4**(2007): p. 624.

18.   Behmand, B., Cloutier, P., Girouard, S., Wagner, J.R., Sanche, L., and Hunting, D.J., *Hydrated Electrons React with High Specificity with Cisplatin Bound to Single-Stranded DNA.* Journal of Physical Chemistry B, **117**(2013): p. 15994.

19.   Lu, Q.B. and Sanche, L., *Effects of cosmic rays on atmospheric chlorofluorocarbon dissociation and ozone depletion.* Physical Review Letters, **87**(2001): p. 078501.

20.   Lu, Q.B. and Sanche, L., *Enhanced dissociative electron attachment to CF2Cl2 by transfer of electrons in precursors to the solvated state in water and ammonia ice.* Physical Review B, **63**(2001): p. 153403.

21.   Lu, Q.B. and Madey, T.E., *Giant enhancement of electron-induced dissociation of chlorofluorocarbons coadsorbed with water or ammonia ices: Implications for atmospheric ozone depletion.* Journal of Chemical Physics, **111**(1999): p. 2861.

22.   Buxton, G.V., Greenstock, C.L., Helman, W.P., and Ross, A.B., *Critical-Review of Rate Constants for Reactions of Hydrated Electrons, Hydrogen-Atoms and Hydroxyl Radicals (.Oh/.O-) in Aqueous-Solution.* Journal of Physical and Chemical Reference Data, **17**(1988): p. 513.

23.   Laenen, R., Roth, T., and Laubereau, A., *Novel precursors of solvated electrons in water: Evidence for a charge transfer process.* Physical Review Letters, **85**(2000): p. 50.

24.   Adloff, J.P. and Guillaumont, R., *Fundamentals of radiochemistry.* 1993: CRC Press.

25.   Han, P. and Bartels, D.M., *H/D Isotope Effects in Water Radiolysis .2. Dissociation of Electronically Excited Water.* Journal of Physical Chemistry, **94**(1990): p. 5824.

26.   Nikogosyan, D.N., Oraevsky, A.A., and Rupasov, V.I., *2-Photon Ionization and Dissociation of Liquid Water by Powerful Laser Uv-Radiation.* Chemical Physics, **77**(1983): p. 131.

27.   Boyle, J.W., Ghormley, J.A., Hochanad.Cj, and Riley, J.R., *Production of Hydrated Electrons by Flash Photolysis of Liquid Water with Light in First Continuum.* Journal of Physical Chemistry, **73**(1969): p. 2886.

28.   Sokolov, U. and Stein, G., *Photolysis of Liquid Water at 1849 A.* Journal of Chemical Physics, **44**(1966): p. 3329.

29.   Crowell, R.A. and Bartels, D.M., *Multiphoton ionization of liquid water with 3.0-5.0 eV photons.* Journal of Physical Chemistry, **100**(1996): p. 17940.

30.   Thomsen, C.L., Madsen, D., Keiding, S.R., Thogersen, J., and Christiansen, O., *Two-photon dissociation and ionization of liquid water studied by femtosecond transient absorption spectroscopy.* Journal of Chemical Physics, **110**(1999): p. 3453.

31.   Elles, C.G., Jailaubekov, A.E., Crowell, R.A., and Bradforth, S.E., *Excitation-energy dependence of the mechanism for two-photon ionization of liquid H2O and D2O from 8.3 to 12.4 eV.* Journal of Chemical Physics, **125**(2006): p. 044515.

32.   Kambhampati, P., Son, D.H., Kee, T.W., and Barbara, P.F., *Solvation dynamics of the hydrated electron depends on its initial degree of electron delocalization.* Journal of Physical Chemistry A, **106**(2002): p. 2374.

33.   Lian, R., Oulianov, D.A., Shkrob, I.A., and Crowell, R.A., *Geminate recombination of electrons generated by above-the-gap (12.4 eV) photoionization of liquid water.* Chemical Physics Letters, **398**(2004): p. 102.

34.   Pimblott, S.M., *Independent Pairs Modeling of the Kinetics Following the Photoionization of Liquid Water.* Journal of Physical Chemistry, **95**(1991): p. 6946.

35.   Savolainen, J., Uhlig, F., Ahmed, S., Hamm, P., and Jungwirth, P., *Direct observation of the collapse of the delocalized excess electron in water.* Nature Chemistry, **6**(2014): p. 697.

36.   Jortner, J., Ottolenghi, M., and Stein, G., *On Photochemistry of Aqueous Solutions of Chloride Bromide + Iodide Ions.* Journal of Physical Chemistry, **68**(1964): p. 247.

37.   Chen, X.Y. and Bradforth, S.E., *The ultrafast dynamics of photodetachment.* Annual Review of Physical Chemistry, **59**(2008): p. 203.

38.   Fox, M. and Mcintyre, R., *Far Ultraviolet Solution Spectroscopy of Hydroxide.* Faraday Discussions, **64**(1977): p. 167.

39.   Moore, C.E., *Atomic Energy Levels: As Derived from the Analyses of Optical Spectra.* 1952: U.S. Department of Commerce, National Bureau of Standards.

40.   Takahashi, N., Sakai, K., Tanida, H., and Watanabe, I., *Vertical Ionization-Potentials and Ctts Energies for Anions in Water and Acetonitrile.* Chemical Physics Letters, **246**(1995): p. 183.

41.   Sheu, W.S. and Rossky, P.J., *Dynamics of Electron Photodetachment from an Aqueous Halide Ion.* Chemical Physics Letters, **213**(1993): p. 233.

42.   Sheu, W.S. and Rossky, P.J., *Electronic and solvent relaxation dynamics of a photoexcited aqueous halide.* Journal of Physical Chemistry, **100**(1996): p. 1295.

43.   Bradforth, S.E. and Jungwirth, P., *Excited states of iodide anions in water: A comparison of the electronic structure in clusters and in bulk solution.* Journal of Physical Chemistry A, **106**(2002): p. 1286.

44.   Ohtaki, H. and Radnai, T., *Structure and Dynamics of Hydrated Ions.* Chemical Reviews, **93**(1993): p. 1157.

45.   Bragg, A.E. and Schwartz, B.J., *The ultrafast charge-transfer-to-solvent dynamics of iodide in tetrahydrofuran. 1. Exploring the roles of solvent and solute electronic structure in condensed-phase charge-transfer reactions.* Journal of Physical Chemistry B, **112**(2008): p. 483.

46.   Messina, F., Bram, O., Cannizzo, A., and Chergui, M., *Real-time observation of the charge transfer to solvent dynamics.* Nature Communications, **4**(2013): p. 2119.

47.   Bedard-Hearn, M.J., Larsen, R.E., and Schwartz, B.J., *The role of solvent structure in the absorption spectrum of solvated electrons: Mixed quantum/classical simulations in tetrahydrofuran.* Journal of Chemical Physics, **122**(2005): p. 134506.

48.   Bowron, D.T., Finney, J.L., and Soper, A.K., *The structure of liquid tetrahydrofuran.* Journal of the American Chemical Society, **128**(2006): p. 5119.

49.   Kloepfer, J.A., Vilchiz, V.H., Lenchenkov, V.A., and Bradforth, S.E., *Electron photodetachment in solution*, in *Liquid Dynamics: Experiment, Simulation, and Theory*. 2002. p. 108-121.

50. Borgis, D. and Staib, A., *Quantum adiabatic umbrella sampling: The excited state free energy surface of an electron-atom pair in solution.* Journal of Chemical Physics, **104**(1996): p. 4776.

51. Staib, A. and Borgis, D., *Reaction pathways in the photodetachment of an electron from aqueous chloride: A quantum molecular dynamics study.* Journal of Chemical Physics, **104**(1996): p. 9027.

52. Vilchiz, V.H., Chen, X.Y., Kloepfer, J.A., and Bradforth, S.E., *Solvent effects on geminate recombination dynamics after photodetachment.* Radiation Physics and Chemistry, **72**(2005): p. 159.

53. Chen, X., *Ultrafast transient spectroscopy and electron photodetachment of inorganic and organic anions in aqueous solutions.* 2006, University of Southern California: Los Angeles.

54. Kloepfer, J.A., Vilchiz, V.H., Lenchenkov, V.A., and Bradforth, S.E., *Molecular mechanisms for photodetachment in water.*, in *Ultrafast Phenomena XIII*, D. Miller, Editor. 2003, Springer Verlag: Vancouver Canada. p. 471–73.

55. Moskun, A.C., Bradforth, S.E., Thogersen, J., and Keiding, S., *Absence of a signature of aqueous I(P-2(1/2)) after 200-nm photodetachment of I-(aq).* Journal of Physical Chemistry A, **110**(2006): p. 10947.

56. Jungwirth, P. and Tobias, D.J., *Molecular structure of salt solutions: A new view of the interface with implications for heterogeneous atmospheric chemistry.* Journal of Physical Chemistry B, **105**(2001): p. 10468.

57. Jungwirth, P. and Tobias, D.J., *Ions at the air/water interface.* Journal of Physical Chemistry B, **106**(2002): p. 6361.

58. Dang, L.X. and Chang, T.M., *Molecular mechanism of ion binding to the liquid/vapor interface of water.* Journal of Physical Chemistry B, **106**(2002): p. 235.

59. Petersen, P.B., Johnson, J.C., Knutsen, K.P., and Saykally, R.J., *Direct experimental validation of the Jones-Ray effect.* Chemical Physics Letters, **397**(2004): p. 46.

60. Herbert, J.M. and Jacobson, L.D., *Structure of the Aqueous Electron: Assessment of One-Electron Pseudopotential Models in Comparison to Experimental Data and Time-Dependent Density Functional Theory.* Journal of Physical Chemistry A, **115**(2011): p. 14470.

61.   Turi, L. and Rossky, P.J., *Theoretical Studies of Spectroscopy and Dynamics of Hydrated Electrons.* Chemical Reviews, **112**(2012): p. 5641.

62.   Kevan, L., *Geometrical Structure of Solvated Electrons.* Radiation Physics and Chemistry, **17**(1981): p. 413.

63.   Coe, J.V., Williams, S.M., and Bowen, K.H., *Photoelectron spectra of hydrated electron clusters vs. cluster size: connecting to bulk.* International Reviews in Physical Chemistry, **27**(2008): p. 27.

64.   Tang, Y., Shen, H., Sekiguchi, K., Kurahashi, N., Mizuno, T., Suzuki, Y.I., and Suzuki, T., *Direct measurement of vertical binding energy of a hydrated electron.* Physical Chemistry Chemical Physics, **12**(2010): p. 3653.

65.   Shreve, A.T., Yen, T.A., and Neumark, D.M., *Photoelectron spectroscopy of hydrated electrons.* Chemical Physics Letters, **493**(2010): p. 216.

66.   Siefermann, K.R., Liu, Y.X., Lugovoy, E., Link, O., Faubel, M., Buck, U., Winter, B., and Abel, B., *Binding energies, lifetimes and implications of bulk and interface solvated electrons in water.* Nature Chemistry, **2**(2010): p. 274.

67.   Larsen, R.E., Glover, W.J., and Schwartz, B.J., *Does the Hydrated Electron Occupy a Cavity?* Science, **329**(2010): p. 65.

68.   Jacobson, L.D. and Herbert, J.M., *Comment on "Does the Hydrated Electron Occupy a Cavity?".* Science, **331**(2011): p. 1387.

69.   Turi, L. and Madarasz, A., *Comment on "Does the Hydrated Electron Occupy a Cavity?".* Science, **331**(2011): p. 1387.

70.   Uhlig, F., Marsalek, O., and Jungwirth, P., *Unraveling the Complex Nature of the Hydrated Electron.* Journal of Physical Chemistry Letters, **3**(2012): p. 3071.

71.   Kumar, A., Walker, J.A., Bartels, D.M., and Sevilla, M.D., *A Simple ab Initio Model for the Hydrated Electron That Matches Experiment.* Journal of Physical Chemistry A, **119**(2015): p. 9148.

72.   Jou, F.Y. and Freeman, G.R., *Temperature and Isotope Effects on the Shape of the Optical-Absorption Spectrum of Solvated Electrons in Water.* Journal of Physical Chemistry, **83**(1979): p. 2383.

73.   Jou, F.Y. and Freeman, G.R., *Optical-Spectra of Electrons Solvated in Liquid Ethers - Temperature Effects.* Canadian Journal of Chemistry-Revue Canadienne De Chimie, **54**(1976): p. 3693.

74. Schnitker, J., Motakabbir, K., Rossky, P.J., and Friesner, R., *A-Priori Calculation of the Optical-Absorption Spectrum of the Hydrated Electron.* Physical Review Letters, **60**(1988): p. 456.

75. Jacobson, L.D. and Herbert, J.M., *Polarization-Bound Quasi-Continuum States Are Responsible for the "Blue Tail" in the Optical Absorption Spectrum of the Aqueous Electron.* Journal of the American Chemical Society, **132**(2010): p. 10000.

76. Uhlig, F., Herbert, J.M., Coons, M.P., and Jungwirth, P., *Optical Spectroscopy of the Bulk and Interfacial Hydrated Electron from Ab Initio Calculations.* Journal of Physical Chemistry A, **118**(2014): p. 7507.

77. Coe, J.V., Lee, G.H., Eaton, J.G., Arnold, S.T., Sarkas, H.W., Bowen, K.H., Ludewigt, C., Haberland, H., and Worsnop, D.R., *Photoelectron-Spectroscopy of Hydrated Electron Cluster Anions, (H2o)N-=2-69.* Journal of Chemical Physics, **92**(1990): p. 3980.

78. Verlet, J.R.R., Bragg, A.E., Kammrath, A., Cheshnovsky, O., and Neumark, D.M., *Observation of large water-cluster anions with surface-bound excess electrons.* Science, **307**(2005): p. 93.

79. Barnett, R.N., Landman, U., Cleveland, C.L., and Jortner, J., *Electron Localization in Water Clusters .2. Surface and Internal States.* Journal of Chemical Physics, **88**(1988): p. 4429.

80. Turi, L., Sheu, W.S., and Rossky, P.J., *Characterization of excess electrons in water-cluster anions by quantum simulations.* Science, **309**(2005): p. 914.

81. Ma, L., Majer, K., Chirot, F., and von Issendorff, B., *Low temperature photoelectron spectra of water cluster anions.* Journal of Chemical Physics, **131**(2009): p. 144303.

82. Armbruster, M., Haberland, H., and Schindler, H.G., *Negatively Charged Water Clusters, or the 1st Observation of Free Hydrated Electrons.* Physical Review Letters, **47**(1981): p. 323.

83. Verlet, J.R.R., Kammrath, A., Griffin, G.B., and Neumark, D.M., *Electron solvation in water clusters following charge transfer from iodide.* Journal of Chemical Physics, **123**(2005): p. 231102.

84. Barnett, R.N., Landman, U., and Nitzan, A., *Dynamics of Excess Electron Migration, Solvation, and Spectra in Polar Molecular Clusters.* Journal of Chemical Physics, **91**(1989): p. 5567.

85. Barnett, R.N., Landman, U., and Nitzan, A., *Dynamics of Electron Localization, Solvation, and Migration in Polar Molecular Clusters.* Physical Review Letters, **62**(1989): p. 106.

86. Hammer, N.I., Shin, J.W., Headrick, J.M., Diken, E.G., Roscioli, J.R., Weddle, G.H., and Johnson, M.A., *How do small water clusters bind an excess electron?* Science, **306**(2004): p. 675.

87. Madarasz, A., Rossky, P.J., and Turi, L., *Interior- and surface-bound excess electron states in large water cluster anions.* Journal of Chemical Physics, **130**(2009): p. 124319.

88. Marsalek, O., Uhlig, F., Frigato, T., Schmidt, B., and Jungwirth, P., *Dynamics of Electron Localization in Warm versus Cold Water Clusters.* Physical Review Letters, **105**(2010): p. 043002.

89. Stähler, J., Bovensiepen, U., Meyer, M., and Wolf, M., *A surface science approach to ultrafast electron transfer and solvation dynamics at interfaces.* Chemical Society Reviews, **37**(2008): p. 2180.

90. Gahl, C., Bovensiepen, U., Frischkorn, C., and Wolf, M., *Ultrafast dynamics of electron localization and solvation in ice layers on Cu(111).* Physical Review Letters, **89**(2002): p. 107402.

91. Meyer, M., Stahler, J., Kusmierek, D.O., Wolf, M., and Bovensiepen, U., *Determination of the electron's solvation site on D2O/Cu(111) using Xe overlayers and femtosecond photoelectron spectroscopy.* Physical Chemistry Chemical Physics, **10**(2008): p. 4932.

92. Bertin, M., Mever, M., Stahler, J., Gahl, C., Wolf, M., and Bovensiepen, U., *Reactivity of water-electron complexes on crystalline ice surfaces.* Faraday Discussions, **141**(2009): p. 293.

93. Bovensiepen, U., Gahl, C., Stahler, J., Bockstedte, M., Meyer, M., Baletto, F., Scandolo, S., Zhu, X.Y., Rubio, A., and Wolf, M., *A Dynamic Landscape from Femtoseconds to Minutes for Excess Electrons at Ice-Metal Interfaces.* Journal of Physical Chemistry C, **113**(2009): p. 979.

94.   Bhattacharya, S.K., Inam, F., and Scandolo, S., *Excess electrons in ice: a density functional theory study.* Physical Chemistry Chemical Physics, **16**(2014): p. 3103.

95.   Hermann, A., Schwerdtfeger, P., and Schmidt, W.G., *Theoretical study of the localization of excess electrons at the surface of ice.* Journal of Physics-Condensed Matter, **20**(2008): p. 225003.

96.   Madarasz, A., Rossky, P.J., and Turi, L., *Excess electron relaxation dynamics at water/air interfaces.* Journal of Chemical Physics, **126**(2007): p. 234707.

97.   Buchner, F., Schultz, T., and Lubcke, A., *Solvated electrons at the water-air interface: surface versus bulk signal in low kinetic energy photoelectron spectroscopy.* Physical Chemistry Chemical Physics, **14**(2012): p. 5837.

98.   Yamamoto, Y., Suzuki, Y.I., Tomasello, G., Horio, T., Karashima, S., Mitric, R., and Suzuki, T., *Time- and Angle-Resolved Photoemission Spectroscopy of Hydrated Electrons Near a Liquid Water Surface.* Physical Review Letters, **112**(2014): p. 187603.

99.   Marsalek, O., Uhlig, F., Vandevondele, J., and Jungwirth, P., *Structure, Dynamics, and Reactivity of Hydrated Electrons by Ab Initio Molecular Dynamics.* Accounts of Chemical Research, **45**(2012): p. 23.

100.   Jacobson, L.D. and Herbert, J.M., *Theoretical Characterization of Four Distinct Isomer Types in Hydrated-Electron Clusters, and Proposed Assignments for Photoelectron Spectra of Water Cluster Anions.* Journal of the American Chemical Society, **133**(2011): p. 19889.

101.   Uhlig, F., Marsalek, O., and Jungwirth, P., *Electron at the Surface of Water: Dehydrated or Not?* Journal of Physical Chemistry Letters, **4**(2013): p. 338.

102.   Sagar, D.M., Bain, C.D., and Verlet, J.R.R., *Hydrated Electrons at the Water/Air Interface.* Journal of the American Chemical Society, **132**(2010): p. 6917.

103.   Franken, P.A., Weinreich, G., Peters, C.W., and Hill, A.E., *Generation of Optical Harmonics.* Physical Review Letters, **7**(1961): p. 118.

104.   Haroche, S., *Essay: Fifty Years of Atomic, Molecular and Optical Physics in Physical Review Letters.* Physical Review Letters, **101**(2008): p. 160001.

105.   Bass, M., Hill, A.E., Franken, P.A., Peters, C.W., and Weinreich, G., *Optical Mixing.* Physical Review Letters, **8**(1962): p. 18.

106. Boyd, R.W., *Nonlinear Optics*. 3rd ed. 2008: Academic Press.

107. Shen, Y.R., *The principles of nonlinear optics*. 2003: Wiley-Interscience.

108. Brevet, P.F., *Surface Second Harmonic Generation*. Cahiers de Chimie. 1997, Lausanne: Presses polytechniques et universitaires romandes.

109. Fox, A.M., *Optical Properties of Solids*. 2001: Oxford University Press.

110. Shen, Y.R., *Surface-Properties Probed by 2nd-Harmonic and Sum-Frequency Generation.* Nature, **337**(1989): p. 519.

111. Eisenthal, K.B., *Liquid interfaces probed by second-harmonic and sum-frequency spectroscopy.* Chemical Reviews, **96**(1996): p. 1343.

112. Richmond, G.L., *Molecular bonding and interactions at aqueous surfaces as probed by vibrational sum frequency spectroscopy.* Chemical Reviews, **102**(2002): p. 2693.

113. Shen, Y.R., *Surface nonlinear optics: A historical perspective.* Ieee Journal of Selected Topics in Quantum Electronics, **6**(2000): p. 1375.

114. Geiger, F.M., *Second Harmonic Generation, Sum Frequency Generation, and chi((3)): Dissecting Environmental Interfaces with a Nonlinear Optical Swiss Army Knife.* Annual Review of Physical Chemistry, **60**(2009): p. 61.

115. Bloembergen, N., *Wave Propagation in Nonlinear Electromagnetic Media.* Proceedings of the Ieee, **51**(1963): p. 124.

116. Brown, F., Parks, R.E., and Sleeper, A.M., *Nonlinear Optical Reflection from a Metallic Boundary.* Physical Review Letters, **14**(1965): p. 1029.

117. Brown, F. and Matsuoka, M., *Effect of Adsorbed Surface Layers on Second-Harmonic Light from Silver.* Physical Review, **185**(1969): p. 985.

118. Chen, J.M., Bower, J.R., Wang, C.S., and Lee, C.H., *Optical second-harmonic generation from submonolayer Na-covered Ge surfaces.* Optics Communications, **9**(1973): p. 132.

119. Rudnick, J. and Stern, E.A., *Second-Harmonic Radiation from Metal Surfaces.* Physical Review B, **4**(1971): p. 4274.

120. Fleischmann, M., Hendra, P.J., and Mcquilla.Aj, *Raman-Spectra of Pyridine Adsorbed at a Silver Electrode.* Chemical Physics Letters, **26**(1974): p. 163.

121. Heinz, T.F., Chen, C.K., Ricard, D., and Shen, Y.R., *Spectroscopy of Molecular Monolayers by Resonant 2nd-Harmonic Generation.* Physical Review Letters, **48**(1982): p. 478.

122. Heinz, T.F., Tom, H.W.K., and Shen, Y.R., *Determination of Molecular-Orientation of Monolayer Adsorbates by Optical 2nd-Harmonic Generation.* Physical Review A, **28**(1983): p. 1883.

123. Tom, H.W.K., Mate, C.M., Zhu, X.D., Crowell, J.E., Heinz, T.F., Somorjai, G.A., and Shen, Y.R., *Surface Studies by Optical 2nd-Harmonic Generation - the Adsorption of O2, Co, and Sodium on the Rh(111) Surface.* Physical Review Letters, **52**(1984): p. 348.

124. Rasing, T., Shen, Y.R., Kim, M.W., and Grubb, S., *Observation of Molecular-Reorientation at a 2-Dimensional-Liquid Phase-Transition.* Physical Review Letters, **55**(1985): p. 2903.

125. Richmond, G.L., Rojhantalab, H.M., Robinson, J.M., and Shannon, V.L., *Experiments on Optical 2nd-Harmonic Generation as a Surface Probe of Electrodes.* Journal of the Optical Society of America B-Optical Physics, **4**(1987): p. 228.

126. Giacovazzo, C., *Fundamentals of Crystallography.* 2002: Oxford University Press.

127. Bloembergen, N. and Pershan, P.S., *Light Waves at Boundary of Nonlinear Media.* Physical Review, **128**(1962): p. 606.

128. Guyot-Sionnest, P., Chen, W., and Shen, Y.R., *General Considerations on Optical 2nd-Harmonic Generation from Surfaces and Interfaces.* Physical Review B, **33**(1986): p. 8254.

129. Heinz, T.F., *Nonlinear Optics of Surfaces and Adsorbates*, in *Department of Physics*. 1982, University of California: Berkeley, California.

130. Hecht, E., *Optics.* 4th ed. 2002: Addison Wesley.

131. Heinz, T.F., *Second-Order Nonlinear Optical Effects at Surfaces and Interfaces*, in *Nonlinear Surface Electromagnetic Phenomena*, H.E. Ponath and G.I. Stegeman, Editors. 1991, Elsevier Science Publishers.

132. Pershan, P.S., *Nonlinear Optical Properties of Solids - Energy Considerations.* Physical Review, **130**(1963): p. 919.

133. Guyotsionnest, P. and Shen, Y.R., *Bulk Contribution in Surface 2nd-Harmonic Generation.* Physical Review B, **38**(1988): p. 7985.

134. Yamaguchi, S., Shiratori, K., Morita, A., and Tahara, T., *Electric quadrupole contribution to the nonresonant background of sum frequency generation at air/liquid interfaces.* Journal of Chemical Physics, **134**(2011): p. 184705.

135. Shiratori, K., Yamaguchi, S., Tahara, T., and Morita, A., *Computational analysis of the quadrupole contribution in the second-harmonic generation spectroscopy for the water/vapor interface* Journal of Chemical Physics, **138**(2013): p. 064704.

136. Shen, Y.R., *Basic Theory of Surface Sum-Frequency Generation.* Journal of Physical Chemistry C, **116**(2012): p. 15505.

137. Guyotsionnest, P., Chen, W., and Shen, Y.R., *General-Considerations on Optical 2nd-Harmonic Generation from Surfaces and Interfaces.* Physical Review B, **33**(1986): p. 8254.

138. Heinz, T.F. and Divincenzo, D.P., *Forbidden Nature of Multipolar Contributions to Second-Harmonic Generation in Isotropic Fluids - Comment.* Physical Review A, **42**(1990): p. 6249.

139. Higgins, D.A. and Corn, R.M., *2nd Harmonic-Generation Studies of Adsorption at a Liquid Liquid Electrochemical Interface.* Journal of Physical Chemistry, **97**(1993): p. 489.

140. Wei, X., Hong, S.C., Lvovsky, A.I., Held, H., and Shen, Y.R., *Evaluation of surface vs bulk contributions in sum-frequency vibrational spectroscopy using reflection and transmission geometries.* Journal of Physical Chemistry B, **104**(2000): p. 3349.

141. Guyotsionnest, P. and Shen, Y.R., *Local and Nonlocal Surface Nonlinearities for Surface Optical 2nd-Harmonic Generation.* Physical Review B, **35**(1987): p. 4420.

142. Pool, R.E., Versluis, J., Backus, E.H.G., and Bonn, M., *Comparative Study of Direct and Phase-Specific Vibrational Sum-Frequency Generation Spectroscopy: Advantages and Limitations.* Journal of Physical Chemistry B, **115**(2011): p. 15362.

143. Chang, R.K., Ducuing, J., and Bloember.N, *Relative Phase Measurement between Fundamental and 2nd-Harmonic Light.* Physical Review Letters, **15**(1965): p. 6.

144. Tom, H.W.K., Heinz, T.F., and Shen, Y.R., *2nd-Harmonic Reflection from Silicon Surfaces and Its Relation to Structural Symmetry.* Physical Review Letters, **51**(1983): p. 1983.

145. Berkovic, G., Shen, Y.R., Marowsky, G., and Steinhoff, R., *Interference between 2nd-Harmonic Generation from a Substrate and from an Adsorbate Layer.* Journal of the Optical Society of America B-Optical Physics, **6**(1989): p. 205.

146. Superfine, R., Huang, J.Y., and Shen, Y.R., *Phase Measurement for Surface Infrared Visible Sum-Frequency Generation.* Optics Letters, **15**(1990): p. 1276.

147. Du, Q., Freysz, E., and Shen, Y.R., *Vibrational-Spectra of Water-Molecules at Quartz Water Interfaces.* Physical Review Letters, **72**(1994): p. 238.

148. Ostroverkhov, V., Waychunas, G.A., and Shen, Y.R., *New information on water interfacial structure revealed by phase-sensitive surface spectroscopy.* Physical Review Letters, **94**(2005): p. 046102.

149. Ji, N., Ostroverkhov, V., Chen, C.Y., and Shen, Y.R., *Phase-sensitive sum-frequency vibrational spectroscopy and its application to studies of interfacial alkyl chains.* Journal of the American Chemical Society, **129**(2007): p. 10056.

150. Ji, N., Ostroverkhov, V., Tian, C.S., and Shen, Y.R., *Characterization of vibrational resonances of water-vapor interfaces by phase-sensitive sum-frequency spectroscopy.* Physical Review Letters, **100**(2008): p. 096102.

151. Veenstra, K.J., Petukhov, A.V., de Boer, A.P., and Rasing, T., *Phase-sensitive detection technique for surface nonlinear optics.* Physical Review B, **58**(1998): p. 16020.

152. Wilson, P.T., Jiang, Y., Aktsipetrov, O.A., Mishina, E.D., and Downer, M.C., *Frequency-domain interferometric second-harmonic spectroscopy.* Optics Letters, **24**(1999): p. 496.

153. Yamaguchi, S. and Tahara, T., *Heterodyne-detected electronic sum frequency generation: "Up" versus "down" alignment of interfacial molecules.* Journal of Chemical Physics, **129**(2008): p. 101102.

154. Stiopkin, I.V., Jayathilake, H.D., Bordenyuk, A.N., and Benderskii, A.V., *Heterodyne-detected vibrational sum frequency generation spectroscopy.* Journal of the American Chemical Society, **130**(2008): p. 2271.

155.   Nihonyanagi, S., Yamaguchi, S., and Tahara, T., *Direct evidence for orientational flip-flop of water molecules at charged interfaces: A heterodyne-detected vibrational sum frequency generation study.* Journal of Chemical Physics, **130**(2009): p. 204704.

156.   Watanabe, H., Yamaguchi, S., Sen, S., Morita, A., and Tahara, T., *"Half-hydration" at the air/water interface revealed by heterodyne-detected electronic sum frequency generation spectroscopy, polarization second harmonic generation, and molecular dynamics simulation.* Journal of Chemical Physics, **132**(2010): p. 144701.

157.   Mondal, J.A., Nihonyanagi, S., Yamaguchi, S., and Tahara, T., *Structure and Orientation of Water at Charged Lipid Monolayer/Water Interfaces Probed by Heterodyne-Detected Vibrational Sum Frequency Generation Spectroscopy.* Journal of the American Chemical Society, **132**(2010): p. 10656.

158.   Hua, W., Chen, X.K., and Allen, H.C., *Phase-Sensitive Sum Frequency Revealing Accommodation of Bicarbonate Ions, and Charge Separation of Sodium and Carbonate Ions within the Air/Water Interface.* Journal of Physical Chemistry A, **115**(2011): p. 6233.

159.   Kundu, A., Yarnaguchi, S., and Tahara, T., *Evaluation of pH at Charged Lipid/Water Interfaces by Heterodyne-Detected Electronic Sum Frequency Generation.* Journal of Physical Chemistry Letters, **5**(2014): p. 762.

160.   Xiong, W., Laaser, J.E., Mehlenbacher, R.D., and Zanni, M.T., *Adding a dimension to the infrared spectra of interfaces using heterodyne detected 2D sum-frequency generation (HD 2D SFG) spectroscopy.* Proceedings of the National Academy of Sciences of the United States of America, **108**(2011): p. 20902.

161.   Nihonyanagi, S., Mondal, J.A., Yamaguchi, S., and Tahara, T., *Structure and Dynamics of Interfacial Water Studied by Heterodyne-Detected Vibrational Sum-Frequency Generation.* Annual Review of Physical Chemistry, Vol 64, **64**(2013): p. 579.

162.   Watanabe, K., Inoue, K., Nakai, I.F., and Matsumoto, Y., *Nonadiabatic coupling between C-O stretching and Pt substrate electrons enhanced by frustrated mode excitations.* Physical Review B, **81**(2010): p. 241408.

163.   Nihonyanagi, S., Singh, P.C., Yamaguchi, S., and Tahara, T., *Ultrafast Vibrational Dynamics of a Charged Aqueous Interface by Femtosecond Time-Resolved Heterodyne-Detected Vibrational Sum Frequency Generation.* Bulletin of the Chemical Society of Japan, **85**(2012): p. 758.

164.   Singh, P.C., Nihonyanagi, S., Yamaguchi, S., and Tahara, T., *Ultrafast vibrational dynamics of water at a charged interface revealed by two-dimensional heterodyne-detected vibrational sum frequency generation.* Journal of Chemical Physics, **137**(2012): p. 094706.

165.   Stolle, R., Marowsky, G., Schwarzberg, E., and Berkovic, G., *Phase measurements in nonlinear optics.* Applied Physics B-Lasers and Optics, **63**(1996): p. 491.

166.   Shen, Y.R., *Phase-Sensitive Sum-Frequency Spectroscopy.* Annual Review of Physical Chemistry, Vol 64, **64**(2013): p. 129.

167.   Maguire, L.P., Szilagyi, S., and Scholten, R.E., *High performance laser shutter using a hard disk drive voice-coil actuator.* Review of Scientific Instruments, **75**(2004): p. 3077.

168.   Hale, G.M. and Querry, M.R., *Optical-Constants of Water in 200-nm to 200-μm Wavelength Region.* Applied Optics, **12**(1973): p. 555.

169.   Singh, S., *Non-linear Optic Materials*, in *Handbook of Lasers with Selected Data on Optical Technology*, R.J. Pressley, Editor. 1971, Chemical Rubber Co.: Cleveland.

170.   Stehlin, T., Feller, M., Guyotsionnest, P., and Shen, Y.R., *Optical 2nd-Harmonic Generation as a Surface Probe for Noncentrosymmetric Media.* Optics Letters, **13**(1988): p. 389.

171.   Wynne, J.J. and Bloember.N, *Measurement of Lowest-Order Nonlinear Susceptibility in 3-5 Semiconductors by Second-Harmonic Generation with a Co2 Laser.* Physical Review, **188**(1969): p. 1211.

172.   Miller, R.C. and Nordland, W.A., *Absolute Signs of Second-Harmonic Generation Coefficients of Piezoelectric Crystals.* Physical Review B, **2**(1970): p. 4896.

173.   *Standards on Piezoelectric Crystals, 1949.* Proceedings of the Institute of Radio Engineers, **37**(1949): p. 1378.

174. Shi, X., Borguet, E., Tarnovsky, A.N., and Eisenthal, K.B., *Ultrafast dynamics and structure at aqueous interfaces by second harmonic generation.* Chemical Physics, **205**(1996): p. 167.

175. Sen, P., Yamaguchi, S., and Tahara, T., *Ultrafast dynamics of malachite green at the air/water interface studied by femtosecond time-resolved electronic sum frequency generation (TR-ESFG): an indicator for local viscosity.* Faraday Discussions, **145**(2010): p. 411.

176. Eisenthal, K.B., *Photochemistry and photophysics of liquid interfaces by second harmonic spectroscopy.* Journal of Physical Chemistry, **100**(1996): p. 12997.

177. Fedoseeva, M., Fita, P., Punzi, A., and Vauthey, E., *Salt Effect on the Formation of Dye Aggregates at Liquid/Liquid Interfaces Studied by Time-Resolved Surface Second Harmonic Generation.* Journal of Physical Chemistry C, **114**(2010): p. 13774.

178. Fita, P., Punzi, A., and Vauthey, E., *Local Viscosity of Binary Water plus Glycerol Mixtures at Liquid/Liquid Interfaces Probed by Time-Resolved Surface Second Harmonic Generation.* Journal of Physical Chemistry C, **113**(2009): p. 20705.

179. Punzi, A., Martin-Gassin, G., Grilj, J., and Vauthey, E., *Effect of Salt on the Excited-State Dynamics of Malachite Green in Bulk Aqueous Solutions and at Air/Water Interfaces: a Femtosecond Transient Absorption and Surface Second Harmonic Generation Study.* Journal of Physical Chemistry C, **113**(2009): p. 11822.

180. Duxbury, D.F., *The Photochemistry and Photophysics of Triphenylmethane Dyes in Solid and Liquid-Media.* Chemical Reviews, **93**(1993): p. 381.

181. Nakayama, A. and Taketsugu, T., *Ultrafast Nonradiative Decay of Electronically Excited States of Malachite Green: Ab Initio Calculations.* Journal of Physical Chemistry A, **115**(2011): p. 8808.

182. Yoshizawa, M., Suzuki, K., Kubo, A., and Saikan, S., *Femtosecond study of S-2 fluorescence in malachite green in solutions.* Chemical Physics Letters, **290**(1998): p. 43.

183. Bhasikuttan, A.C., Sapre, A.V., and Okada, T., *Ultrafast relaxation dynamics from the S-2 state of malachite green studied with femtosecond upconversion spectroscopy.* Journal of Physical Chemistry A, **107**(2003): p. 3030.

184. Iglev, H., Trifonov, A., Thaller, A., Buchvarov, I., Fiebig, T., and Laubereau, A., *Photoionization dynamics of an aqueous iodide solution: the temperature dependence.* Chemical Physics Letters, **403**(2005): p. 198.

185. Kloepfer, J.A., Vilchiz, V.H., Lenchenkov, V.A., and Bradforth, S.E., *Femtosecond dynamics of photodetachment of the iodide anion in solution: resonant excitation into the charge-transfer-to-solvent state.* Chemical Physics Letters, **298**(1998): p. 120.

186. Kloepfer, J.A., Vilchiz, V.H., Lenchenkov, V.A., Germaine, A.C., and Bradforth, S.E., *The ejection distribution of solvated electrons generated by the one-photon photodetachment of aqueous I- and two-photon ionization of the solvent.* Journal of Chemical Physics, **113**(2000): p. 6288.

187. Shirom, M. and Stein, G., *Excited State Chemistry of Ferrocyanide Ion in Aqueous Solution .1. Formation of Hydrated Electron.* Journal of Chemical Physics, **55**(1971): p. 3372.

188. Lenchenkov, V., Kloepfer, J., Vilchiz, V., and Bradforth, S.E., *Electron photodetachment from [Fe(CN)(6)](4-): photoelectron relaxation and geminate recombination.* Chemical Physics Letters, **342**(2001): p. 277.

189. Assel, M., Laenen, R., and Laubereau, A., *Ultrafast electron trapping in an aqueous NaCl-solution.* Chemical Physics Letters, **289**(1998): p. 267.

190. Gauduel, Y., Migus, A., Chambaret, J.P., and Antonetti, A., *Femtosecond Reactivity of Electron in Aqueous-Solutions.* Revue De Physique Appliquee, **22**(1987): p. 1755.

191. Goh, M.C., Hicks, J.M., Kemnitz, K., Pinto, G.R., Bhattacharyya, K., Heinz, T.F., and Eisenthal, K.B., *Absolute Orientation of Water-Molecules at the Neat Water-Surface.* Journal of Physical Chemistry, **92**(1988): p. 5074.

192. Powell, R.C., *Symmetry, Group Theory, and the Physical Properties of Crystals*. Lecture Notes in Physics. 2010, New York: Springer